ADDITIVE MANUFACTURING TECHNOLOGIES FOR FLEXIBLE OPTICAL AND BIOMEDICAL SYSTEMS

by

Bongjoong Kim

Dissertation

Submitted to the Faculty of Purdue University

In Partial Fulfillment of the Requirements for the degree of

Doctor of Philosophy

School of Mechanical Engineering

West Lafayette, Indiana

May 2021

THE PURDUE UNIVERSITY GRADUATE SCHOOL
STATEMENT OF COMMITTEE APPROVAL

Dr. Chi Hwan Lee, Chair
School of Mechanical Engineering

Dr. Liang Pan
School of Mechanical Engineering

Dr. Craig Goergen
Weldon School of Biomedical Engineering

Dr. Zahyun Ku
Air Force Research Laboratory

Approved by:
Dr. Nicole L. Key

ACKNOWLEDGMENTS

Foremost, I would like to express my deepest gratitude for all support during my college life to my advisor Prof. Chi Hwan Lee for giving me the opportunity to conduct research and providing invaluable guidance during my Ph.D. degree. His vision, sincerity, passion, and motivation have deeply inspired me. He guided research direction, which great privilege and honor to my work and study. I am extremely grateful and I could not imagine have a better advisor and mentor for my Ph.D. study.

Besides my advisor, I would like to thank my committee members, Dr. Zahyun Ku, Prof. Liang Pan, Prof. Adrian Buganza Tepole, and Prof. Craig Goergen, for their encouragement, insightful comments, and important advice.

I thank all my labmates in Lee Research Group during my Ph.D. degree: Dae Seung Wie, Hyungjun Kim, Donghyun Baek, Hanmin Jang, Heungsoo Lee, Woohyun Park, Kyunghun Kim, Heun Park, Eun Kwang Lee, Yale Jeon, Jonghun Yi, Taehoo Chang, Seul Ah Lee, Seokkyoon Hong, Jinyuan Zhang, Sena Huh, and Jehwan Hwang.

Last but not the least, I am extremely grateful to my parents, Hee Chae Kim, Malnyeo Choi, and my mother-in-law,Young Ae Kim, for their love, prayers, caring and sacrifices for educating for my future. Also, I am very much thankful to my wife (Soo Hyun Kim) and my son (Yulha Kim) for their love, understanding, and continuing support to complete my Ph.D. degree. Also, I express my thanks to my sister (Kang Yun Kim), bother in law (Jae Moon Kim) for their support. My special thanks go to my grandparents in heaven for their love, caring, and sacrifices.

I would like to say thanks to my friends and research colleagues, Arvin Soepriatna, Yue Zhang, Kwan Soo Lee, Jiyeon Jeon, Dong Rip Kim for their encouragement and genuine support throughout this research work.

Finally, my thanks go to all the people who have supported me to complete the research work directly or indirectly.

TABLE OF CONTENTS

LIST OF TABLES 7
LIST OF FIGURES 8
ABSTRACT 16
1. INTRODUCTION 18
1.1 Background 18
1.2 Overview of conventional manufacturing technologies 20
1.2.1 Sacrificial layer etching-based transfer printing 20
1.2.2 Controlled spalling-based transfer printing 22
1.2.3 Interfacial layer delamination-based transfer printing 24
2. MECHANICS-DRIVEN MANUFACTURING OF QUASI-THREE-DIMENSIONAL NANOARCHITECTURES 26
2.1 Background 26
2.2 3D nanoassembly method 27
2.3 Mechanism study and mechanics analysis 34
2.4 Applicability to diverse types of quasi-3D plasmonic nanoarrays 44
2.5 Heterogeneous modular assembly with controlled spatial arrangement 48
2.6 Pilot assembly and post-electro-optical (EO) analysis 53
2.7 Methods 60
2.7.1 Fabrication of donor Si substrates 60
2.7.2 Computational analysis 60
2.7.3 Numerical simulation of transmission 61
2.7.4 FTIR measurements 62
2.7.5 Fabrication of MWIR-T2SL-based HPD 62
2.7.6 Characterization of MWIR-T2SL-based HPD 63
2.7.7 Transmission spectra analysis 64
2.8 Conclusion 64
3. MECHANICS-DRIVEN MANUFACTURING OF QUASI-THREE-DIMENSIONAL INFRARED BANDPASS FILTERS 66
3.1 Background 66

3.2 Repetitive replication of quasi-3D plasmonic IR filters 67
3.3 Underlying mechanism of defect-free replication process 73
3.4 Application in IR bandpass filtering 77
3.5 Methods 82
3.5.1 Fabrication of Donor Si Mold 82
3.5.2 Numerical Simulation of Transmission 82
3.5.3 FEM Analysis 83
3.5.4 FTIR measurements 83
3.6 Conclusion 84
4. ELECTROCHEMICAL REACTION-DRIVEN DELAMINATION OF THIN FILM ARCHITECTURES OVER 4 INCH WAFER-SCALE 85
4.1 Background 85
4.2 Microbubble-driven delamination of Quasi-3D plasmonic nanoarchitectures 85
4.3 Microbubble-driven delamination of thin-film electronics 87
4.3.1 Microbubble-driven delamination process 87
4.3.2 Component-level validation of transferred thin-film nanoelectronics 89
4.3.3 Transferred thin-film biosensors 90
5. RAPID CUSTOM PRINTING OF SOFT POROELASTOMERS FOR BIOMEDICAL DEVICES 91
5.1 Background 91
5.2 Custom design and prototyping of poroelastic biosensors 93
5.3 Material structure-property relationships 98
5.4 Rapid custom prototyping 109
5.5 Spatiotemporal recording of epicardial electrocardiogram *in vivo* 113
5.6 Intraoperative epicardial mapping in a murine myocardial infarction model 117
5.7 Intraoperative epicardial mapping in a murine myocardial infarction model 125
5.8 Methods 132
5.8.1 4D heart segmentation 132
5.8.2 Ink composition and preparation 132
5.8.3 Mechanical and electrical measurements under cyclic strains 132
5.8.4 Measurement of rheological properties 133

5.8.5 Molecular dynamics (MD) simulation 133
5.8.6 Fabrication of custom-printed sensor array 134
5.8.7 Animal surgeries on mice 135
5.8.8 Animal surgeries on pigs 136
5.8.9 Simultaneous ultrasound imaging during ECG recording 136
5.8.10 Anti-biofouling analysis 137
5.8.11 Histological analysis 137
5.9 Conclusion 138
6. CONCLUSION 140
REFERENCES 141

LIST OF TABLES

Table 1.1. Printing methods in terms of the working principles, printable materials, and key advantages and challenges. 19

Table 5.1. Comparisons of the poroelastic silicone composite with other existing materials in terms of the mechanical and electrical properties. The following abbreviations are used in this table. Nanowire (NW); Carbon Nanotube (CNT); Poly(Ethylene Oxide) (PEO); Carbon Black (CB); Thermoplastic PolyUrethane (TPU); Styrene-Butadiene-Styrene (SBS); Polydimethylsiloxane (PDMS) 93

Table 5.2. Printing methods in terms of the working principles, printable materials, and key advantages and challenges. 99

LIST OF FIGURES

Figure 1.1. Pick-and-place transfer printing method. i) Schematic illustration of the process flow by using an elastomeric stamp.(Meitl et al., 2006) ii) Schematic diagram of critical energy release rates for the film/substrate interface and the stamp/film interface.(Feng et al., 2007) 22

Figure 1.2. Controlled spalling-driven transfer printing method. i) Schematic illustration of the process flow by exploiting controlled thermal spalling.(Alharbi, Nasri, Wu, & Shahrjerdi, 2016) ii) Schematic illustration of the stress field in the spalling fracture mode.(C. H. Lee et al., 2014) 23

Figure 1.3. Chemomechanics-driven transfer printing method. i) Schematic illustration of the process flow by exploiting controlled interfacial delamination phenomenon. ii) Experimental and finite-element analysis (FEA) results of peeling strength versus peeling distance under wet (water) and dry conditions.(Wie et al., 2018)..... 25

Figure 2.1. Schematic illustration for physical separation of quasi-3D plasmonic nanoarrays from its donor Si substrate..... 28

Figure 2.2. SEM images of various nanopatterns on donor Si substrate configured with circular-shaped nanoholes (a), circular-shaped nanoposts (b), subwavelength nanowire gratings (c), and ring-shaped disks (d). Scale bars are 200 nm, 400 nm, 950 nm, and 3 μm, respectively. 28

Figure 2.3. Photo of a plasmonic film configured with quasi-3D nanoposts on a WST after the separation. Scale bar is 3.5 mm. 29

Figure 2.4. Photo of the plasmonic film afloat on the surface of water after the dissolution of the WST. Scale bar is 3.5 mm. 29

Figure 2.5. Schematic illustration of the microscale positioning and alignment setup. 30

Figure 2.6. Photos of a setting for micro-scale positioning and alignment. Scale bar is 7.5 cm and 5 mm from the left. 30

Figure 2.7. Schematic illustration of the microscale positioning and alignment setup. 31

Figure 2.8. Schematic illustrations for the entire process of the 3D nanoassembly method. 31

Figure 2.9. Photo (left) and enlarged SEM image (right) of the transferred plasmonic film on a receiver Si substrate. Scale bars are 3 mm (left) and 4 μm (right) 32

Figure 2.10. Photo (left) and enlarged SEM image (right) of the donor Si substrate. Scale bars are 3 mm (left) and 6.5 μm (right). 32

Figure 2.11. Photos of a donor Si substrate through 4 times recycle for the transfer of quasi-3D plasmonic nanoarrays to receiver DSP wafers. Scale bar is 4.3 mm. 33

Figure 2.12. SEM images of the transferred quasi-3D nanoposts consisted of BCB (left) and SU-8 (right) as a dielectric spacer. Scale bars are 3.0 μm..... 34

Figure 2.13. Experimental and FEA results of the separation load (L)-separation displacement (D) curves for quasi-3D plasmonic nanoposts under dry (red) and wet (blue) conditions. 35

Figure 2.14. Photo (left) and SEM image (right) of the defects and cracks on a specimen when peeled by the L_{ss} out of the defect-free zone. Scale bars are 3.5 mm and 2.3 μm from the left. .. 35

Figure 2.15. Experimental, FEA, and theoretical results for the effect of H_{post} on L_{ss}/b. 36

Figure 2.16. Experimental and FEA results of the separation load (L)-displacement (D) curves for quasi-3D plasmonic nanoholes under dry (red) and wet (blue) conditions. 37

Figure 2.17. Experimental, FEA, and theoretical results for the effect of H_{hole} on L_{ss}/b. 37

Figure 2.18. FEA results of strain distributions in the nanoarrays during the interfacial separation under dry and wet conditions. 39

Figure 2.19. Schematic of the modeled structure. 39

Figure 2.20. (a) FEA results of the peeling strength (P)-separation distance (d) curves for quasi-3D nanoposts in dry (red) and wet (blue) conditions. (b) FEA results of strain distributions during the interfacial separation for varied d. 40

Figure 2.21. FEA results of the peeling strength (P)-separation distance (d) curves for quasi-3D nanoposts with different Hpost in dry (a) and wet (b) conditions. (c) FEA results of strain distributions during the interfacial separation for varied H_{post}. 41

Figure 2.22. FEA results of the peeling strength (P)-separation distance (d) curves for quasi-3D nanoholes with different H_{hole} in dry (a) and wet (b) conditions. (c) FEA results of strain distributions during the interfacial separation for varied H_{hole}. 42

Figure 2.23. (a) FEA results of the peeling strength (P)-separation distance (d) curves for quasi-3D nanoposts with BCB and SU-8 in dry and wet conditions. (b) FEA results of the peeling strength (P)-separation distance (d) curves for quasi-3D nanoholes with BCB and SU-8 in dry and wet conditions. (c) and (d) FEA results of strain distributions during the interfacial separation for varied dielectric spacer materials. 43

Figure 2.24. Demonstrations on various types of quasi-3D plasmonic nanoarrays. An arrangement of schematic illustrations (left column), SEM images (middle column), and analysis of transmission spectra (right column) for a range of quasi-3D plasmonic nanoarrays configured with (a) nanoposts, (b) nanoholes, (c) bilayer nanowire gratings and (d) ring-shaped disks. Scale bars are 3.3 μm, 2.0 μm, 1.8 μm, and 2.0 μm from the top. 45

Figure 2.25. Detailed geometric information for the quasi-3D nanoarrays configured with nanoposts (a), nanoholes (b), bilayer nanowire gratings (c), and ring-shaped disks (d). 46

Figure 2.26. Repeatedly measured transmission spectra at widely spread locations of the transferred nanoarrays. 47

Figure 2.27. Schematic illustration (left) and photo (right) of multiple stacked plasmonic nanoarrays configured with identical quasi-3D nanoposts. Scale bar is 1 cm. 49

Figure 2.28. The enlarged SEM images of the 1st, 2nd, 3rd, and 4th layer-stacked nanoposts. Scale bar is 2.3 μm. 49

Figure 2.29. Measured transmission spectra of the 2nd, 3rd, and 4th layer-stacked nanoposts... 50

Figure 2.30. Schematic illustration (left) and photo (right) of a 3×3 array of dissimilar quasi-3D plasmonic nanoposts featured with different sizes and arrangements. Scale bar is 1 cm..... 51

Figure 2.31. The enlarged SEM images of each transferred module. Scale bar is 3.3 μm..... 51

Figure 2.32. Measured transmission spectra of the transferred each module unit..... 52

Figure 2.33. Photo (left) and schematic illustration (right) of a demonstration system. Scale bar is 4.5 mm. 54

Figure 2.34. Schematics of the model MWIR-T2SL-based HPD assembled in a flip-chip-on-laminate configuration. 54

Figure 2.35. EO-measured spectral HPD-responses and FTIR-measured transmission of the specimens. 55

Figure 2.36. EO-measured spectral HPD-responses and FTIR-measured transmission of the specimens. 55

Figure 2.37. Schematic diagram of a custom setup for the measurement of optical-to-electrical (EO)-measured spectral response. 57

Figure 2.38. EO-measured spectral HPD-responses and FTIR-measured transmission of the specimens. 57

Figure 2.39. Photos of the as-fabricated HPD (a), the HPD after the assembly of the nanoposts (b), and the HPD after the removal of the nanoposts (c). Scale bars are 3.5 mm, 4.5 mm, and 3.5 mm from the top. 58

Figure 2.40. FIT-simulated distribution of electric field magnitude (|E|) at the peak wavelength for a nanopost unit cell. 59

Figure 2.41. Measured dark- and photo-currents of the specimens. 59

Figure 2.42. Schematic diagram of a custom setup for the measurement of dark- and photo-current. 59

Figure 2.43. (a) Schematic illustration of the nanohole patterns tapered by ~80° from the ground. (b) Cross-sectional SEM image of the tapered nanohole pattern. Scale bar is 160 nm..... 60

Figure 2.44. Measured complex refractive index of PMMA (left) and Au (right) permittivity... 61

Figure 2.45. Schematic illustration of the entire process for the fabrication of the HPD..... 63

Figure 3.1. Schematic illustrations for the fabrication process of a single unit of a quasi-3D metal (i.e., Au)-dielectric (i.e., SU-8) nanoposts. 68

Figure 3.2. Schematic illustrations for the fabrication process of a donor Si mold..... 69

Figure 3.3. (a) Thickness of the dielectric spacer using SU-8 (red line) and Ecoflex (blue line) diluted with the SU-8 2000 ThinnerTM (MicroChem, Inc.) and the Thinning Ecoflex SiliconesTM (Smooth-on, Inc.), respectively. (b) Simulated transmission spectra as a function of wavelength

for the IR filters using SU-8 (400 nm; black line), SU-8 (4 μm; red line), and Ecoflex (4 μm; blue line) as a dielectric spacer. (c) Transmission spectrum of SU-8 (red line) and Ecoflex (blue) at a fixed thickness of 4 μm. 70

Figure 3.4. Schematic illustrations of quasi-3D nanoposts (p = 3 μm; d = 1.2 μm; t_m = 50 nm; t_p = 250 nm; t_d = 400 nm) and nanoholes (p = 3 μm; d = 1.2 μm; t_m = 50 nm, t_p = 330 nm, t_d = 230 nm), respectively. 71

Figure 3.5. Optical photograph and scanning electron microscopy (SEM) images of the transferred nanoantennas. 72

Figure 3.6. SEM images of a donor Si substrate through three times recycle. 73

Figure 3.7. Principal strain distribution (ε) of nanoposts, comprising 3 x 3 square arrays without and with PMMA stress-absorbing layer. 74

Figure 3.8. Principal strain distribution (ε) of nanoholes, comprising 3 x 3 square arrays without and with PMMA stress-absorbing layer. 74

Figure 3.9. Principal strain distribution (ε) of nanoposts, comprising 3 x 3 square arrays without and with PMMA stress-absorbing layer. 75

Figure 3.10. The maximal principal strain and bending stiffness of nanoantennas of function as the thickness of PMMA stress-absorbing layer increase from 0 to 2 μm. 75

Figure 3.11. Representative SEM image of the damaged nanoantenna out of the defect-free zone. 76

Figure 3.12. Schematic illustration for a 3 × 3 square array of nanoantennas under debonding process from an edge, respectively. 77

Figure 3.13. The scanned principal strain profile along *i-i'* and *j-j'* directions across the surface of quasi-3D nanoposts and nanoholes without and with 1 μm thick PMMA stress-absorbing layer. 77

Figure 3.14. Analysis of transmission spectra of nanoantennas. Note that spectra measured across the sample (1 x 1 cm^2) show very good uniformity with only small variations in spectra. 78

Figure 3.15. 2D surface plots of normalized transmission of quasi-3D nanoposts and nanoholes, as a function of array periodicity (p) and wavelength (μm) with SU-8 dielectric spacer. 79

Figure 3.16. Peak wavelengths and FWHMs of quasi-3D nanoposts and nanoholes depending on the geometrical parameters (d, t_p, t_m, t_d). 80

Figure 3.17. (a) Schematic illustrations of a single unit of the quasi-3D nanoposts (top panel) and nanoholes (bottom panel) with the residual deposition of Au at the sidewall. (b) Simulated peak wavelength with the reduce gap space by the sidewall deposition of Au. 81

Figure 3.18. 2D surface plots of normalized transmission of quasi-3D nanoposts and nanoholes, as a function of array periodicity (p) and wavelength (μm) with PMMA dielectric spacer. 82

Figure 4.1. Schematic illustration of basic procedures of the microbubble-driven delamination of quasi-3D plasmonic nanoarchitectures. 86

Figure 4.2. Representative optical and SEM images of the transferred plasmonic nanopost arrays on double-side-polished Si wafer. 86

Figure 4.3. Transmission spectra measurements with and without separation SiO_2 (10 nm thick). 87

Figure 4.4. Schematic illustrations of basic procedures of the microbubble-driven delamination of thin-film nanoelectronics from its fabrication Si wafer. 88

Figure 4.5. Schematic illustrations of basic procedures of the microbubble-driven delamination of thin-film nanoelectronics from its fabrication Si wafer. 88

Figure 4.6. Photograph of transferred thin-film electronic laminated on textile. 88

Figure 4.7. Microscope images showing the transferred Si NM-based resistor (Left), Si NRs-based diode (Middle), and Si NM-based transistor (Right) from its fabrication Si wafer. (Scale bars: 40, 200, and 250 μm, respectively.). 89

Figure 4.8. Corresponding electrical characteristics to each device before and after the transfer printing process. 89

Figure 4.9. Corresponding electrical characteristics to each device before and after the transfer printing process. 90

Figure 5.1. Schematic illustrations and optical images for the key process steps: (a) 3D imaging and custom direct ink writing (DIW), (b) steam etching, (c) metallization, (d) post-DIW, and (e) implementation on the epicardial surface of a murine heart. 95

Figure 5.2. (a) Results of differential scanning calorimetry (DSC) for the sponge-like foam. (b) Change in the resistance and stretchability of the custom-printed sensor array with respect to the plating time of Cu. 97

Figure 5.3. (a) Photographs of the custom-printed sensor array immersed in a warm water bath (35ºC) for 10 seconds. (b) Results of the bending stiffness of the custom-printed sensor array with respect to the thickness of the water-soluble medical tape. 97

Figure 5.4. Snapshot image of the MD simulation for the interfacial interaction energy of a SiO2-PS particle (left panel) and a SiO2-OH particle (right panel) with the surrounding resins. 98

Figure 5.5. Storage and loss modulus of the inks with respect to shear stress. 100

Figure 5.6. Photographs of various as-printed structures using the formulated ink with the weight ratio of 6.0:3.3:0.7. 101

Figure 5.7. Viscosity of the inks with respect to shear rate. 102

Figure 5.8. Change in the storage and loss modulus of the inks over time. 102

Figure 5.9. Cross-sectional side view of an SEM image for the sponge-like foam. 103

Figure 5.10. Change in the storage and loss modulus of the formulated ink with the weight ratio of 6.0:3.3:0.7 (left panel) and the ink with directly mixed Ag flakes (right panel) over time. 103

Figure 5.11. Stress-strain curves of the inks. Inset graph shows the corresponding results obtained from the ink with 6.0:3.3:0.7 ratio configured into an open mesh layout. 105

Figure 5.12. Mechanical hysteresis of the inks for 5 loading-unloading cycles at a strain of 50%. 105

Figure 5.13. Energy loss of the inks. 106

Figure 5.14. Change in the energy loss of the custom-printed sensor array with respect to a strain ranging from 30% to 70%. 106

Figure 5.15. Electrical hysteresis of the inks with respect to the strain from 10% to 50%. 107

Figure 5.16. Change in the resistance of the custom-printed sensor array with respect to the strain up to 150%. 107

Figure 5.17. Change in the resistance of the inks throughout 1,000 times of loading-unloading cycles with the strains ranging from 10% to 30%. 108

Figure 5.18. Change in the sheet resistance of the devices soaked in a bath of DI water (top panel), PBS (middle panel), and ethanol (bottom panel) for 12 hours. 108

Figure 5.19. Photographs of the custom-printed sensor arrays, each of which was customized to fit with the enucleated piglet, ovine, porcine, and bovine hearts from upper left to bottom right clockwise. 109

Figure 5.20. Schematic illustration of the cross-sectional view of the hearts. 110

Figure 5.21. (a) Schematic illustration of an experiment setup for the ex vivo measurement of epicardial ECG signals from the enucleated porcine heart. (b) Photograph of the device (total 64 electrodes) placed on the surface of the enucleated porcine heart. (c) Measurement results of the epicardial ECG signals by applying an artificial ECG waveform. 111

Figure 5.22. Photographs of the devices placed on the surface of (a) the enucleated porcine liver and (b) a human brain model. 112

Figure 5.23. Photographs of the custom-printed sensor arrays placed on the epicardial surface of a murine (left panel) and porcine heart (right panel). 113

Figure 5.24. Electrochemical impedance of the device soaked in a bath of PBS as a function of frequency. 114

Figure 5.25. Photographs of the devices with different thicknesses ranging from 50 μm to 300 μm placed on the epicardial surface of a murine heart. 115

Figure 5.26. Post-processed 3D data of the spatiotemporally recorded murine (left panel) and porcine (right panel) ECG signals. 115

Figure 5.27. Epicardial ECG signals obtained from the healthy murine (n = 5) and porcine hearts (n = 2). 116

Figure 5.28. The corresponding quantitative data of R-R interval, QRS duration, and J-point elevation. 116

Figure 5.29. Simultaneously measured ECG signals using the custom-printed sensor array (top panel) and a control 3-lead electrode set (bottom panel) on a murine heart. 117

Figure 5.30. Enlarged images of the custom-printed sensor array covering the entire ventricular epicardium. The red highlighted area indicates the regional myocardial infarction propagating toward the apex of the murine heart over time. 118

Figure 5.31. Measured epicardial ECG signals using the custom-printed sensor array. 119

Figure 5.32. (a) Epicardial ECG signals obtained from a murine myocardial infarction model (n = 5). (b) The corresponding quantitative data of R-R interval (left panel), QRS duration (middle panel), and J-point elevation (right panel). 119

Figure 5.33. Simultaneously measured ECG signals using a control 3-lead electrode set. 120

Figure 5.34. Representative global ECG data of ST-segment depression (top panel) and elevation (bottom panel) within seconds following left coronary artery ligation (blue arrows). 120

Figure 5.35. Representative ECG data with persistent ST-segment elevation at baseline and at 1, 15, and 30 minutes following left coronary artery ligation. 121

Figure 5.36. Schematic illustration of the experiment setup for simultaneous epicardial ECG recording and ultrasound imaging. 122

Figure 5.37. Photograph of the measurement setup for simultaneous epicardial ECG recording and ultrasound imaging..... 123

Figure 5.38. Representative short-axis ultrasound image displaying the custom-printed sensor array (yellow circle) along with the epicardium (blue circle) and endocardium (red circle) of the heart..... 123

Figure 5.39. Representative ultrasound images of relatively thick (200 μm-thick; top panel) and thin (50 μm-thick; bottom panel) devices placed on the epicardial surface of a fixed murine heart. 124

Figure 5.40. Post-processed 3D image reconstructed from the spatiotemporally recorded epicardial ECG and ultrasound signals after 60 seconds post-ligation..... 124

Figure 5.41. Results of cell compatibility assay for the custom-printed sensor array with heart myoblast (H9C2) cells in a 24-well plate, as measured using a colorimetric assay kit. 126

Figure 5.42. Representative histological cross-sectional views of the murine cardiac tissues that were stained with both hematoxylin-eosin (H&E; left panel) and Masson's trichrome (MTC; right panel) on day 14 post-implant of the custom-printed sensor array..... 126

Figure 5.43. (a) Overview of granuloma and aorta on day 7 post-implant. (b) Magnified views (at 20×) of granuloma formation on day 7 post-implant. The boxed area identifies the presence of macrophages, multi-nucleated giant cells, and fibroblasts. The inset image demonstrates macrophages containing phagocytized debris resulting from the intralesional device. (c) Magnified views (20×) of macrophages and multi-nucleated giant cells at the surface of the implanted device (red arrows). The neutrophils (blue arrows) suggest acute to chronic inflammation directed at the device. 127

Figure 5.44. (a) Day 1 epicardium at 20 × (left) and 40 × (right) magnification. The epicardium presents at five-times normal thickness and is comprised of neutrophils (red arrows). (b) Day 7 epicardium. The double-headed line indicates a thickening of epicardium by mononuclear cells and fibroblasts due to chronic inflammatory response. (c) Day 14 epicardium. The double-headed line indicates a worsening of epicardial thickening. The presence and epithelioid morphology of macrophages (red arrow) indicate chronic granulomatous response (e.g., foreign body response) at the surface of the implanted device. The neutrophils (blue arrow) suggests that acute chronic inflammation directed towards the implanted device. (d) Progression of epicardial thickness measured using ImageJ (n = 5). The measurements were spaced at 100 µm perpendicularly from the epicardial surface to the underlying muscle layer. 128

Figure 5.45. (a) Chronic epicarditis observed on day 7 post-implant. (b) Pericardial to epicardial adhesion with intralesional device observed on day 14 post-implant. 129

Figure 5.46. Z-stack fluorescence images of a BSA-FITC (6 mg/ml) coated on the printed device as compared to control groups made of the SE 1700 ink and the Sylgard 184 ink and prepared on a pristine glass, from upper left to bottom right clockwise. 130

Figure 5.47. Results of one-way ANOVA tests with Bonferroni correction (n = 5 per group). Fluorescence intensity is shown as average ± standard deviation (**p < 0.001). 130

Figure 5.48. Representative ultrasound images of the left ventricle of a murine heart on 0, 1, 7, and 14 days implantation of the custom-printed sensor array. 131

Figure 5.49. Results of the ejection fraction of the murine heart post-implant. 131

ABSTRACT

Advances in additive manufacturing technologies enable the rapid, high-throughput generation of mechanically soft microelectromechanical devices with tailored designs for many applications spanning from optical to biomedical applications. These devices can be softly interfaced with biological tissues and mechanically fragile systems, which enables to open up a whole new range of applications. However, the scalable production of these devices faces a significant challenge due to the complexity of the microfabrication process and the intolerable thermal, chemical, and mechanical conditions of their flexible polymeric substrates. To overcome these limitations, I have developed a set of advanced additive manufacturing technologies enabling (1) mechanics-driven manufacturing of quasi-three-dimensional (quasi-3D) nanoarchitectures with arbitrary substrate materials and structures; (2) repetitive replication of quasi-3D nanoarchitectures for infrared (IR) bandpass filtering; (3) electrochemical reaction-driven delamination of thin-film electronics over wafer-scale; (4) rapid custom printing of soft poroelastic materials for biomedical applications.

First, I have developed a new mechanics-driven nanomanufacturing method enabling large-scale production of quasi-3D plasmonic nanoarchitectures that are capable of controlling light at nanoscale length. This method aims to eliminate the need for repetitive uses of conventional nanolithography techniques that are time- and cost-consuming. This approach is innovative and impactful because, unlike any of the conventional manufacturing methods, the entire process requires no chemical, thermal, and mechanical treatments, enabling a large extension of types of receiver substrate to nearly arbitrary materials and structures. Pilot deterministic assembly of quasi-3D plasmonic nanoarrays with imaging sensors yields the most important advances, leading to improvements in a broad range of imaging systems. Comprehensive experimental and computational studies were performed to understand the underlying mechanism of this new manufacturing technique and thereby provide a generalizable technical guideline to the manufacturing society. The constituent quasi-3D nanoarchitectures achieved by this manufacturing technology can broaden considerations further downscaled plasmonic metamaterials suggest directions for future research.

Second, I have developed mechanics-driven nanomanufacturing that provides the capability to repetitively replicate quasi-3D plasmonic nanoarchitectures even with the presence of an

extremely brittle infrared-transparent spacer, such as SU-8, thereby manipulating IR light (e.g., selectively transmitting a portion of the IR spectrum while rejecting all other wavelengths). Comprehensive experimental and computational studies were performed to understand the underlying nanomanufacturing mechanism of quasi-3D plasmonic nanoarchitectures. The spectral features such as the shape of the transmission spectrum, peak transmission and full width at half maximum (FWHM), etc. were studied to demonstrate the bandpass filtering effect of the assembled quasi-3D plasmonic nanoarchitecture.

Third, I have developed an electrochemical reaction-driven transfer printing method enabling a one-step debonding of large-scale thin-film devices. Conventional transfer printing methods have critical limitations associated with an efficient and intact separation process for flexible 3D plasmonic nanoarchitectures or bio-integrated electronics at a large scale. The one-step electrochemical reaction-driven method provides rapid delamination of large-scale quasi-3D plasmonic nanoarchitectures or bio-integrated electronics within a few minutes without any physical contact, enabling transfer onto the target substrate without any defects and damages. This manufacturing technology enables the rapid construction of quasi-3D plasmonic nanoarchitectures and bio-integrated electronics at a large scale, providing a new generation of numerous state-of-art optical and electronic systems.

Lastly, I have developed a new printing method enabling the direct ink writing (DIW) of multidimensional functional materials in an arbitrary shape and size to rapidly prototype stretchable biosensors with tailored designs to meet the requirement of adapting the geometric nonlinearity of a specific biological site in the human body. Herein, we report a new class of a poroelastic silicone composite that is exceptionally soft and insensitive to mechanical strain without generating significant hysteresis, which yields a robust integration with living tissues, thereby enabling both a high-fidelity recording of spatiotemporal electrophysiological activity and real-time ultrasound imaging for visual feedback. Comprehensive *in vitro*, *ex vivo*, and *in vivo* studies provide not only to understand the structure-property-performance relationships of the biosensor but also to evaluate infarct features in a murine acute myocardial infarction model. These features show a potential clinical utility in the simultaneous intraoperative recording and imaging on the epicardial surface, which may guide a definitive surgical treatment.

1. INTRODUCTION

A version of this chapter was previously published by *Advanced Materials* [https://doi.org/10.1002/adma.201902051].

1.1 Background

Multidimensional flexible architecture has attracted a great deal of attention in the past decade for the production of diverse optical and biomedical systems. Different forms of flexible materials and manufacturing techniques have been utilized by relying on a set of parallel protocols to print conductive and dielectric materials and miniaturized electronic microchips for their rational integration into functional and flexible structures with prescribed geometries and configurations. The following sections highlight conventional manufacturing technologies for flexible architectures. Table 1.1 presents a summarized overview of these methods in terms of the working principles, printable materials, and key advantages and challenges.

Herein, we report advanced manufacturing technologies including mechanic- and electrochemical reaction-driven manufacturing, and rapid custom printing, which have been demonstrated in optical and biomedical applications. We developed several system-level applications of the most promising devices for the novel optical and biomedical sensing platform. The basic materials, design layouts, data processing, and transmission configurations, and their implications are also discussed. Also, we illustrate all the key developments in optical and biomedical systems in this report and discuss the needs and future work to expand the scope.

Table 1.1. Printing methods in terms of the working principles, printable materials, and key advantages and challenges.

Printing Strategy	Working Principles	Printable Materials	Key Advantages	Challenges
Transfer Printing	Sacrificial Layer Etching-Based Transfer Printing	Si/Ge/GaAs/ GaN/InP	Available to various forms of monocrystalline semiconducting materials	Slow etching process of the sacrificial layer
				Requirement for post-fabrication process on receiver substrates
	Controlled spalling-driven method	Si/Ge/III–Vs	Transfer of fully fabricated circuits over wafer-scale	Requirement for post-etching of residual substrate material
				Handling difficulty for the stressed/curved thin-films
	Interfacial Layer Delamination-Based Transfer Printing	Integrated nano-circuits and sensors	No requirement for post-fabrication	Limited in the use of monocrystalline semiconducting materials
			Multiple times reusable donor wafer	

1.2 Overview of conventional manufacturing technologies

Traditionally, microelectronics and sensors have been fabricated by using standard semiconductor lithography techniques that typically involve the use of photo-sensitive polymers, which are extremely well suited to the tasks to define complex microscale patterns on a rigid, flat wafer. However, significant challenges exist in adopting these techniques directly for mechanically flexible and non-flat substrates that are particularly made of biocompatible soft elastomers, mainly due to the required chemical and thermal treatments causing potential damages to the substrates. To circumvent this problem, various forms of transfer printing approaches have been established.(Carlson et al., 2011; M. K. Choi et al., 2015; S. Kim et al., 2010; B. H. Lee et al., 2007; Linghu et al., 2019; Meitl et al., 2006; Wie et al., 2018; Zhuocheng Yan et al., 2017) In general, these approaches represent a set of techniques that enable the deterministic integration of various classes of materials with a foreign receiver substrate in a large-scale and defect-free manner. These approaches offer remarkable opportunities to construct high-performance electronics and sensors on diverse substrates in a spatially controlled manner that produces the most complex and sophisticated configurations. These sections summarize the most promising transfer printing methods, organized according to their working principles such as *i)* sacrificial layer-etching-based transfer printing,(Feng et al., 2007; Meitl et al., 2006) *ii)* controlled spalling-based transfer printing,(Bedell et al., 2012; Shahrjerdi et al., 2013) and *iii)* interfacial layer delamination-based transfer printing(C. H. Lee, Kim, & Zheng, 2011; Wie et al., 2018; Y. Zhang, Liu, & Xu, 2017). These exemplary transfer printing methods have enabled the realization of custom design services at the consumer level for producing diverse microscale electronics and sensors, demonstrating their commercial viability.

1.2.1 Sacrificial layer etching-based transfer printing

Figure 1.1 (left) describes a particularly powerful transfer printing method due to its natural capability to incorporate device-grade monocrystalline semiconducting materials in which the materials are picked up from their growth/fabrication substrates with a soft elastomeric stamp made of polydimethylsiloxane (PDMS) and then printed to a foreign receiver substrate in a parallel manner.(Meitl et al., 2006) The pick-and-place steps occur at room temperature and can be repeated for large-area assembly and/or heterogeneous materials integration in 2D or 3D layouts

at the microscale by using a micro-XYZ manipulator under microscope examinations. The success of this method relies principally on the competition of the interfacial adhesion and delamination among the printable materials, elastomeric stamp, and donor/receiver substrates, wherein the adhesion between the solid films and the stamp depends on peeling rate (that is, kinetically controllable) due to the intrinsic viscoelasticity property of the elastomeric stamp. Specifically, a rapid peeling (≥~10 cm/sec) of the stamp from the donor wafer leads to the delamination of the materials to the surface of the stamp while a sufficiently slow peeling (≤~1 mm/sec) of the stamp from the receiver substrate allows the materials to remain behind on the surface of the receiver substrate. Transfer printing with various classes of monocrystalline semiconducting materials, such as Si, Ge, GaAs, GaN, and InP in various forms ranging from 0D dots to 1D wires and ribbons, to 2D membranes, and 3D architectures have been successfully demonstrated in this way.

Figure 1.1 (right) shows a schematic diagram of critical energy release rate (G_{crit}) at the interface of film/substrate ($G_{film/substrate}$) and stamp/film ($G_{stamp/film}$) versus the peeling rate (v).(Feng et al., 2007; Gent & Lai, 1994; Hutchinson & Suo, 1991) To facilitate precise adhesion control of the $G_{film/substrate}$ during the pickup step, an additional layer of chemically dissolvable sacrificial film can be inserted in between the semiconducting materials and the donor wafer substrate. An example approach involves the use of multiple stacked semiconductor (i.e., GaAs)/sacrificial (i.e., AlGaAs) films that are epitaxially grown on a host GaAs wafer, followed by immersing in a proper etchant solution (i.e., hydrofluoric acid, HF) to remove the sacrificial layer exclusively, resulting in the physical release of the remaining semiconducting materials.(Melosh et al., 2003) Subsequently, the above-mentioned pick-and-place operation can be repeatedly employed to deliver the released semiconducting materials to a receiver substrate in a spatial layout. During the printing step, a pulsed laser beam (power: 30W; wavelength: 805 nm; minimum pulse width: 1 ms) can be also applied to facilitate precise adhesion control of the $G_{stamp/film}$ where the laser beam is focused at the interface while the transparent stamp allows the laser radiation to transmit through. (S. Kim et al., 2010) Here, the picked solid materials serve as a heat source to raise the temperature of the stamp by 250-300ºC, yielding thermal expansion and curvature in the stamp and leading to the physical release of the solid materials from the stamp.(Yi et al., 2018) This laser-assisted approach is to eliminate the need for precise control of the interfacial adhesion between the stamp and the receiver substrate, regardless of the pitch size and density of the printed structures. The

subsequent step includes the post-fabrication required for defining other necessary conducting, dielectric and encapsulation layers on the receiver substrate to yield the complete functional device. This pick-and-place transfer printing method has provided great achievements over the past decade wherein various classes of electronics and sensors have been successfully realized on a range of flexible, stretchable and wearable substrates including polyurethane, polyimide and silicone elastomers.(Jong-Hyun et al., 2006; Menard, Lee, Khang, Nuzzo, & Rogers, 2004; Yi et al., 2018) However, the choice of the receiver substrates remains impeded by which the receiver substrate materials must contain a certain degree of thermal and chemical resistance to accommodate the post-fabrication conditions. Another challenge exists in the printed structures configured with a high pitch or low density which may give rise to stamp collapse, specifically when high printing strength is subjected to compensate for misalignments between the stamp and the substrate. This may increase the risk of potential damages to both the donor and receiver substrates.

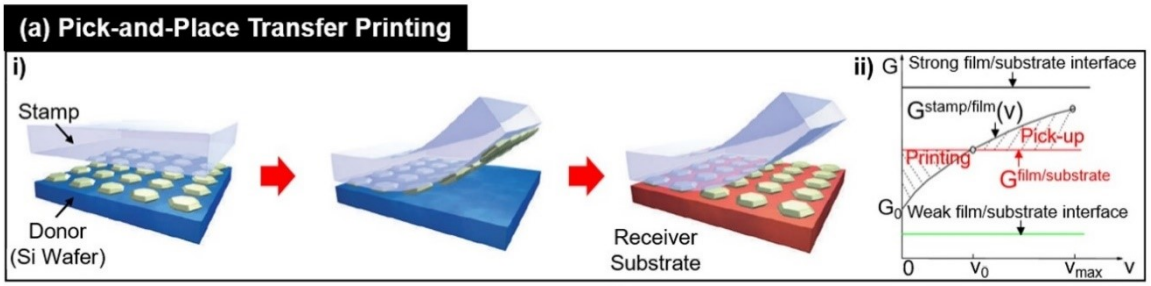

Figure 1.1. Pick-and-place transfer printing method. i) Schematic illustration of the process flow by using an elastomeric stamp.(Meitl et al., 2006) ii) Schematic diagram of critical energy release rates for the film/substrate interface and the stamp/film interface.(Feng et al., 2007)

1.2.2 Controlled spalling-based transfer printing

Figure 1.2 (left) shows another notable transfer printing method by exploiting a controlled thermal spalling that occurs underneath and parallel to the top surface of the donor wafer. The process begins by fabricating complete electronics on a conventional wafer through standard microfabrication technology without any limitation in the use of chemical and thermal processes. The next step involves depositing a relatively thick metal layer such as Ni (6 μm), Ag (20 μm), and Al (50 μm) on the top surface of the donor wafer by using either sputtering or screen printing to serve as a stress inducer. (Dross et al., 2007) Subsequent rapid annealing of the entire structure at >900°C for a few seconds in a belt furnace followed by cooling down leads to a large thermal

contraction between the stress inducer layer and the donor wafer, yielding stresses underneath the wafer to crack the top layer. As a next, the residual wafer materials and buffer layer are chemically etched (e.g. Ge film removed from hydrogen peroxide, H_2O_2) while the donor wafer is required to be polished for recycle.(Shahrjerdi et al., 2013) The basic mechanism of this method relies on the controlled spalling that can be propagated from an edge of the donor wafer through the other end, allowing for wafer-scale processing. The stress field of this controlled spalling is comprised of both pure opening stress and the shear stress components at the crack tip where the crack tends to follow the trajectory at which the shear stress can be minimized (Fig. 1.2, right). (C. H. Lee, Kim, & Zheng, 2014) The equilibrium depth of the spalling typically appears at the location a few microns below the top surface of the wafer which is underneath the pre-fabricated thin-film electronics. The spalling depth is determined by adjusting the thickness of the stress inducer layer. The use of this method has generated a wide variety of flexible electronics such as thin-film integrated circuits,(Shahrjerdi & Bedell, 2013) photovoltaics(Bedell et al., 2012; Shahrjerdi et al., 2013) and energy harvesters(Hwang et al., 2014) by exploiting various classes of epitaxially grown monocrystalline semiconducting elements including Si, Ge and III–Vs. Although this method has not been utilized for biomedical and optical applications yet, the wafer-scale integration of monocrystalline semiconducting elements-based electronics provides a great potential for its future applications in high-performance electronics and sensors. However, challenges remain in the requirement of the post-etching process to remove residual substrate materials and the additional mechanical polishing step to remove kerfs on donor wafer for recycles. The required special handling for the stressed and curved thin-films after the spalling process yields an impediment to be overcome.

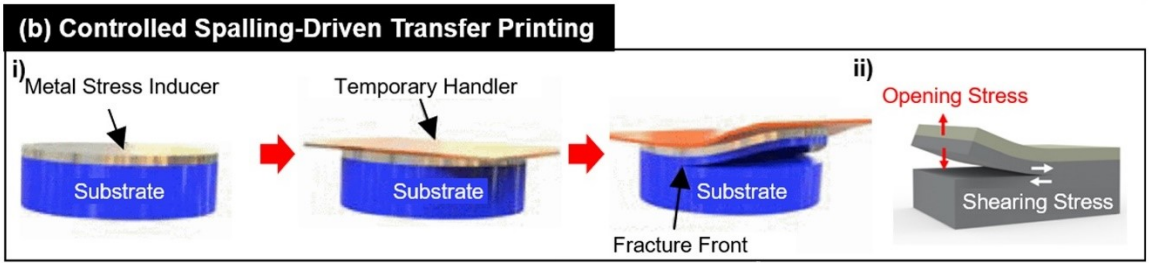

Figure 1.2. Controlled spalling-driven transfer printing method. i) Schematic illustration of the process flow by exploiting controlled thermal spalling.(Alharbi, Nasri, Wu, & Shahrjerdi, 2016) ii) Schematic illustration of the stress field in the spalling fracture mode.(C. H. Lee et al., 2014)

1.2.3 Interfacial layer delamination-based transfer printing

In the above-mentioned transfer printing methods, the donor fabrication wafer is often sacrificed by chemical etching or spalling, and cannot be directly recycled. More recently, interfacial layer delamination-based transfer printing methods are developed in which thin-film electronics can be physically delaminated from the fabrication substrate over wafer-scale under manipulated conditions such as induced chemomechanics reactions at the interface,(C. H. Lee et al., 2012; C. H. Lee et al., 2014; C. H. Lee et al., 2013; Wie et al., 2018) and precisely controlled weak interfacial adhesion,(Fowkes, 1963; D. H. Park et al., 2019) all in a defect-free manner that allows the donor wafer to be reused for next fabrication cycles. This aspect serves as a major cost-saving factor in the manufacturing schemes. Figure 1.3 (left) schematically describes the entire transfer printing protocols of the most recent demonstration:(Wie et al., 2018) *i)* The process begins by fabricating desired thin-film electronics on a Si wafer that is coated with a ductile metal film such as Ni (~300 nm) and diluted polyimide (1:1 mixture of 1-methyl-2-pyrrolidinone and polyimide, ~300 nm), *ii)* The next step involves mechanical peeling of the thin-film electronics with a temporary handling holder such as thermally releasable tape (Nitto Denko) in distilled (DI) water at room temperature, which allows the bottom Ni film together with the thin-film electronics to be cleanly delaminated from the Si wafer, *iii)* The physically peeled thin-film electronics can be then pasted to the surface of an arbitrary substrate or surface such as papers, building windows and flowerpots, thereby allowing such everyday objects to provide useful electronic capabilities, and *iv)* Removal of the temporary handling holder from the surface completes the entire process.

The basic underpinned mechanism of defect-free interfacial debonding relies on a chemomechanics reaction with water molecules at the debonding tip. Figure 1.3 (right) shows representative experimental (dots) and computational (lines) results that reveal the relationship between peeling strength (p) versus peeling distance (d). These results indicate that the debonding strength under wet (water) condition is largely decreased compared to that under dry condition (20% relative humidity), and also confirm that the presence of water indeed reduces the interfacial adhesion and thereby promote the intact debonding. However, this method is limited in the performance of the resulting electronics because the epitaxial growth of monocrystalline semiconductor materials is not allowed due to the bottom Ni film. To overcome this, a hybrid transfer printing approach can be used: *i)* The first step involves the use of the above-mentioned pick-and-place transfer printing method to define homogeneous or heterogeneous combinations of

monocrystalline semiconducting materials on desired locations of the D-PI/Ni/Si wafer, followed by standard microfabrication processes to yield the complete electronics, and then *ii)* the chemomechanics-driven interfacial debonding process is followed to physically separate the pre-fabricated thin-film electronics from the Si wafer and subsequently print onto an arbitrary substrate or surface.

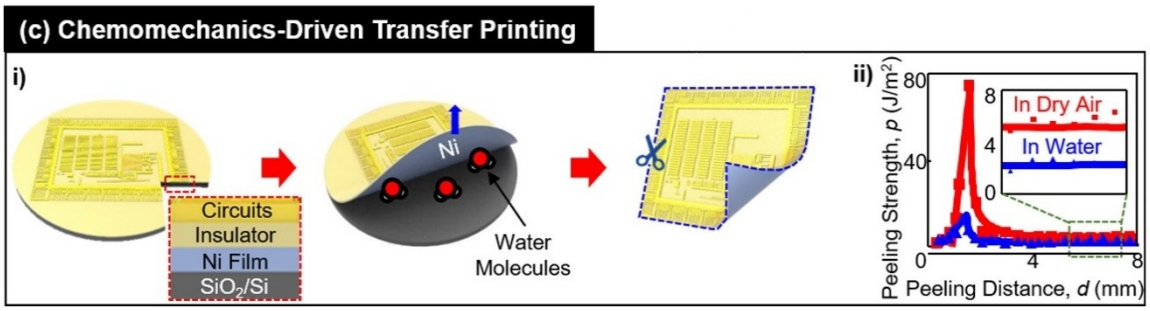

Figure 1.3. Chemomechanics-driven transfer printing method. i) Schematic illustration of the process flow by exploiting controlled interfacial delamination phenomenon. ii) Experimental and finite-element analysis (FEA) results of peeling strength versus peeling distance under wet (water) and dry conditions.(Wie et al., 2018)

2. MECHANICS-DRIVEN MANUFACTURING OF QUASI-THREE-DIMENSIONAL NANOARCHITECTURES

A version of this chapter was previously published by *Nano Letters* [https://doi.org/10.1021/acs.nanolett.9b02598].

2.1 Background

Interaction of incident light with three-dimensional (3D) metal-dielectric composite nanoarrays provides unique capabilities to manipulate light at nanoscale length.(Atwater & Polman, 2010; Cheben, Halir, Schmid, Atwater, & Smith, 2018; Naldoni, Shalaev, & Brongersma, 2017; Soukoulis & Wegener, 2010; Stockman et al., 2018; Yang, Yao, Rho, Yin, & Zhang, 2012; X. Zhang & Liu, 2008) Diverse types of 3D or quasi-3D plasmonic nanoarrays with tailored feature shapes, sizes, and configurations have been explored for a broad range of light-driven sensors and actuators such as imagers, bio-sensors, lasers, and antennas.(Franklin, Frank, Wu, & Chanda, 2017; Q. Huang, Peh, Hergenrother, & Cunningham, 2016; Ni, Wong, Mrejen, Wang, & Zhang, 2015; Safaei et al., 2018; Stewart et al., 2006; Vazquez-Guardado et al., 2016; M. Zhang, Lu, Ge, & Cunningham, 2014) Traditionally, the construction of 3D plasmonic nanoarrays has been largely relied on the use of nanolithography techniques by exploiting either electron-beam lithography (EBL), focused ion-beam lithography (FIB), or laser interferometry (IL), but their laborious, complex, and time-consuming nature impedes practical applications.(Jang et al., 2016; Luo, Jiang, Liu, & Si, 2018; Y. Wang et al., 2015; Xia, Ku, Lee, & Brueck, 2011) Besides, the nanolithography processes often require the use of thermal and chemical treatments, leading to an additional increase of complexity and risk in protecting the substrate materials. Alternative strategies involve the use of micro/nanoscale 3D printing techniques such as nanoimprinting and modular micro-transfer printing, allowing for deterministic integration of 3D plasmonic nanoarrays with a foreign receiver substrate, and thereby circumventing the incompatibility of the nanolithography conditions with substrate materials.(Chanda, Shigeta, Gupta, et al., 2011; Chanda, Shigeta, Truong, et al., 2011; Gao et al., 2014; S. Lee et al., 2016) Nevertheless, the choice of receiver substrates remains limited by the required physical contact forces during printing steps, yielding an increased risk of potential damages to receiver substrates particularly composed of mechanically fragile materials and structures.

Herein, we report a new 3D nanoassembly method that enables intact separation of various types of quasi-3D plasmonic nanoarrays from their donor fabrication substrate and then transfer them to a preferred receiver substrate in a way that allows the donor substrate to be recycled for a cost- and time-saving solution. Unlike conventional approaches, the entire process of this method exclusively occurs in distilled water under ambient conditions without the need of further chemical, thermal, or mechanical treatments, and thereby can substantially extend the types of receiver substrate to nearly arbitrary materials and structures. Pilot assembly of specifically designed quasi-3D plasmonic nanoarrays with mid-wavelength infrared type-II superlattice (MWIR-T2SL)-based hybrid pixel detector (HPD) in a defect-free manner demonstrates the effectiveness of this method in the deterministic enhancement of the detection performances. Both analytical predictions and experimental validations reveal the underlying optical and physical properties of the resulting optical systems to confirm the integrity after the assembly process.

2.2 3D nanoassembly method

Figure 2.1 shows schematic illustrations of the physical separation of quasi-3D plasmonic nanoarrays from their donor Si substrate that is configured with periodic circular patterns at nanoscale. Here, these patterns are pre-formed on the donor Si substrate by exploiting conventional EBL,(Y. Chen, 2015; Vieu et al., 2000) of which representative scanning electron microscopy (SEM) images appear in Figure 2.2. The process begins by depositing a sacrificial Ni layer (10 nm) and Au plasmon film (50 nm) by electron-beam (e-beam) evaporator on a donor Si substrate, followed by spin-casting of a dielectric spacer using either poly(methyl methacrylate) (PMMA), benzocyclobutene (BCB), or SU-8 to form an optical cavity (Figure 2.1, left). The next step involves immersing the entire structure in a bath of etchant (TFB, Transene), allowing the etchant to penetrate through the dielectric spacer(Kusy, Whitley, & Kalachandra, 2001) and then remove the underneath Ni layer exclusively. This allows the remaining layers to sink and adhere to the surface of the donor Si substrate by weak van der Waals adhesive force (Figure 2.1, middle). The resulting structure is then rinsed with distilled water to keep the dielectric spacer wet while the top surface is wiped with a cleanroom swab to stay dry where a water-soluble tape (WST, Aquasol) is attached to serve as a temporary handling holder. Finally, mechanical peeling of the WST occurs at a constant rate of 50 mm/min by using an automated tool (Mark-10), resulting in intact separation of the quasi-3D plasmonic film from the donor Si substrate (Figure 2.1, right). Figure

2.3 provides an optical image of a representative specimen configured with an array (1×1 cm^2) of quasi-3D nanopost configurations, which is peeled intactly from its donor Si substrate with a WST. Subsequent placement of the WST on the surface of water leads to complete dissolution within ~10 min at room temperature, allowing the remaining quasi-3D plasmonic nanoarrays to stay afloat on the water surface (Figure 2.4).

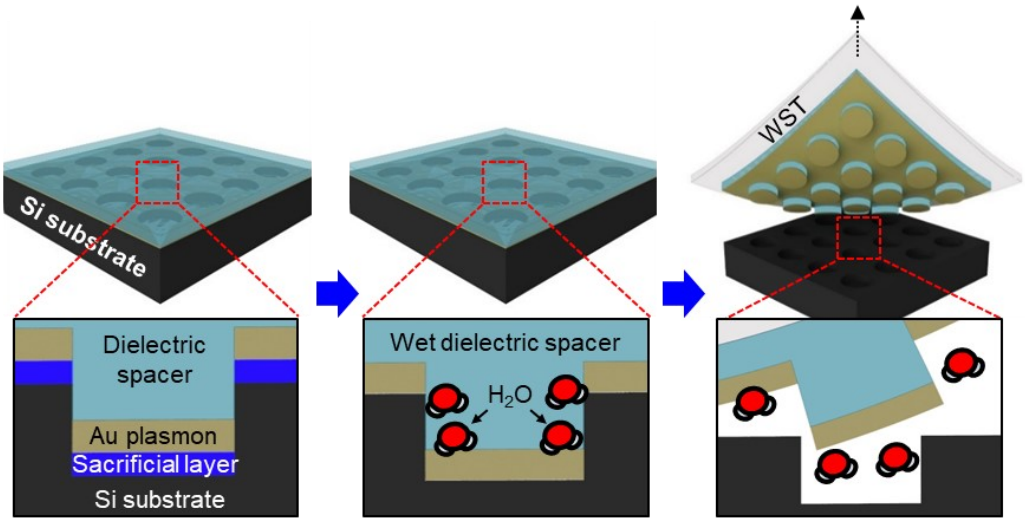

Figure 2.1. Schematic illustration for physical separation of quasi-3D plasmonic nanoarrays from its donor Si substrate

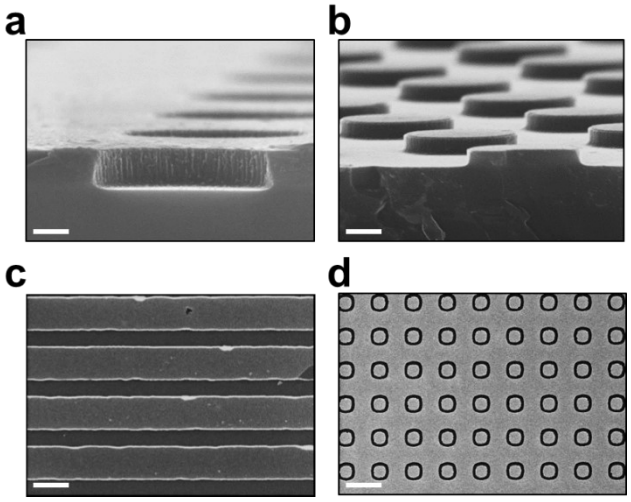

Figure 2.2. SEM images of various nanopatterns on donor Si substrate configured with circular-shaped nanoholes (a), circular-shaped nanoposts (b), subwavelength nanowire gratings (c), and ring-shaped disks (d). Scale bars are 200 nm, 400 nm, 950 nm, and 3 μm, respectively.

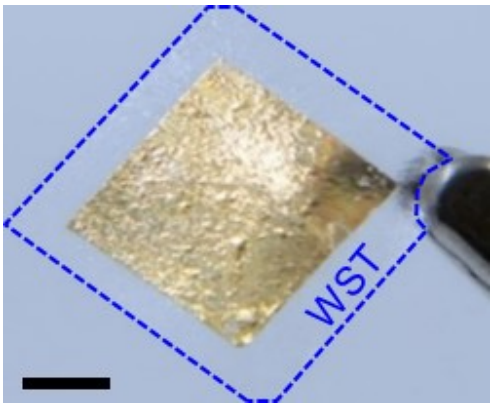

Figure 2.3. Photo of a plasmonic film configured with quasi-3D nanoposts on a WST after the separation. Scale bar is 3.5 mm.

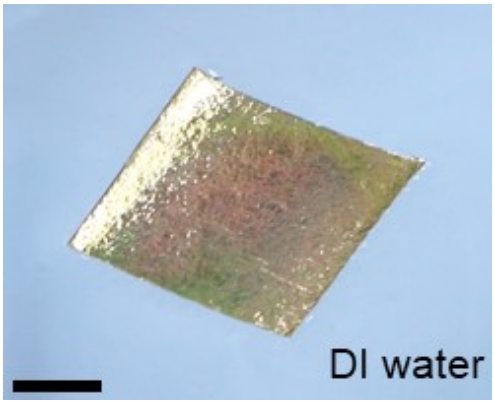

Figure 2.4. Photo of the plasmonic film afloat on the surface of water after the dissolution of the WST. Scale bar is 3.5 mm.

The next 'assembly' step occurs by exploiting a custom-setting in which a plastic petri dish of distilled water (~50 mL) is placed on a probe station (Signatone) where a preferred receiver substrate is immersed and anchored underneath the water by a distance of <1 mm from the surface (Figure 2.5). Details of this setting appear in Figure 2.6. Here, the quasi-3D plasmonic nanoarrays remain afloat on the water surface and can be slipped with full XY movement and 360° rotation by using a micromanipulator (Signatone) for precise positioning and alignment. Upon proper positioning, the water in the petri dish is slowly removed, or evaporated, until the plasmonic nanoarrays reach the surface of the receiver substrate and remain contacted via van der Waals adhesion force. Upon any misalignment, the receiver substrate is obliquely soaked in water with an angle of ~20° from the surface,(Cheng et al., 2013) allowing the misaligned plasmonic

nanoarrays to be released from the receiver substrate by the surface tension of water. Finally, the assembled structure is dried at room temperature to secure the interfacial bonding or, if allowed by the receiver substrate, can be annealed at ~60°C for 10 min in a convection oven to substantially promote the adhesion,(W. T. Li, Charters, Luther-Davies, & Mar, 2004) by more than 50% (Figure 2.7). The entire process of this method is also schematically illustrated in Figure 2.8.

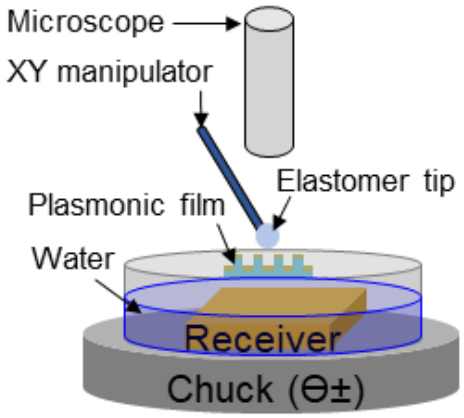

Figure 2.5. Schematic illustration of the microscale positioning and alignment setup.

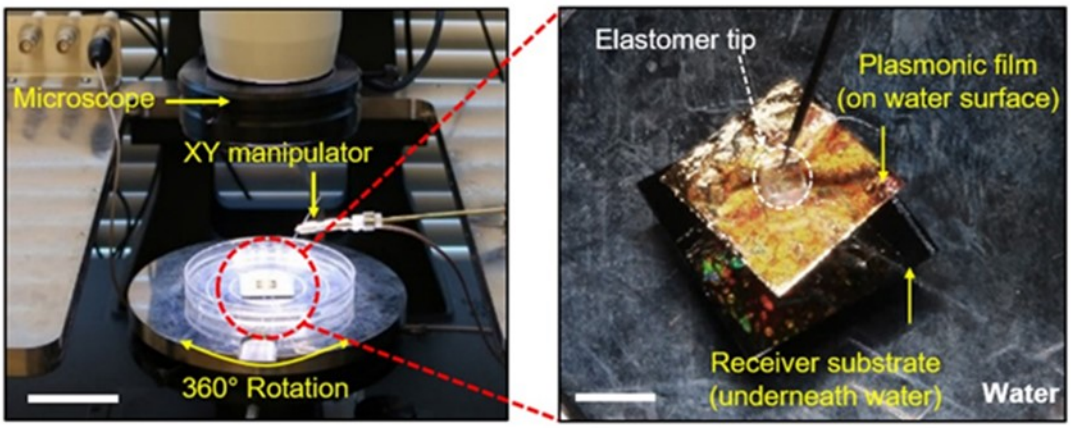

Figure 2.6. Photos of a setting for micro-scale positioning and alignment. Scale bar is 7.5 cm and 5 mm from the left.

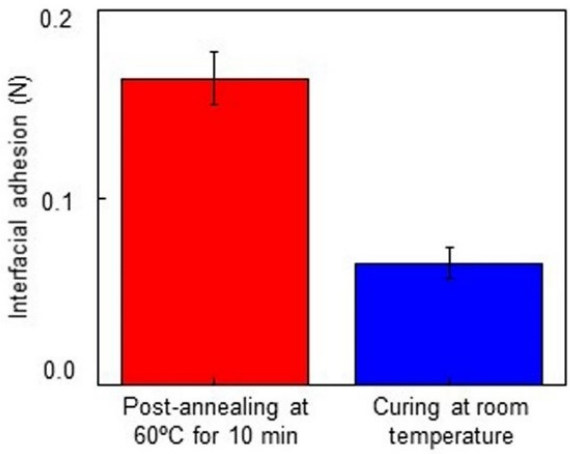

Figure 2.7. Schematic illustration of the microscale positioning and alignment setup.

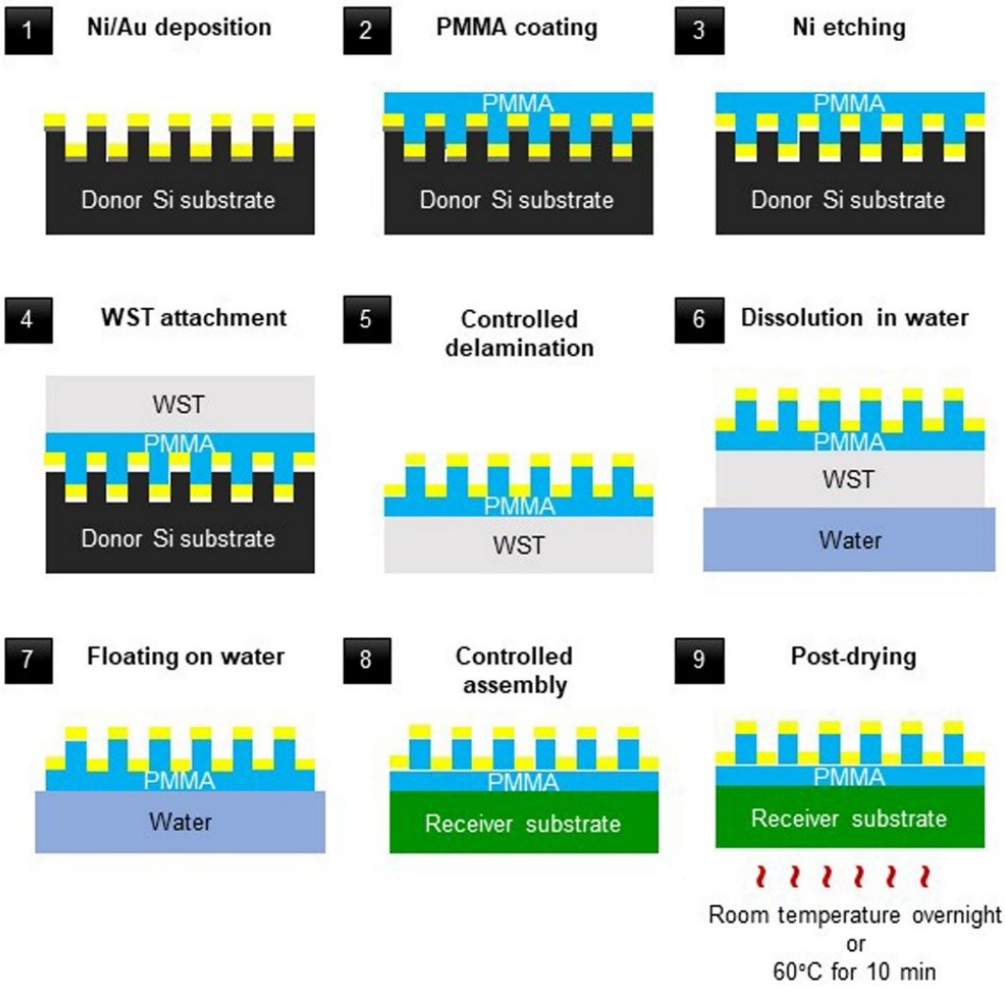

Figure 2.8. Schematic illustrations for the entire process of the 3D nanoassembly method.

Figure 2.9 provides a photo (left) and an SEM image (right) of the transferred quasi-3D plasmonic film on a model foreign receiver substrate such as a double-side polished (DSP) Si wafer. The results display no visual defects or damages over the area. The optical images in Figure 2.10 confirm the integrity of the donor Si substrate which allows its multiple recycles through post-cleaning inspections and thereby can serve as a major cost- and time-saving factor (Figure 2.11). Comprehensive evaluations by exploiting different types of dielectric spacers such as BCB or SU-8 produce consistent results (Figure 2.12).

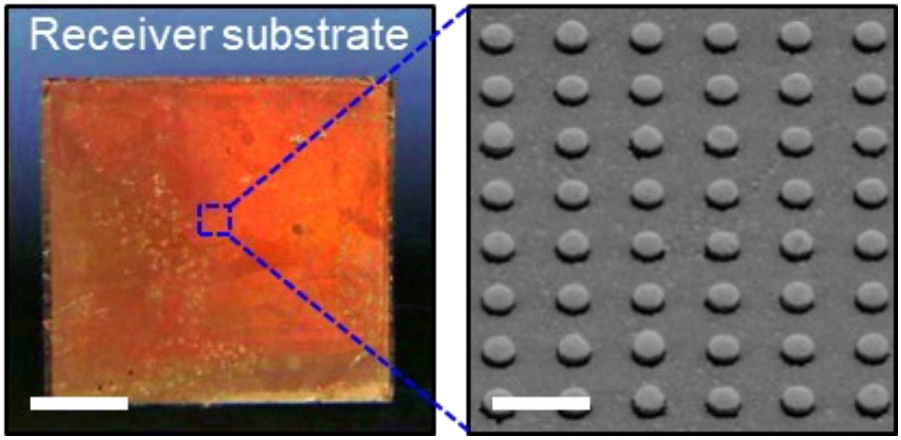

Figure 2.9. Photo (left) and enlarged SEM image (right) of the transferred plasmonic film on a receiver Si substrate. Scale bars are 3 mm (left) and 4 μm (right)

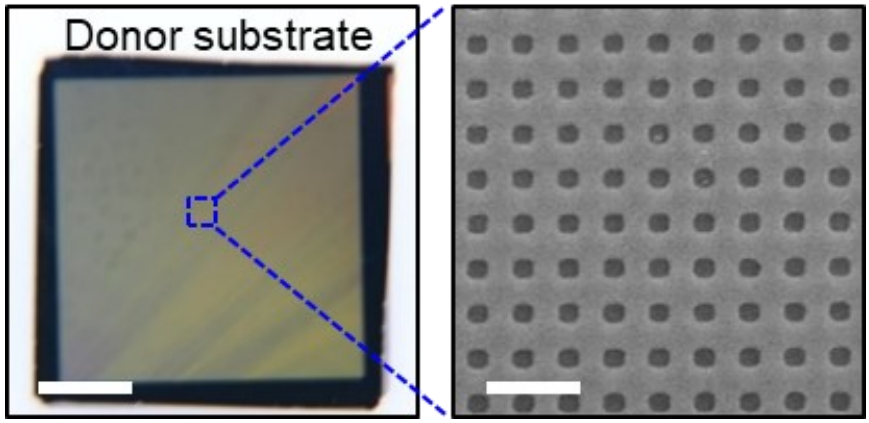

Figure 2.10. Photo (left) and enlarged SEM image (right) of the donor Si substrate. Scale bars are 3 mm (left) and 6.5 μm (right).

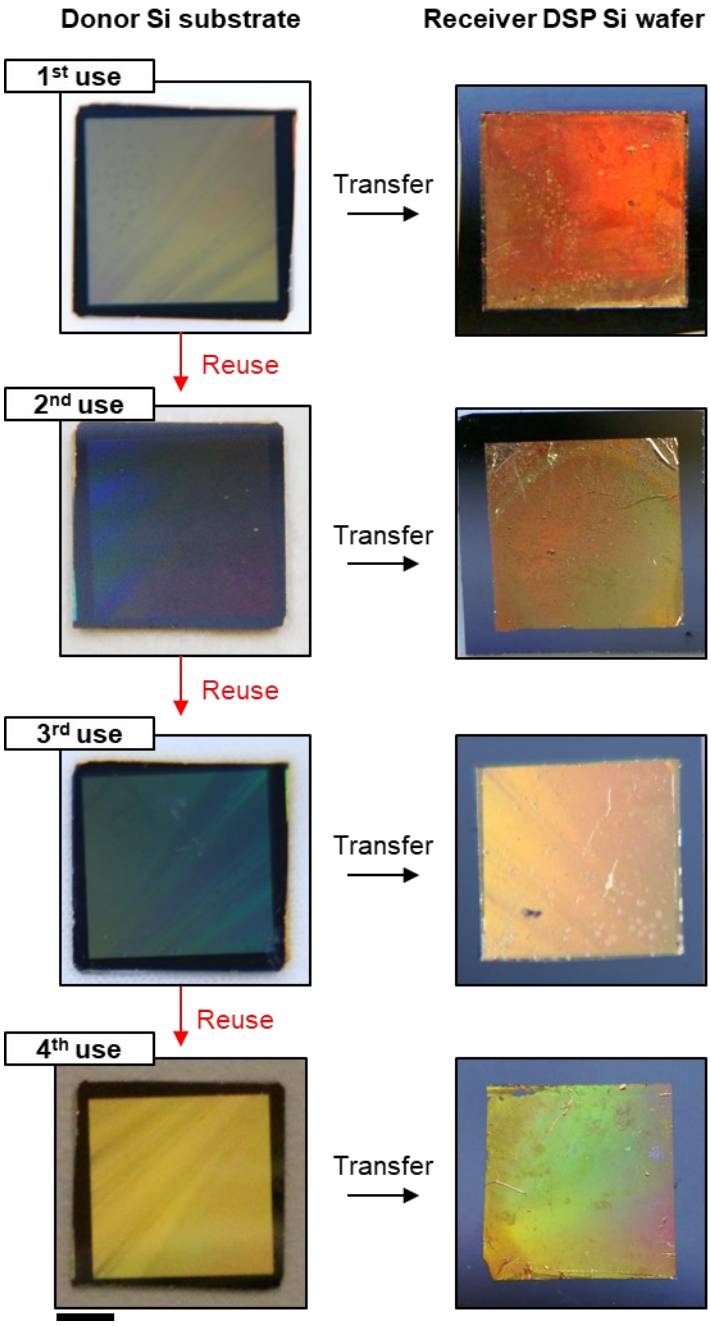

Figure 2.11. Photos of a donor Si substrate through 4 times recycle for the transfer of quasi-3D plasmonic nanoarrays to receiver DSP wafers. Scale bar is 4.3 mm.

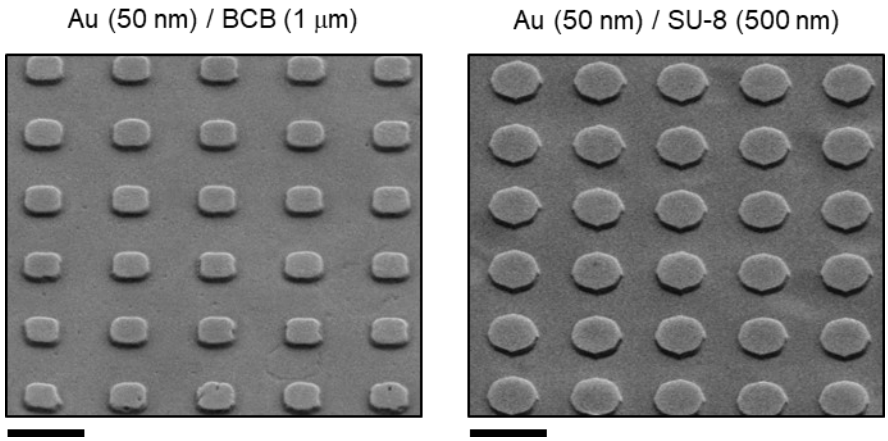

Figure 2.12. SEM images of the transferred quasi-3D nanoposts consisted of BCB (left) and SU-8 (right) as a dielectric spacer. Scale bars are 3.0 μm.

2.3 Mechanism study and mechanics analysis

The interfacial separation between quasi-3D plasmonic nanoarrays and donor Si substrate under wet (water) condition occurs by overcoming the wet adhesion of confined water molecules between Au and Si, where the underneath Ni layer is completely removed. Figure 2.13 shows experimental and finite element analysis (FEA) results of the separation load (L)-separation displacement (D) curves, obtained with an array (1×1 cm^2) of quasi-3D Au (50 nm)/PMMA (1 μm)-based nanoposts under dry (red color, 20% relative humidity) and wet (blue color, distilled water) conditions. The results produce consistent agreements in which the L increases rapidly at the edge within ~1 mm of the specimen and then decreases until it becomes constant to the steady-state (L_{ss}). Notably, a substantial decrease of the L_{ss}, by more than ~70%, occurs under the wet condition as compared with that under the dry condition. These results indicate that the presence of water molecules indeed results in the reduction of interfacial energy at the 3D nanoscale featured surface. The green-filled area in Figure 2.13 defines a defect-free zone where the separated plasmonic nanoarrays remain intact with a successful yield of nearly 100% (among >100 testbed specimens). A representative image of the damaged specimen when peeled the L_{ss} out of the defect-free zone appears in Figure 2.14. The damages may occur due to the increased L_{ss} caused by any potential residues of the sacrificial Ni layer.

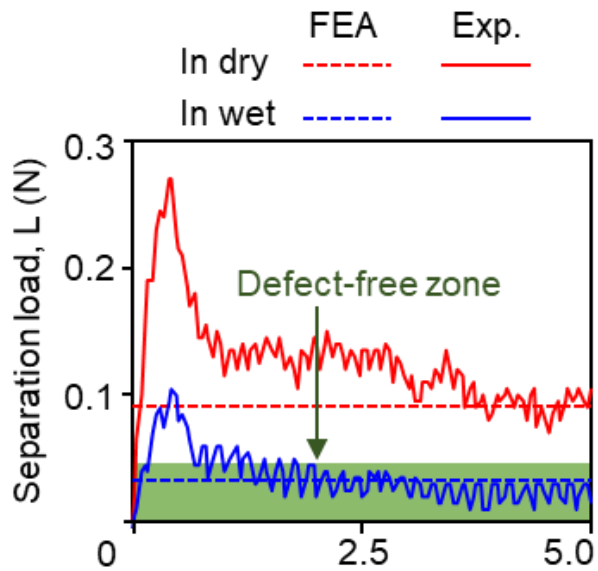

Figure 2.13. Experimental and FEA results of the separation load (L)-separation displacement (D) curves for quasi-3D plasmonic nanoposts under dry (red) and wet (blue) conditions.

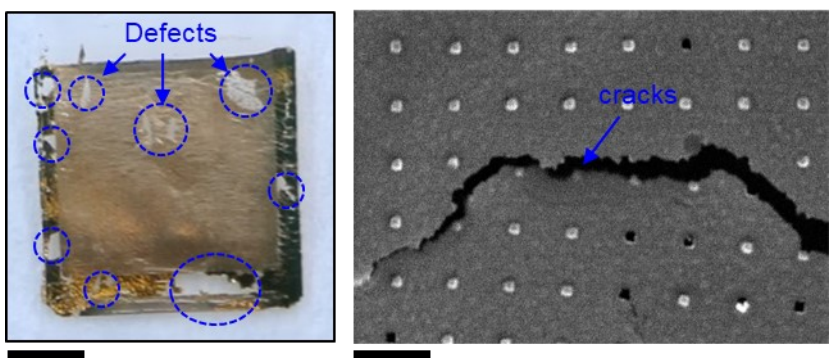

Figure 2.14. Photo (left) and SEM image (right) of the defects and cracks on a specimen when peeled by the L_{ss} out of the defect-free zone. Scale bars are 3.5 mm and 2.3 μm from the left.

Figure 2.15 shows experimental, computational (FEA), and theoretical results that reveal the effect of the nanopost height, H_{post} (inset), on L_{ss}. The results indicate that the steady-state separation load per unit width (L_{ss} /b) of the specimen is increased as the H_{post} is increased from 200 nm to 400 nm, which is attributed to the increased deformation energy required for longer nanoposts. In theory, the energy balance of quasistatic interfacial separation can be expressed as:(Yue Zhang et al., 2017) $W_L = W_{interface} + W_{deformation}$, where W_L (= $L_{ss} \cdot \Delta D$) is the work done by the L_{ss} and ΔD is the separation displacement; $W_{interface}$ (= $G \cdot b \cdot \Delta D$) is the interfacial adhesion energy between the plasmonic nanoarrays and the donor Si substrate, where G is the adhesion

energy per unit area at the interface; $W_{deformation}$ (= $u \cdot b \cdot \Delta D \cdot H_{post}$) is the deformation energy of the quasi-3D nanoposts, where u is the deformation energy density. As a consequence, the energy balance leads to: $L_{ss}/b = G + u \cdot H_{post}$, wherein the G and u are independent of the H_{post} because both the interface and materials properties of the quasi-3D nanoposts remain unchanged. These assessments are consistent with the experimental observations that the L_{ss} under wet condition is substantially smaller than that under dry condition for the same H_{post}, mainly due to the reduced interfacial adhesion energy by the effect of water molecules. The control evaluations by exploiting similar quasi-3D plasmonic nanoarrays with a nanohole configuration (Figure 2.16 & 2.17) produce consistent results to support and confirm these findings.

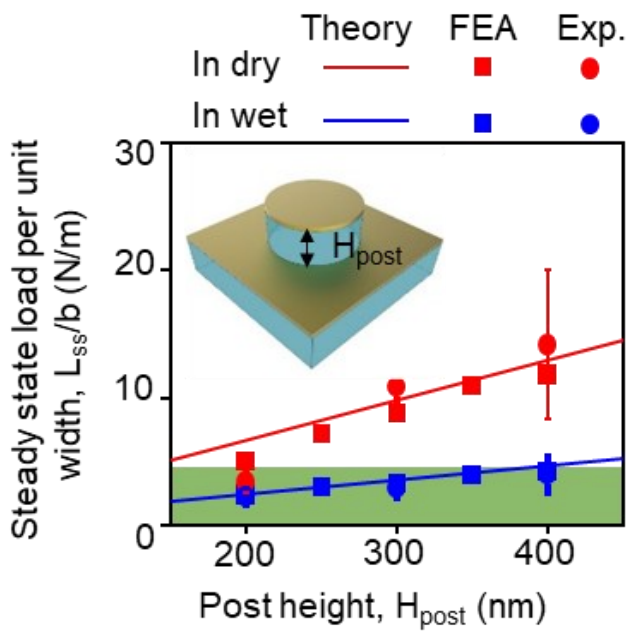

Figure 2.15. Experimental, FEA, and theoretical results for the effect of H_{post} on L_{ss}/b.

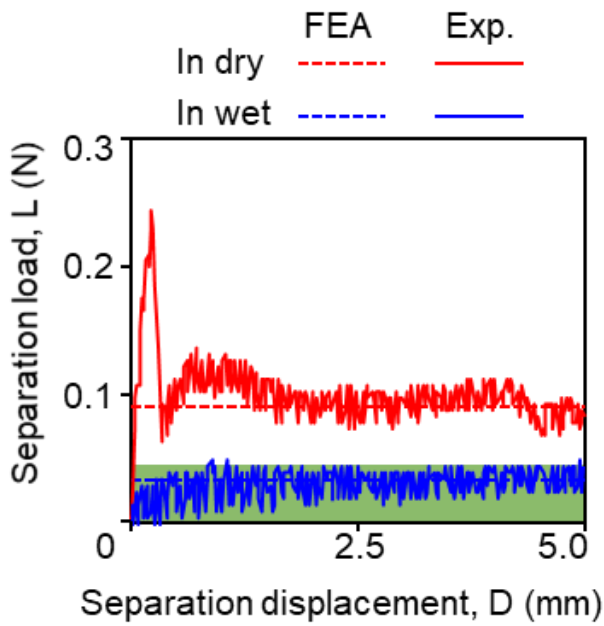

Figure 2.16. Experimental and FEA results of the separation load (L)-displacement (D) curves for quasi-3D plasmonic nanoholes under dry (red) and wet (blue) conditions.

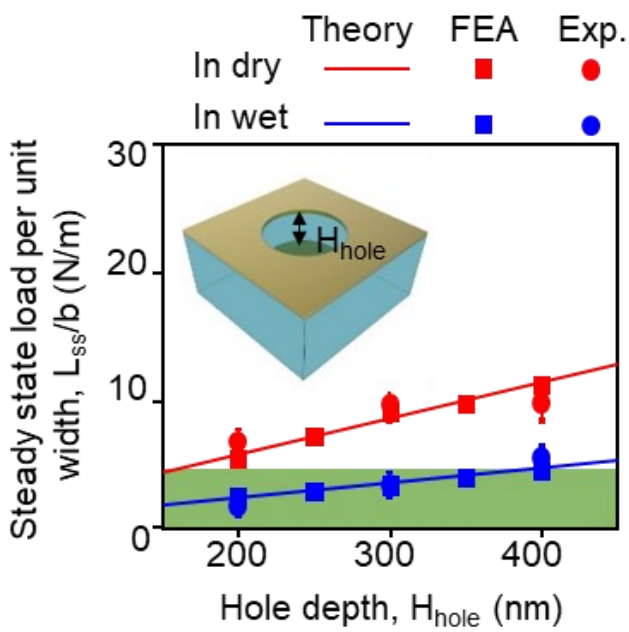

Figure 2.17. Experimental, FEA, and theoretical results for the effect of H_{hole} on L_{ss}/b.

Figure 2.18 provides the corresponding modeling (FEA) results that reveal the underlying strain distributions of the plasmonic nanoarrays during the interfacial separation process under the dry (top row) and wet conditions (bottom row). Here, the modeled structure includes a unit of Au (50 nm)/PMMA (1 μm) composites configured with quasi-3D nanoposts (left column, H_{post} = 300 nm) and nanoholes (right column, H_{hole} = 300 nm), where d is defined as the distance between the separated plasmonic nanoarrays and the donor Si substrate (Figure 2.19). The results reveal that the maximum principal strain (ε_{max}) appears in the PMMA layer where the magnitude in wet conditions is >60% smaller than that in dry conditions. This aspect allows the Au film to experience insignificant mechanical constraints during the interfacial separation process and thereby can reduce the potential risk of defects, which is consistent with the above-mentioned experimental observations. The corresponding modeling results for varied d, $H_{post,}$ and H_{hole} as well as by exploiting different dielectric spacers (BCB and SU8) under both dry and wet conditions are summarized in Figure 2.20-2.23.

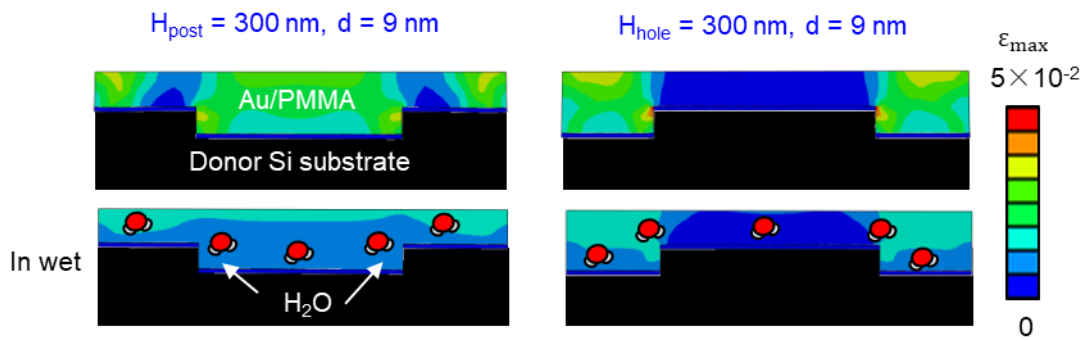

Figure 2.18. FEA results of strain distributions in the nanoarrays during the interfacial separation under dry and wet conditions.

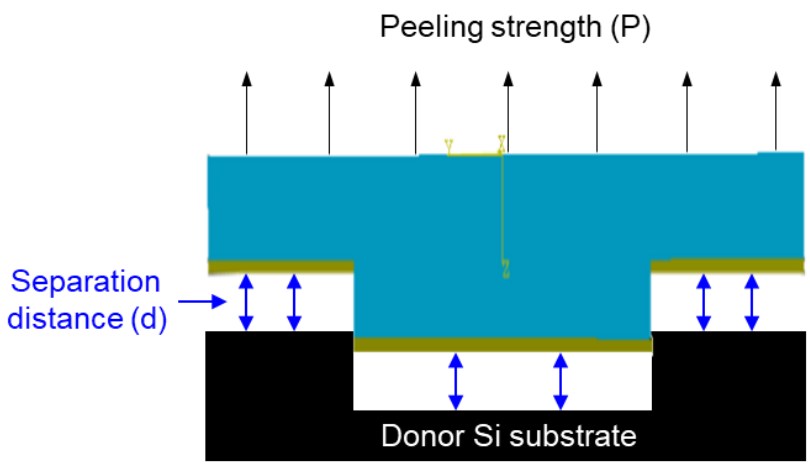

Figure 2.19. Schematic of the modeled structure.

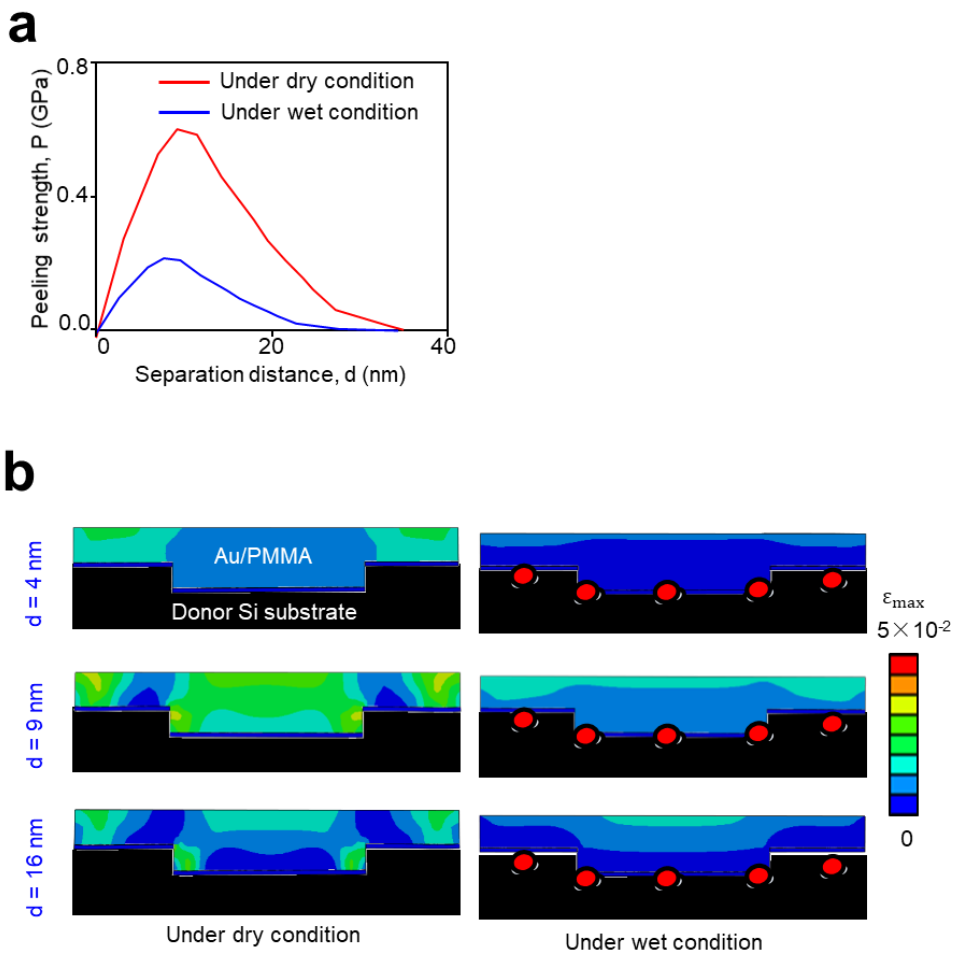

Figure 2.20. (a) FEA results of the peeling strength (*P*)-separation distance (*d*) curves for quasi-3D nanoposts in dry (red) and wet (blue) conditions. (b) FEA results of strain distributions during the interfacial separation for varied *d*.

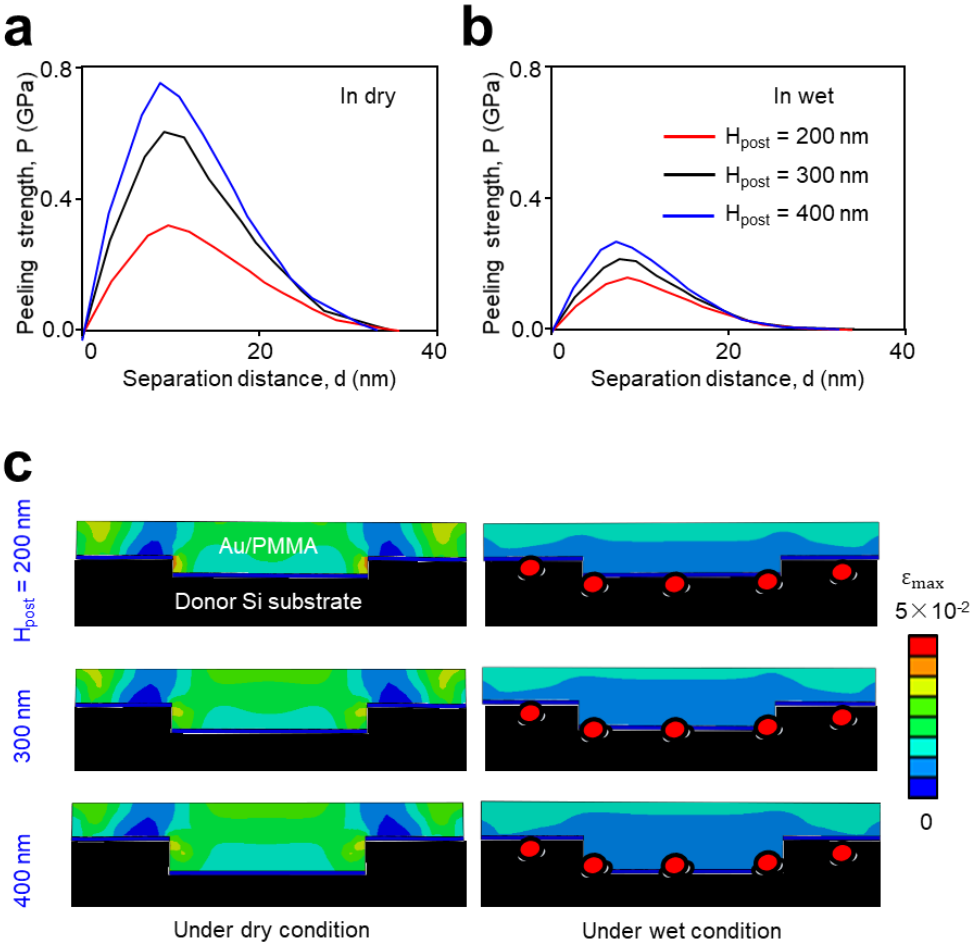

Figure 2.21. FEA results of the peeling strength (*P*)-separation distance (*d*) curves for quasi-3D nanoposts with different Hpost in dry (a) and wet (b) conditions. (c) FEA results of strain distributions during the interfacial separation for varied H_{post}.

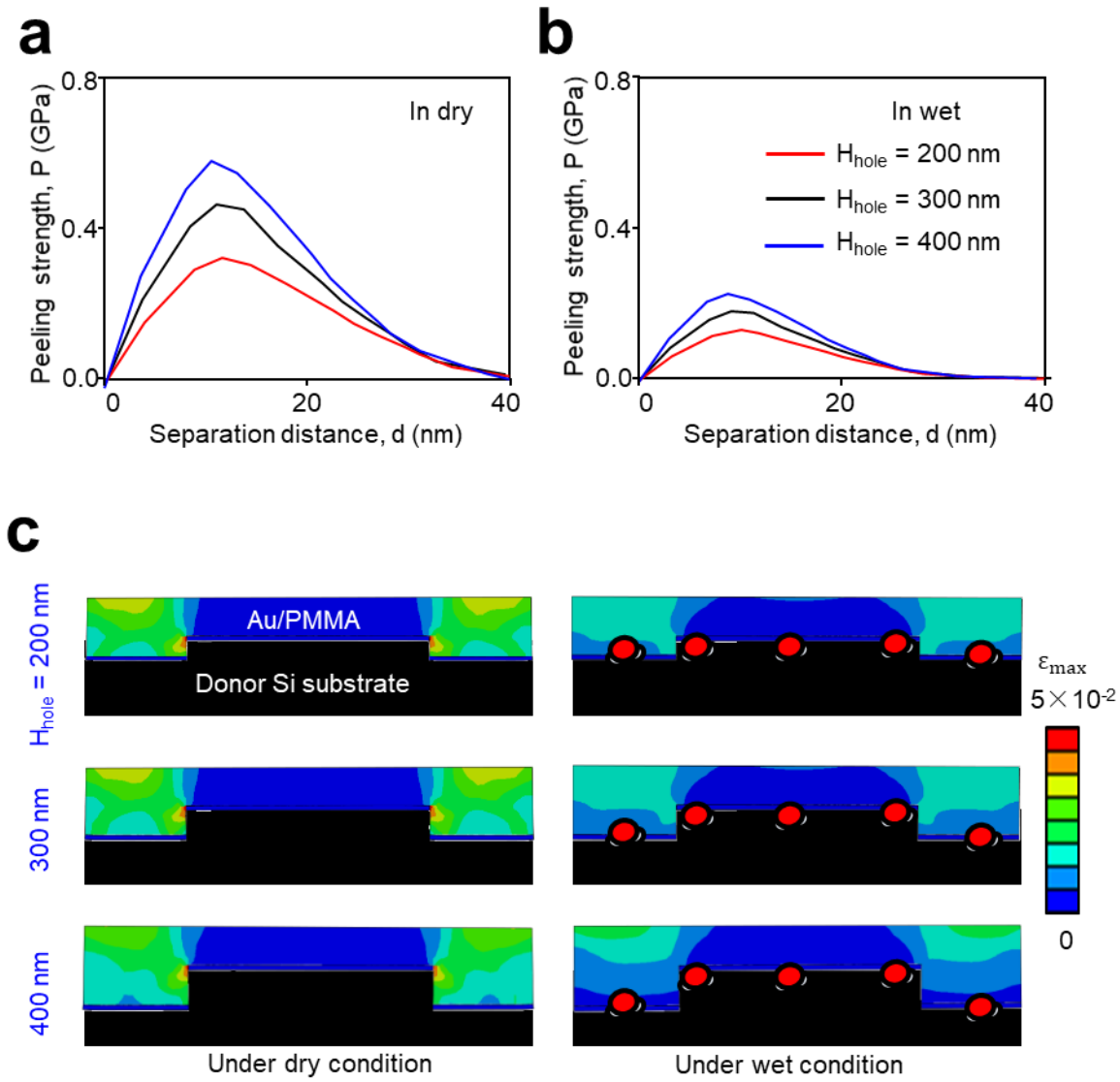

Figure 2.22. FEA results of the peeling strength (*P*)-separation distance (*d*) curves for quasi-3D nanoholes with different H_{hole} in dry (a) and wet (b) conditions. (c) FEA results of strain distributions during the interfacial separation for varied H_{hole}.

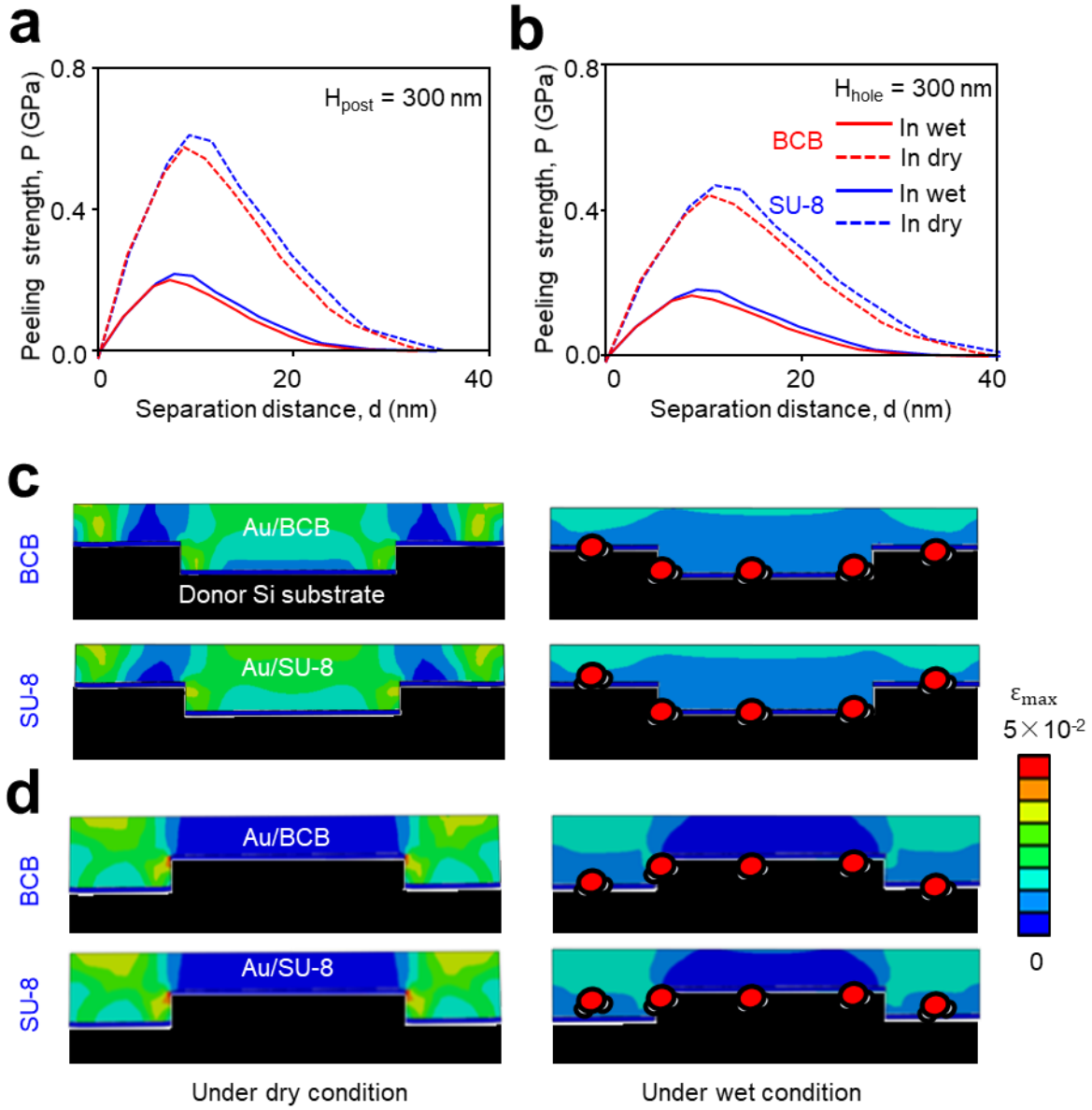

Figure 2.23. (a) FEA results of the peeling strength (*P*)-separation distance (*d*) curves for quasi-3D nanoposts with BCB and SU-8 in dry and wet conditions. (b) FEA results of the peeling strength (*P*)-separation distance (*d*) curves for quasi-3D nanoholes with BCB and SU-8 in dry and wet conditions. (c) and (d) FEA results of strain distributions during the interfacial separation for varied dielectric spacer materials.

2.4 Applicability to diverse types of quasi-3D plasmonic nanoarrays

This 3D nanoassembly method is applicable to diverse types of quasi-3D metal-dielectric composite nanoarrays. Figure 2.24 presents an arrangement of schematic illustrations (left column), SEM images (middle column) and transmission spectra measurements (right column) for a range of quasi-3D plasmonic nanoarrays configured with (a) nanoposts, (b) nanoholes, (c) bilayer nanowire gratings and (d) ring-shaped disks, each of which is transferred from its donor Si substrate to a foreign DSP Si wafer. Detailed geometric information for these plasmonic nanoarrays appears in Figure 2.25, with the minimum width of the nanoarrays ranging from 250 nm to 1.5 μm. The collective set of the SEM images indicates that no visual defects appear along the surface of the transferred nanoarrays regardless of the feature sizes, shapes, and configurations. Also, the continued agreement between the transmission spectra of experimental (blue color) and modeling (red color) results support these observations, each of which is obtained using the Fourier transform infrared (FTIR) spectrometer (Nicolet 5700) and the Computer Simulation Technology (CST) Microwave Studio-based on the finite integration technique (FIT), respectively. Repetitive transmission measurements of the specimens at widely spread locations produce consistent outcomes (Figure 2.26), highlighting the uniformity and integrity over the area (1×1 cm^2).

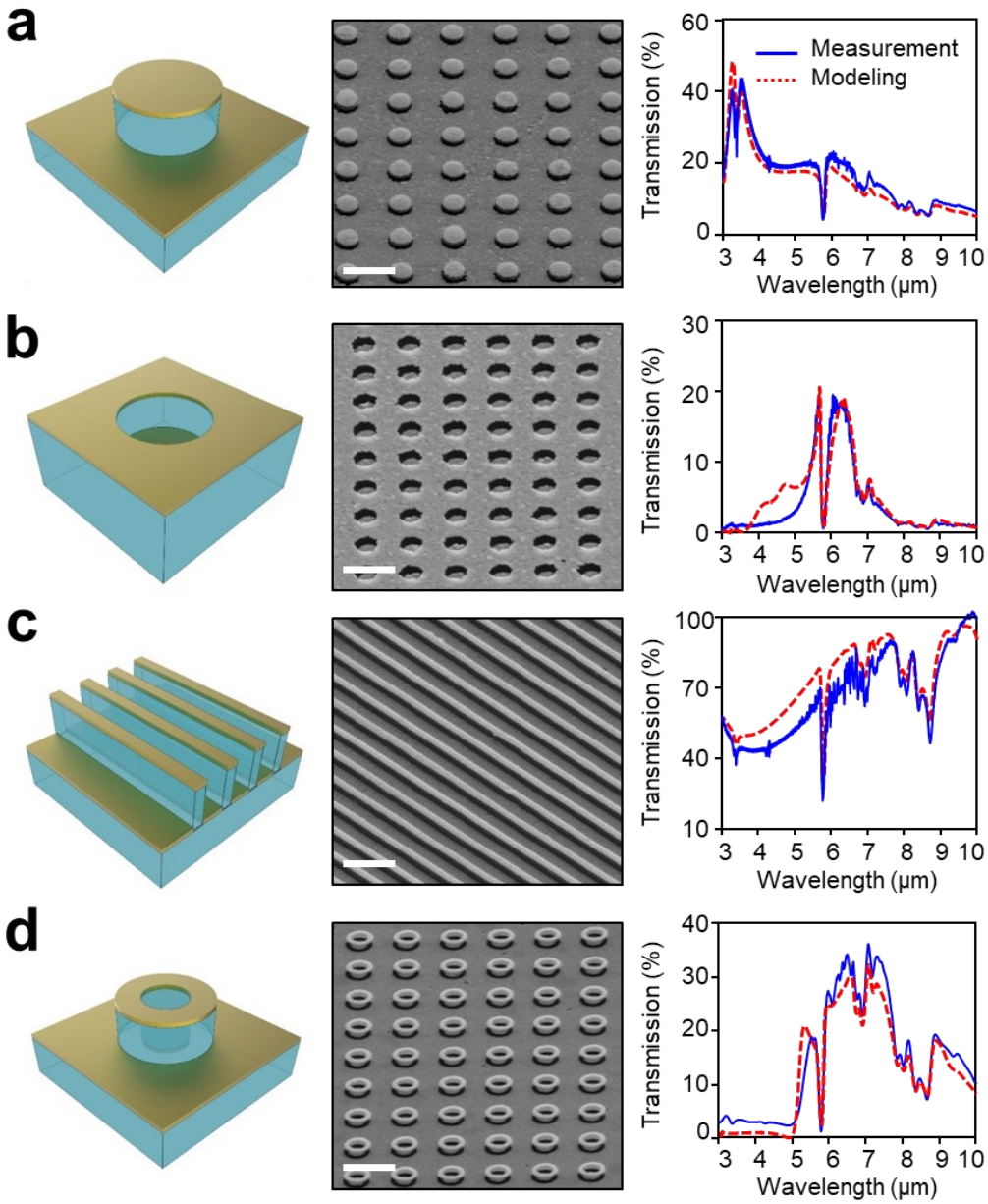

Figure 2.24. Demonstrations on various types of quasi-3D plasmonic nanoarrays. An arrangement of schematic illustrations (left column), SEM images (middle column), and analysis of transmission spectra (right column) for a range of quasi-3D plasmonic nanoarrays configured with (a) nanoposts, (b) nanoholes, (c) bilayer nanowire gratings and (d) ring-shaped disks. Scale bars are 3.3 μm, 2.0 μm, 1.8 μm, and 2.0 μm from the top.

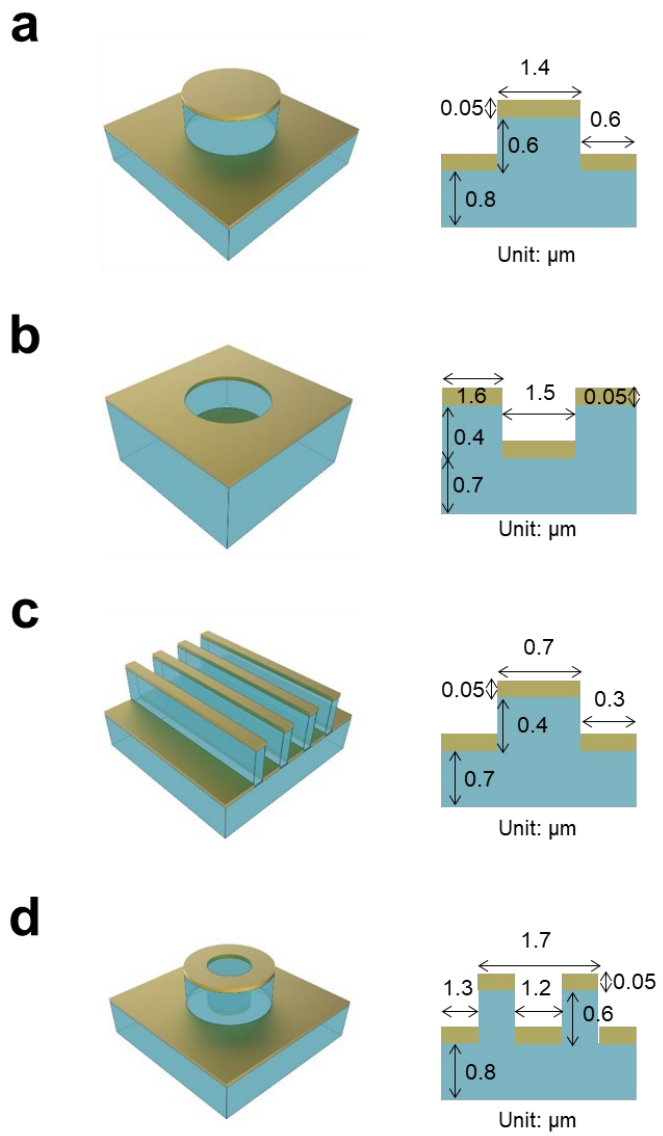

Figure 2.25. Detailed geometric information for the quasi-3D nanoarrays configured with nanoposts (a), nanoholes (b), bilayer nanowire gratings (c), and ring-shaped disks (d).

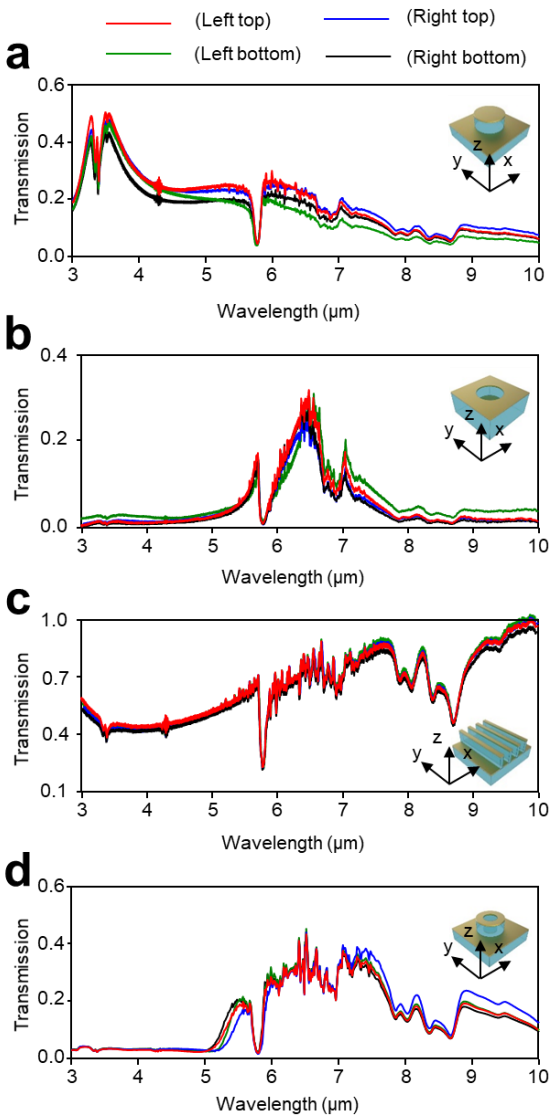

Figure 2.26. Repeatedly measured transmission spectra at widely spread locations of the transferred nanoarrays.

2.5 Heterogeneous modular assembly with controlled spatial arrangement

The ability to assemble several identical or different types of quasi-3D plasmonic nanoarrays in a spatially controlled manner provides a mean of attaining advanced light manipulation.(Goldflam et al., 2017; X. Liu et al., 2011; J. Valentine et al., 2008; Shuang Zhang et al., 2005; Shuang Zhang et al., 2006; Zhao, Belkin, & Alu, 2012) Figure 2.27 shows a schematic illustration (left) and a photo (right) of multiple stacked plasmonic films configured with identical quasi-3D nanoposts in which each unit is sequentially transferred from its donor Si substrate to a single DSP wafer loaded on a temporary handling holder. The adhesion at the interface between each transferred plasmonic film can be secured by post-annealing treatment in a convention oven at 60°C for 10 min. Here, the transferred nanoposts exhibit the diameter (D_{post}) of 1.0 μm and the edge-to-edge gap (G_{edge}) of 800 nm (inset schematic). The enlarged SEM images of the 1st (left top), 2nd (right top), 3rd (right bottom) and 4th (left bottom) layer-stacked nanoposts (Figure 2.28) and the corresponding results of transmission spectra measurements (Figure 2.29) consistently indicate that no defect occurs throughout the multiple stacking process. The relative alignment error of each stacked layer remains below 1 μm, which can be furthermore improved by employing alignment marks. Figure 2.30 presents another experimental demonstration that involves multiple modular assemblies to construct a larger array of dissimilar quasi-3D plasmonic nanoposts that exhibit different sizes (D_{post} = 0.7 μm-1.7 μm) and arrangements (G_{edge} = 0.7 μm-1.9 μm). The enlarged SEM images of each transferred module (Figure 2.31) and the corresponding results of transmission spectra measurements (Figure 2.32) provide continued consistency. These demonstrations highlight the spatial controllability and modular scalability of this method, which is highly desired for many envisioned large-scale plasmonic applications.

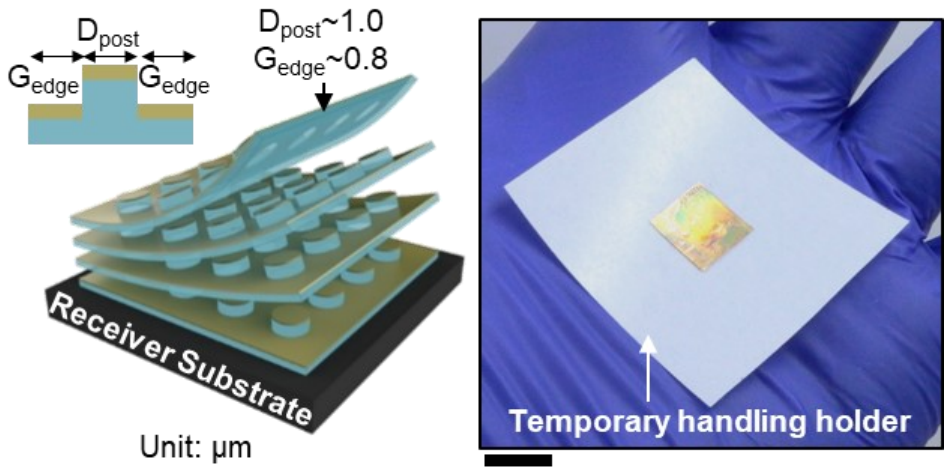

Figure 2.27. Schematic illustration (left) and photo (right) of multiple stacked plasmonic nanoarrays configured with identical quasi-3D nanoposts. Scale bar is 1 cm.

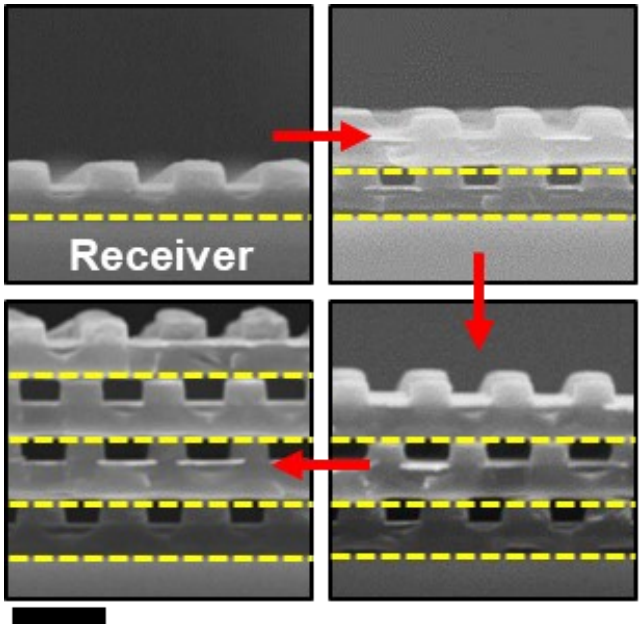

Figure 2.28. The enlarged SEM images of the 1st, 2nd, 3rd, and 4th layer-stacked nanoposts. Scale bar is 2.3 μm.

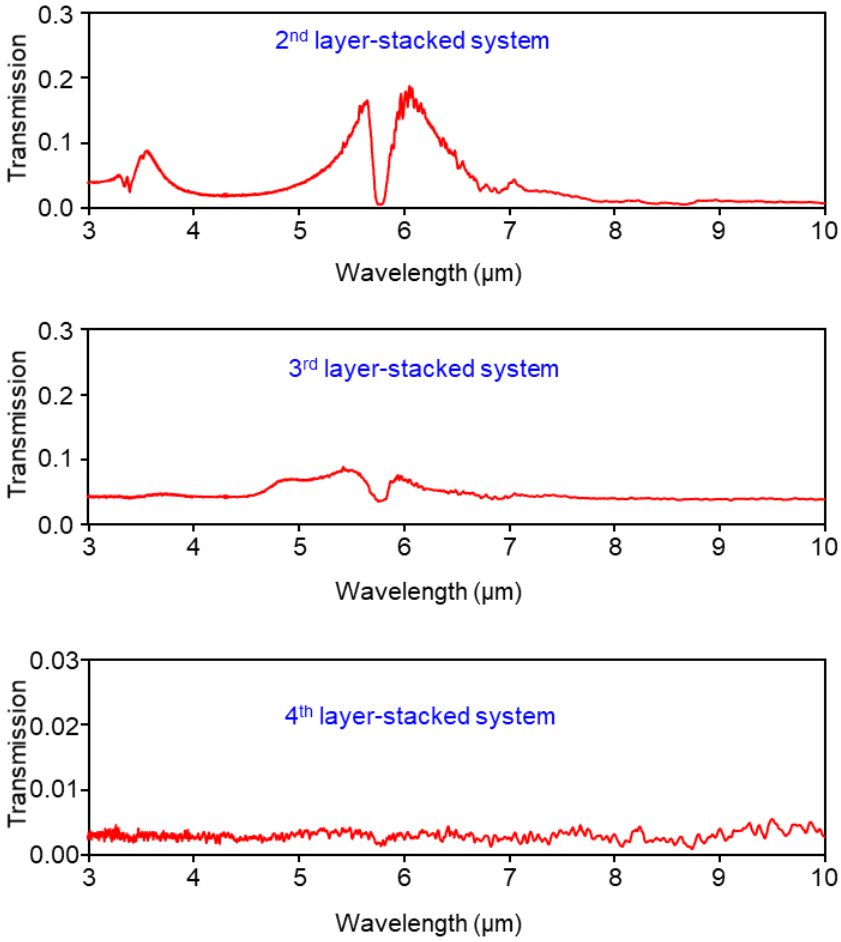

Figure 2.29. Measured transmission spectra of the 2nd, 3rd, and 4th layer-stacked nanoposts.

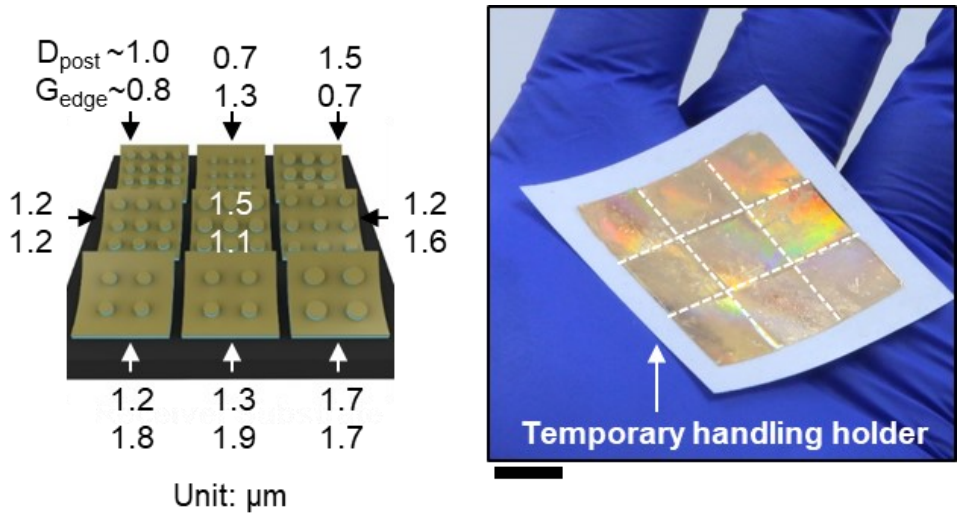

Figure 2.30. Schematic illustration (left) and photo (right) of a 3×3 array of dissimilar quasi-3D plasmonic nanoposts featured with different sizes and arrangements. Scale bar is 1 cm.

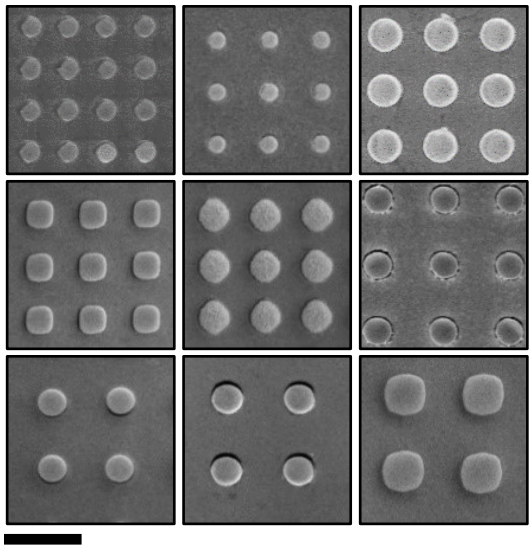

Figure 2.31. The enlarged SEM images of each transferred module. Scale bar is 3.3 μm.

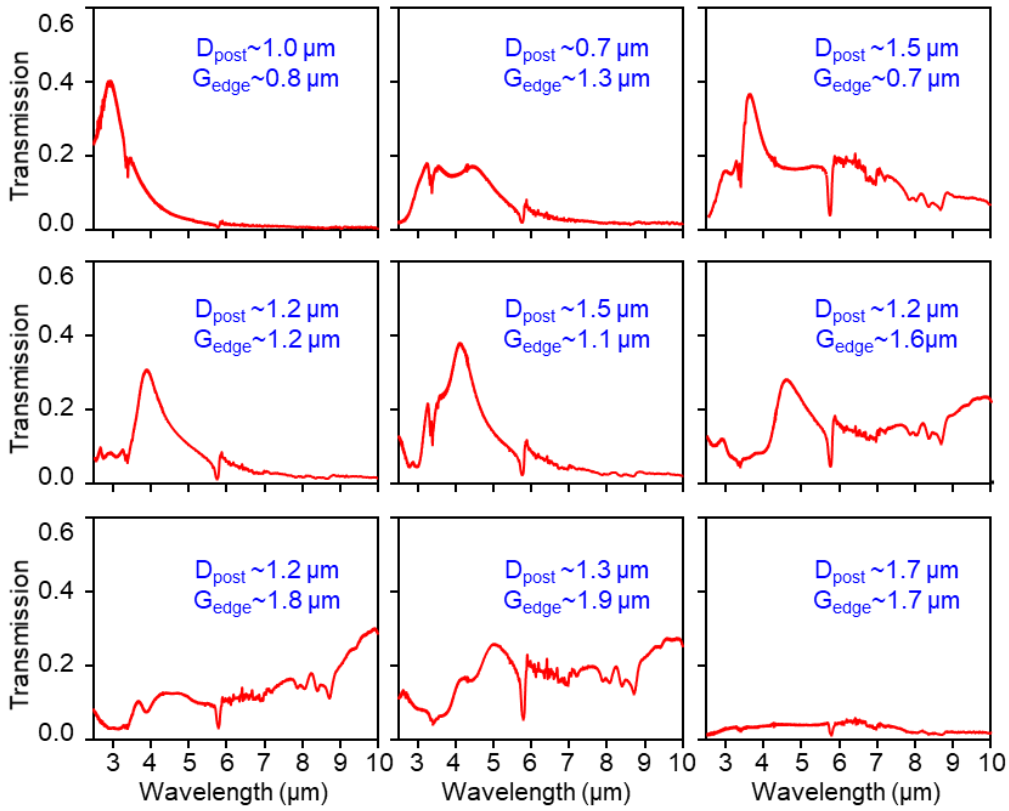

Figure 2.32. Measured transmission spectra of the transferred each module unit.

2.6 Pilot assembly and post-electro-optical (EO) analysis

The pilot assembly of quasi-3D plasmonic nanoarrays with a sophisticatedly designed HPD illustrates the feasibility and utility of this method in the deterministic manipulation of the light spectrum for enhancing the detection performances and functionalities beyond its standards.(Chang et al., 2010; Ku et al., 2013; S. J. Lee et al., 2011; Q. Li et al., 2014; Rosenberg, Shenoi, Vandervelde, Krishna, & Painter, 2009) Figure 2.33 presents a photo (left) and a schematic illustration (right) of the demonstration system. Here, an MWIR-T2SL-based HPD serves as a model receiver system, of which the basic components include GaSb (p-type) for top contact (300 nm), InAs/GaSb/InSb for active (×300 periods, 1.9 μm)/bottom (×80 periods, 508 nm) superlattice and Indium (In) bumps for connections, all assembled in a flip-chip-on-laminate configuration (Figure 2.34). (S. J. Lee et al., 2011) The constituent materials and structures of this model receiver system represent a chemically and mechanically vulnerable receiver substrate that is otherwise difficult to directly construct quasi-3D plasmonic nanoarrays by using conventional nanolithography or micro/nanoscale printing techniques. The process begins by mounting the HPD on a leadless chip carrier (LCC) to serve as a temporary handling holder that allows the HPD to avoid any physical contact during the entire process. The resulting structure is then immersed underneath distilled water in a petri dish while a unit (1×1 cm^2) of quasi-3D Au (50 nm)/PMMA (800 nm) nanoposts (H_{post} = 0.2 μm, D_{post} = 1 μm, G_{edge} = 1 μm) stays afloat on the water surface. The subsequent assembly step takes place on the probe station with full XY movements and 360° rotation under microscope examinations. Drying of the assembled unit at room temperature finishes the process. A representative microscope image of the complete system (Figure 2.35) suggests that the receiver HPD is in its integrity with no visible defects or damages along the surface. The enlarged SEM images taken from widely spread locations on the surface of the transferred nanoposts support these observations (Figure 2.36).

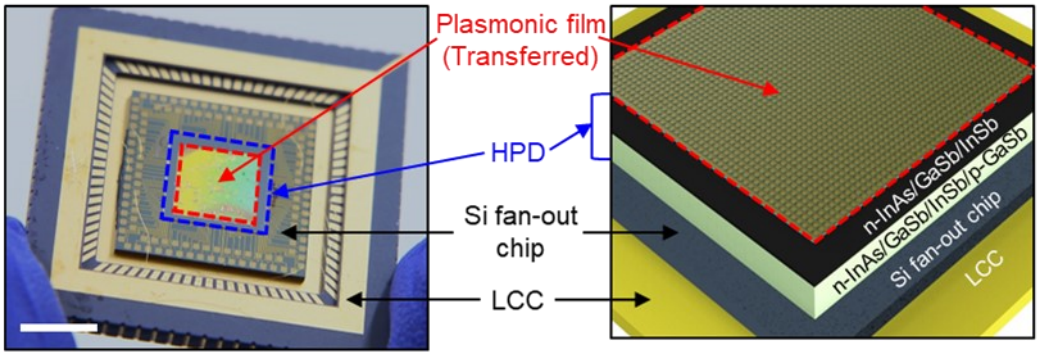

Figure 2.33. Photo (left) and schematic illustration (right) of a demonstration system. Scale bar is 4.5 mm.

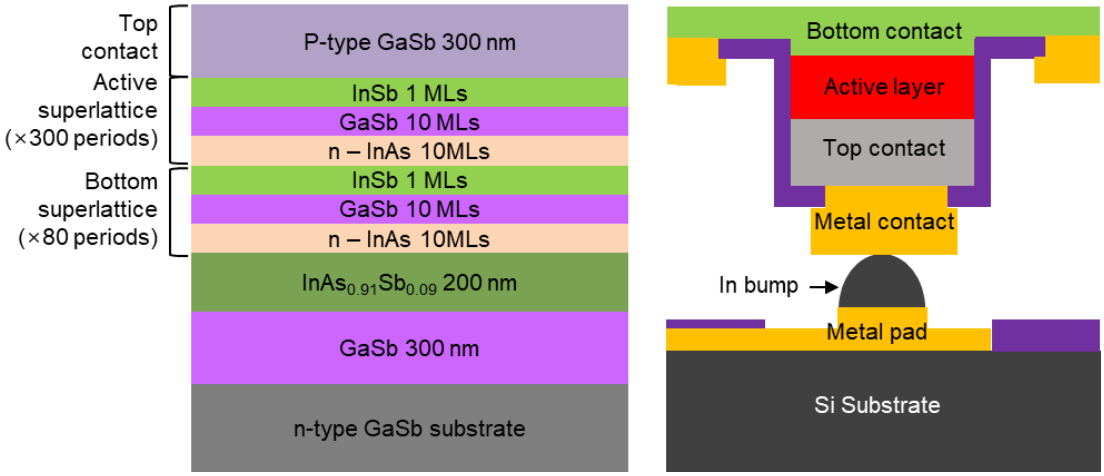

Figure 2.34. Schematics of the model MWIR-T2SL-based HPD assembled in a flip-chip-on-laminate configuration.

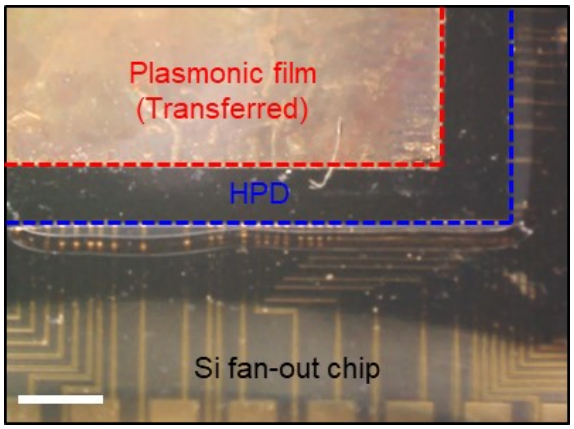

Figure 2.35. EO-measured spectral HPD-responses and FTIR-measured transmission of the specimens.

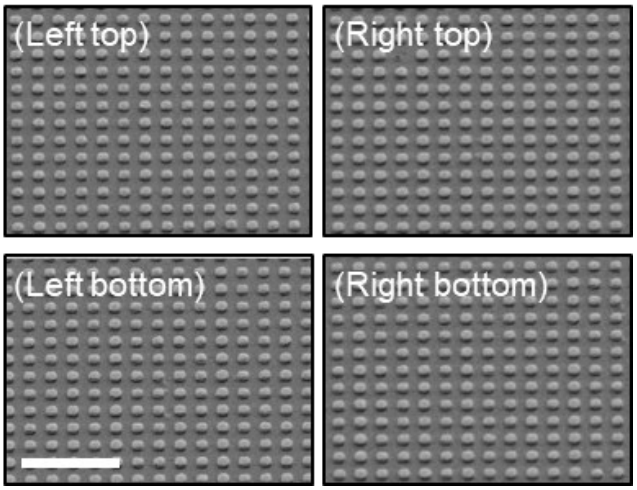

Figure 2.36. EO-measured spectral HPD-responses and FTIR-measured transmission of the specimens.

The post-electro-optical (EO) analysis takes place in a custom measurement setup that allows for the acquisition of optical-to-electrical-measured spectral responses at 77K (Figure 2.37). Figure 2.38 presents representative measurement results obtained with the following specimens; (a) the as-fabricated HPD (red color), (b) the HPD after assembly of the nanoposts (blue color), and (c) the HPD after removal of the nanoposts (purple color) by acetone to dissolve the underneath PMMA layer and thereby strip the entire Au plasmon film (Figure 2.39). The inset graph (green color) shows the corresponding FTIR-measured transmission after the assembly process. The results indicate that deterministic adjustment of the waveguide resonance occurs in the HPD after the assembly (blue color) in which distinct oscillatory characteristics appear in all of the spectral responses due to the Fabry-Perot cavity resonances between air and the embedded mirror planes consisting of ohmic contact under bump metallization and In bump. (E. K.-w. Huang et al., 2011; E. K.-w. Huang et al., 2012; J. A. Montoya, Z. B. Tian, S. Krishna, & W. J. Padilla, 2017) The transmitted light through the narrow gaps of the nanoposts exhibits waveguide resonance behavior that is correlated to interactions between the embedded Au plasmonic layers where the maximum value of the electric field magnitude ($|E|$) occurs at the peak wavelength.(Wenjun Fan, Zhang, Malloy, & Brueck, 2005; W. Fan, Zhang, Minhas, Malloy, & Brueck, 2005) The corresponding FIT-simulated $|E|$ distribution at the peak wavelength appears in Figure 2.40. Importantly, the spectral responses after removal of the nanoposts remain barely changed from those of the as-fabricated HPD within the range of measurement error, providing clear evidence of retaining intact even after the assembly and removal of the nanoposts. Figure 2.41 provides quantitatively comparable results of dark- and photo-currents between the as-fabricated HPD (symbols) and after the removal of the nanoposts (lines) at the applied bias voltage ranging from -500 mV to 0 V, all obtained using a custom measurement setup at 77K (Figure 2.42). The results show that the dark- and photo-currents undergo negligible changes within the range of measurement error, which consistently implies that the intrinsic performances of the receiver HPD remain preserved without any degradation in the performance.

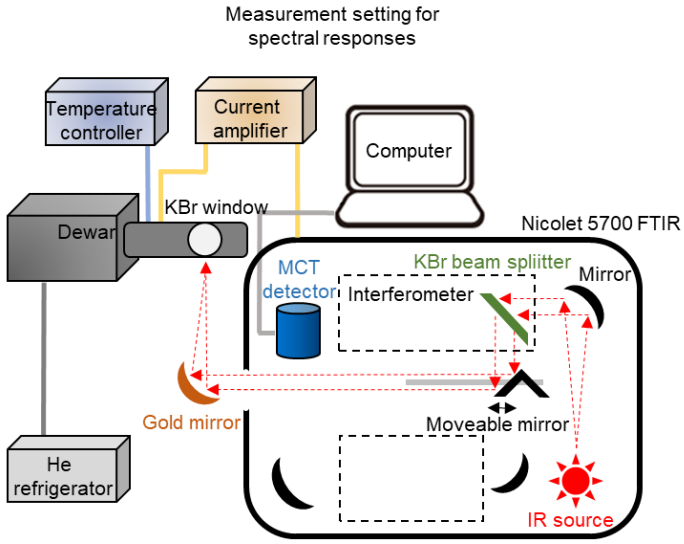

Figure 2.37. Schematic diagram of a custom setup for the measurement of optical-to-electrical (EO)-measured spectral response.

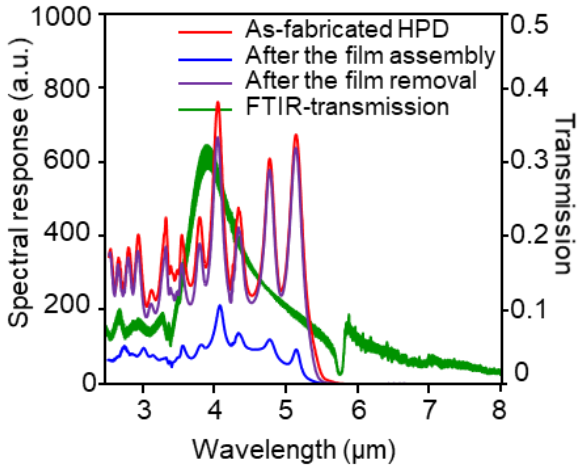

Figure 2.38. EO-measured spectral HPD-responses and FTIR-measured transmission of the specimens.

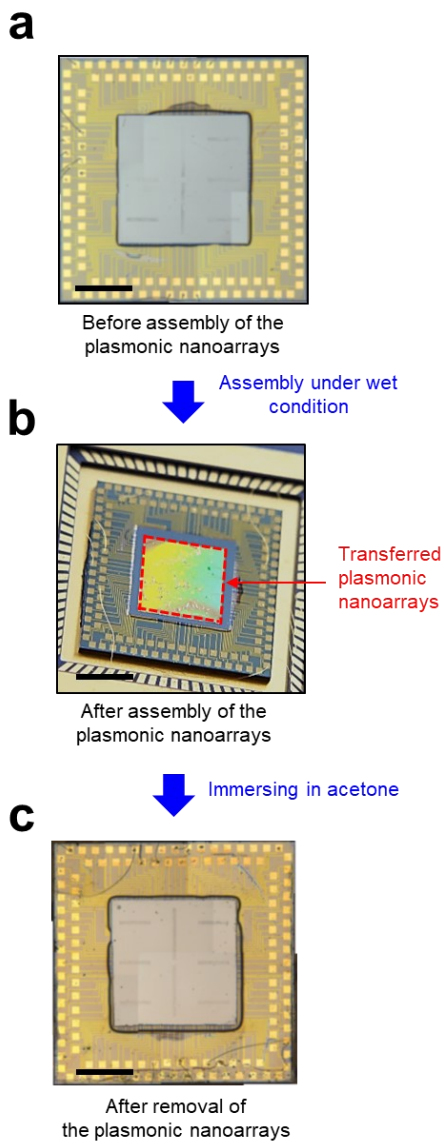

Figure 2.39. Photos of the as-fabricated HPD (a), the HPD after the assembly of the nanoposts (b), and the HPD after the removal of the nanoposts (c). Scale bars are 3.5 mm, 4.5 mm, and 3.5 mm from the top.

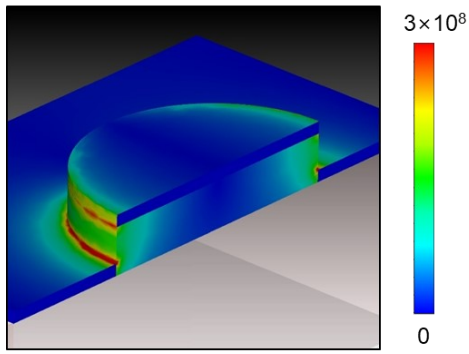

Figure 2.40. FIT-simulated distribution of electric field magnitude (|E|) at the peak wavelength for a nanopost unit cell.

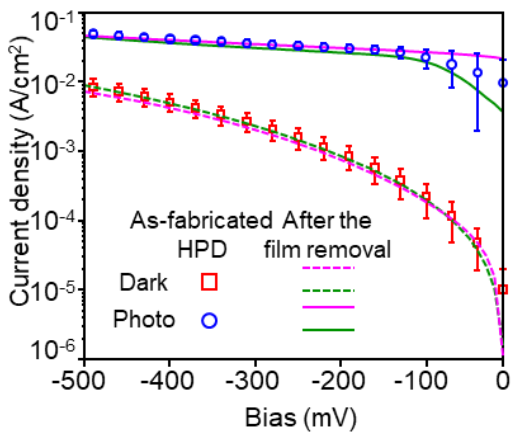

Figure 2.41. Measured dark- and photo-currents of the specimens.

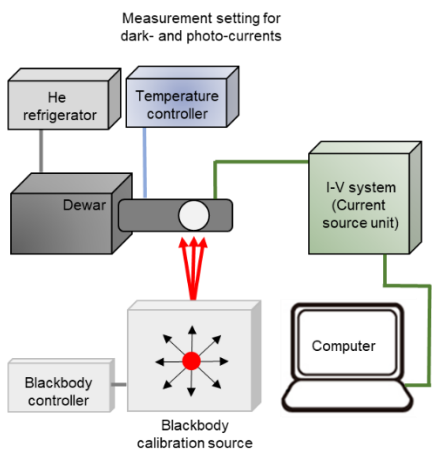

Figure 2.42. Schematic diagram of a custom setup for the measurement of dark- and photo-current.

2.7 Methods

2.7.1 Fabrication of donor Si substrates

Conventional EBL technique was used to produce various periodic nanopatterns of a photoresist layer on a Si substrate. A thin layer (20 nm) of Cr formed by e-beam evaporator was used to serve as a selective masking layer for subsequent etching of Si. A brief isotropic etching with CF_4/O_2 (13/2 sccm; 45 mTorr; 100W) for 10 min was followed to slightly taper the sidewall of the Si patterns, by ~80° from the ground (Figure 2.43), to serve a passage for solutions (water or etching solutions) to efficiently pass through the dielectric spacer. Finally, the Cr masking layer was removed by immersing in a bath of a Cr etchant for ~30 sec to complete the entire process.

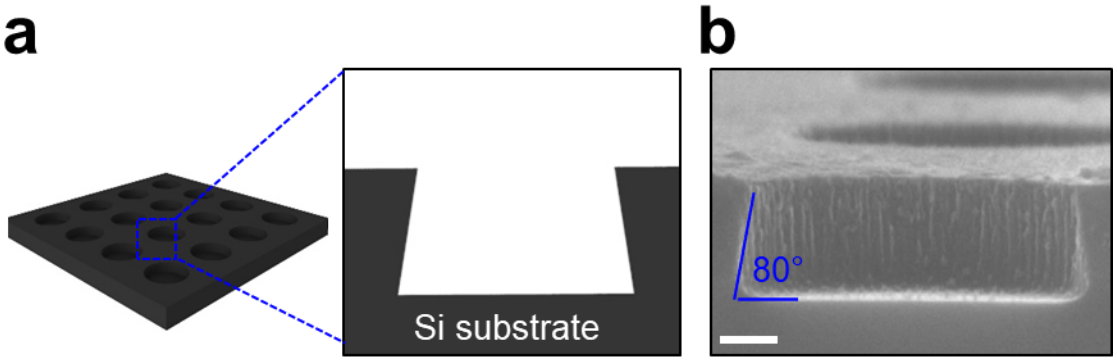

Figure 2.43. (a) Schematic illustration of the nanohole patterns tapered by ~80° from the ground. (b) Cross-sectional SEM image of the tapered nanohole pattern. Scale bar is 160 nm.

2.7.2 Computational analysis

The FEA was performed by using the ABAQUS/standard package. The material deformation of the PMMA was modeled by viscoelastic-plastic behavior with the mechanical modulus (E) and the Poisson's ratio (ν) E = 3.0 GPa and ν = 0.35, and yield stress σ_y = 40 MPa. The plasmon Au film was modeled by elastic-perfectly plastic behavior, with E = 79 GPa, ν = 0.42, and yield stress σ_y = 200 MPa. The donor Si substrate was modeled by linear elastic model with E = 130 GPa and ν = 0.27. A mesh convergence study was conducted in advance to confirm the discretization of the model sufficiently enough for extracting converged separation force. The interfacial separation between the plasmon Au film and the donor Si substrate was modeled using

the cohesive zone model with a bilinear traction–separation relation. In the cohesive zone model, the interfacial traction-separation relation was characterized by the following two key parameters: (1) cohesive strength (σ_0, the maximum traction in the traction-separation curve), and (2) fracture toughness (Γ_c, the area of the traction–separation curve). In this study, the cohesive strength of $\sigma_0 = 31$ MPa and 13 MPa and the fracture toughness of $\Gamma_c = 0.48$ J/m^2 and 0.19 J/m^2 were used for the dry and wet conditions, respectively. A constant displacement loading rate was applied on the top to delaminate quasi-3D plasmonic nanoarrays while the donor Si substrate was fixed.

2.7.3 Numerical simulation of transmission

Numerical simulation was conducted by using the Computer Simulation Technology (CST) Microwave Studio-based on a finite integration technique (FIT) to design various quasi-3D plasmonic nanoarrays and to understand their underlying mechanisms such as localized surface plasmon (SP), propagating SP, waveguide resonance mode and the Fabry-Perot resonance. In the CST simulator, a single unit cell was simulated with appropriate boundary conditions including the transverse magnetic field equal to zero (perfect magnetic conductor: PMC), the transverse electric field equal to zero (perfect electric conductor: PEC), a TEM plane wave was simulated to propagate in the z-direction. The direction of polarized incoming light was parallel to the x-axis, as also illustrated in Figure 2.25. The refractive index of PMMA and the permittivity of Au used in these simulations were measured by spectroscopic ellipsometry (Figure 2.44). The wavelength-independent refractive index of the DSP Si wafer, $n_{Si} = 3.4$, was used.

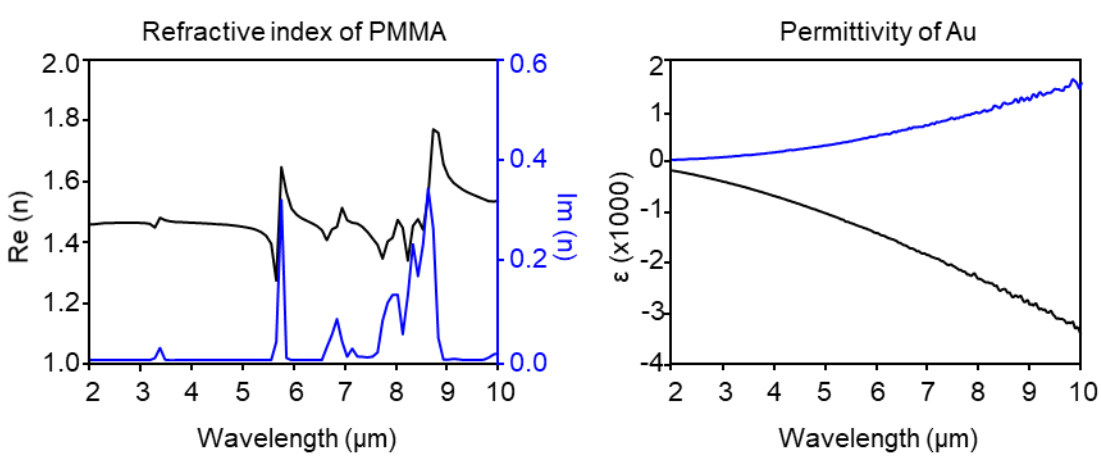

Figure 2.44. Measured complex refractive index of PMMA (left) and Au (right) permittivity.

2.7.4 FTIR measurements

The transmission spectra were recorded by the Nicolet 5700 Fourier transform infrared (FTIR) spectrometer with a liquid nitrogen-cooled mercury-cadmium-telluride detector and KBr beam splitter in the wavelength range of 3-10 μm.

2.7.5 Fabrication of MWIR-T2SL-based HPD

For the fabrication of the MWIR-T2SL, InAs/GaSb type-II superlattice (SL) device structure was grown on a 2-inch n-type GaSb substrate with a solid source molecular beam epitaxy (MBE) machine. A 300 nm GaSb buffer layer was grown to smooth the surface before the device layer growth. A 200 nm InAsSb etch stop layer was grown, followed by n-type bottom contact SL-layer (×80 periods) and absorber SL-layer (×300 periods) consisting of 10 monolayer (ML) of InAs / 10 ML of GaSb / 1 ML of InSb, and a 300 nm p-type GaSb top contact layer. The fabrication scheme of the HPD was composed of a dry etch to form the mesa, surface passivation, ohmic metal evaporation, under bump metallization, In deposition and reflow process. An array mesa was formed using standard photolithography, inductively coupled plasma (ICP) etching by BCl3 gas, followed by wet-chemical etching in the mixed solution of H_3PO_4:H_2O_2:H_2O = 1:2:20 in order to reduce the charge density on ICP-etched mesa sidewall surfaces (surface leakage). A 200 nm thick SiO_2 was deposited for surface passivation using plasma-enhanced chemical vapor deposition (PECVD). After making a through the SiO_2, the ohmic contact metals, under bump metallization and In bump were deposited by e-beam evaporation, then the deposited In was reflowed to form In bums. The fabricated pixel array device was hybridized with a Si fan-out chip through a standard flip-chip-on-laminate process, then underfill epoxy was injected for mechanical support between the pixel array device and the Si fan-out chip. Finally, the substrate was removed by using a series of chemical-mechanical polishing (CMP) and selective etching to InAsSb etch stop layer. A schematic illustration of the entire fabrication procedure appears in Figure 2.45.

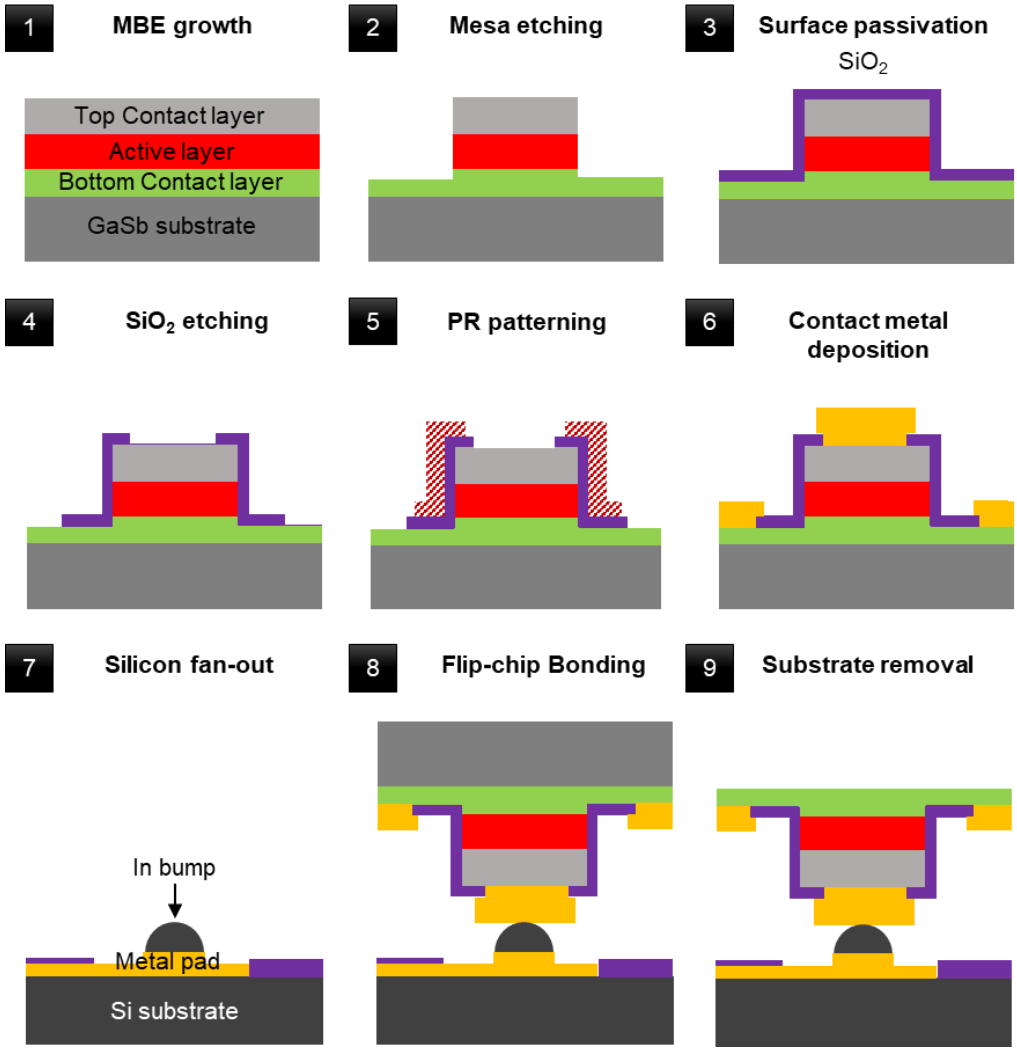

Figure 2.45. Schematic illustration of the entire process for the fabrication of the HPD.

2.7.6 Characterization of MWIR-T2SL-based HPD

The MWIR-T2SL-based HPD was mounted and wire-bonded to a leadless chip (LCC). The HPD was then characterized using custom settings configured for spectral response and dark- and photo-currents. The dark current was measured in a variable temperature cryostat with a cold shield in front of the device and a cold finger cooling the device from the backside, and the photocurrent was tested using a calibrated blackbody source (900K). The FTIR-spectrometer (Nicolet 5700) was used to spectrally evaluate the device-response over the relevant range of operating temperatures and bias voltages.

2.7.7 Transmission spectra analysis

Both arrays of the quasi-3D nanoposts and nanoholes were conceptually considered as two separate plasmonic layers of metallic disk array (MDA) and metallic hole array (MHA) on top of the PMMA spacer. The waveguide (WG) resonance mode through the nanoscale gaps in the nanoposts and nanoholes arrays was ascribed to the interaction between MDA and MHA layers, resulting in greatly enhancing the transmission (EOT, extraordinary optical transmission) and realizing an easy-to-control optical filter. These arrays were designed for potential candidates of sensing techniques, termed algorithmic spectrometry wherein suitable spectral shapes of the sensor's responsivities would be achieved through the deterministic integration of nanoarrays with preexisting EO-sensors for the synthesis of a desired spectral filter shapes. The bilayer metallic nanowire gratings were designed for the polarization of light by transmitting only a specific polarization state (p-polarized, perpendicular polarization to the nanowires), providing advantages of lowering the s-polarized (parallel polarization to the nanowires) transmission by using two self-aligned metal gratings, as compared with the traditional one-dimensional metallic grating (planar grating layer), and increasing the p-polarized transmission due to the Fabry-Perot cavity resonance in the dielectric spacer. The extinction ratio of the bilayer nanowire gratings was ~15 dB at 7.55 μm with a high p-polarized transmission, 89%, as also seen in Figure 2.23 (distinct dips at ~3.4 μm, ~5.8 μm, ~7 μm and 8~9 μm which were attributed to the PMMA absorptions; more specifically to the C-H bond stretching vibrations, the presence of the acrylate carboxyl group, the bending vibration of the C-H bonds, and C-O-C stretching vibration, respectively). Lastly, the ring-shaped disks were designed to isolate a wide spectral band and exhibit a high peak transmission in the passband.

2.8 Conclusion

The results outlined herein illustrate a novel 3D nanoassembly method that occurs under wet condition, enabling intact integration of various quasi-3D plasmonic nanoarrays with a desired foreign substrate. Uniquely, the entire process of this method requires no chemical and thermal treatments (except water at room temperature) and physical contact forces (except weak van der Waals contact force), and thereby leads to a large extension of the types of receiver substrate to nearly arbitrary materials and structures. This method is reliable and repeatable to generate various

types of quasi-3D plasmonic nanoarrays on preferred receiver substrates in a defect-free manner that allows the donor substrates to be recycled multiple times. The comprehensive set of data gained from both experimental, computational and theoretical studies provides an insight into fundamental principles and design tradeoffs to identify optimal conditions for defect-free outcomes. The advanced features of multiple modular assemblies in lateral and vertical configurations, taken together with the implementation of a set of automated equipment for precisely controlled assembly protocols, suggest the controllability and modular scalability of this method. The constituent quasi-3D composite materials and structures presented in this report are not the only options that can be achieved by this method, and broader considerations of even more complex or further downscaled 3D nanoarchitectures(S. Xu et al., 2015; Yan et al., 2016; Yihui Zhang et al., 2017) and nanoelectronics(Fu et al., 2018; Wie et al., 2018; Z. Yan et al., 2017) suggest directions for future research.

3. MECHANICS-DRIVEN MANUFACTURING OF QUASI-THREE-DIMENSIONAL INFRARED BANDPASS FILTERS

A version of this chapter is pending publication in ACS Applied Materials & Interfaces.

3.1 Background

Bandpass filters that allow through a specific band of light frequencies serve as a critical optical element of multispectral imaging for broad applications including space-based imaging, remote sensing, military target tracking, land mine detection, diagnostic medicine, and environmental monitoring.(Amenabar et al., 2017; Duempelmann, Gallinet, & Novotny, 2017; Meng, Cadusch, & Crozier, 2021; Primpke, Godejohann, & Gerdts, 2020; Yakovliev et al., 2019) The bandpass filters are comprised of coupled half-wavelength resonators and multilayer mirrors using alternating dielectric thin films with high and low refractive indices to form a Fabry-Perot optical cavity.(Shaoda Zhang et al., 2019) Effective bandpass filtering occurs through the constructive interference of light when a phase difference coincides with incoming and reflected light waves.(Emadi, Wu, de Graaf, & Wolffenbuttel, 2012) Narrow bandpass filtering with tunable spectral selectivity occurs using hybrid metal-dielectric plasmonic nanoarchitectures (i.e., nanoantennas) with various structural configurations such as metal disks, metal holes, metal coaxial apertures, split-ring resonators, coherent perfect absorbers, and quasi-three-dimensional (quasi-3D) crystals.(Azad, Hara, Singh, Chen, & Taylor, 2013; Jeon et al., 2016; Lin et al., 2019; Shah et al., 2018; Tan et al., 2020; Vial et al., 2014; Yoo et al., 2019) These plasmonic nanoantennas enable a surface-plasmon-enhanced light transmission through a subwavelength aperture (i.e., extraordinary optical transmission).(Fernández-Domínguez, García-Vidal, & Martín-Moreno, 2017)

Traditionally, the fabrication of these nanoarchitectures has been primarily relied on the use of conventional nanolithography techniques by exploiting either electron-beam, focused ion-beam, nanoimprint, or interference lithography on a rigid, flat wafer.(Gao et al., 2014; Joshi-Imre & Bauerdick, 2014; Vieu et al., 2000; Xia et al., 2011) Despite great successes over the past decades, these approaches are limited by the laborious, complex, and time-consuming nature of the nanolithography techniques, thereby impeding their application in wide use. Recently, we demonstrated a proof-of-concept methodology that enables the physical transfer of quasi-3D

metal-dielectric hybrid nanoantennas from their donor Si mold to a foreign receiver substrate (e.g., photodetectors) in a time and cost effective manner.(B. Kim et al., 2019) However, the application of the resulting nanoantennas in IR bandpass filters is challenged by the inherent brittleness of IR transparent dielectric spacers, such as SU-8 (i.e., fracture strain = 2-3%).(Mattsson, Thungstrom, Bertilsson, Nilsson, & Martin, 2007; Robin, Vishnoi, & Jonnalagadda, 2014)

Here, we unlock this material limitation and therefore establish mechanically and optically reliable quasi-3D metal-dielectric hybrid nanoantennas with a SU-8 dielectric spacer for IR bandpass filtering. The entire fabrication process of the nanoantennas occurred at room temperature with a temporary stress-absorbing layer, such as polymethyl methacrylate (PMMA), to prevent the brittle SU-8 dielectric spacer from mechanical damages. Following complete removal of the stress-absorbing layer, the resulting nanoantennas exhibited a capability of spectral filtering in IR region with respect to the peak transmission and full width at half maximum (FWHM). We investigated the effect of the structural design of these nanoantennas on IR bandpass filtering, and also validated the experimental results with computational analysis using finite integration technique (FIT) and finite element method (FEM).

3.2 Repetitive replication of quasi-3D plasmonic IR filters

Figure 3.1 schematically illustrates the fabrication process of the IR filters, which begins with a Si mold that contains pre-formed quasi-3D nanoposts or nanoholes via a lithographic patterning. The fabrication process of the Si mold is also schematically illustrated in Figure 3.2 with the detailed experimental procedures in the Materials and Methods section. First, thin films of Ni (10 nm)/Au (50 nm) were deposited on the Si mold using an e-beam evaporator, followed by the deposition of SU-8 (600 nm)/PMMA (1 μm) via spin-casting. Next, the entire structure was immersed in a bath of Ni etchant (TFB, Transene) to selectively etch the underneath Ni layer, and then rinsed with distilled water. A water-soluble tape (Aquasol) was attached on the top surface of the PMMA layer and then gently peeled off, allowing the remaining thin films (i.e., Au/SU-8/PMMA) to be cleanly delaminated from the Si mold. Both the water-soluble tape and the PMMA layer were then removed by placing on a bath of water and acetone sequentially. The underlying mechanics of this defect-free debonding process is discussed in the following section. Finally, the resulting structure (i.e., Au/SU-8) was transferred to a desired receiver substrate.

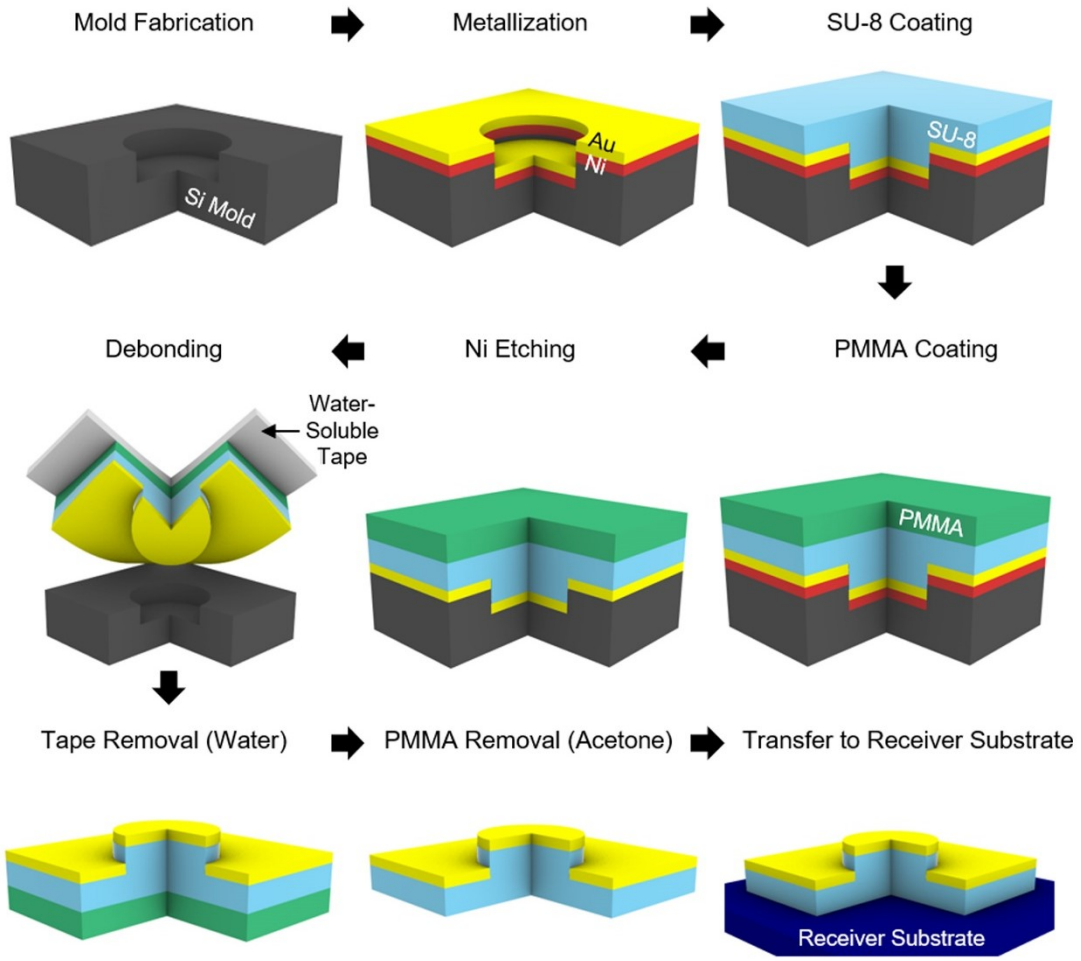

Figure 3.1. Schematic illustrations for the fabrication process of a single unit of a quasi-3D metal (i.e., Au)-dielectric (i.e., SU-8) nanoposts.

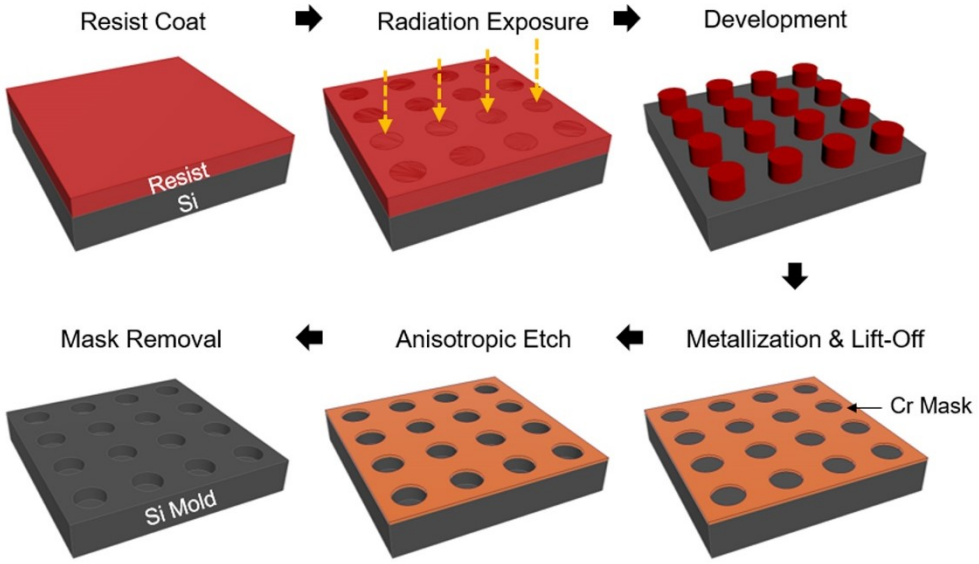

Figure 3.2. Schematic illustrations for the fabrication process of a donor Si mold.

Here, the SU-8 layer was used not only to serve as an IR transparent dielectric spacer through which the light can transmit at a wavelength of 3-10 μm, but also to be thinly deposited at the range of several hundred nanometers (i.e., < 600 nm).(Ashraf et al., 2019; Digaum et al., 2014) The minimum achievable thickness of the SU-8 layer was approximately 150 nm which is at least 26-fold thinner than that of other dielectric materials such as Ecoflex (i.e., > 4 μm-thick) using a diluent thinning agent such as the SU-8 2000 ThinnerTM (MicroChem, Inc.) and the Thinning Ecoflex SiliconesTM (Smooth-on, Inc.), respectively (Figure 3.3a). Therefore, the IR filters using a SU-8 dielectric spacer enabled advances in providing a stable transmission spectrum over the counterpart using an Ecoflex dielectric spacer (Figure 3.3b) despite their similar optical transparency in an IR regime (Figure 3.3c).

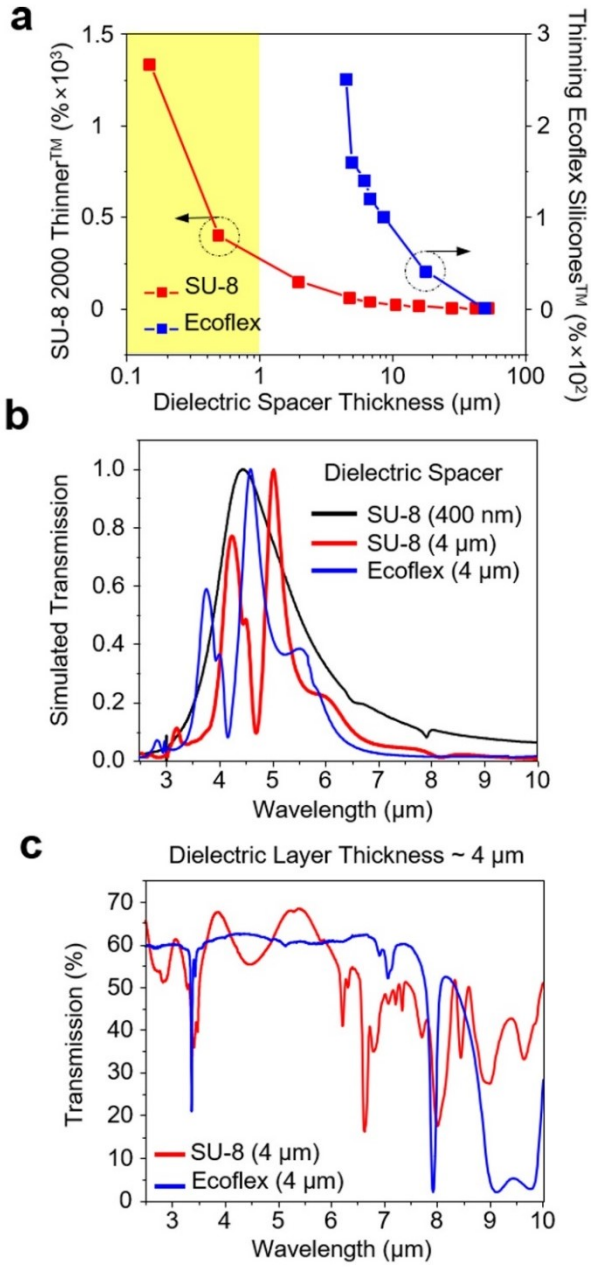

Figure 3.3. (a) Thickness of the dielectric spacer using SU-8 (red line) and Ecoflex (blue line) diluted with the SU-8 2000 ThinnerTM (MicroChem, Inc.) and the Thinning Ecoflex SiliconesTM (Smooth-on, Inc.), respectively. (b) Simulated transmission spectra as a function of wavelength for the IR filters using SU-8 (400 nm; black line), SU-8 (4 μm; red line), and Ecoflex (4 μm; blue line) as a dielectric spacer. (c) Transmission spectrum of SU-8 (red line) and Ecoflex (blue) at a fixed thickness of 4 μm.

Figure 3.4 shows schematic diagrams of a single unit of quasi-3D metal (i.e., Au arrays)-dielectric (i.e., SU-8 spacer) hybrid nanoantennas configured into nanoposts and nanoholes,

respectively. The geometrical parameters of the nanoantennas are denoted as follows: periodicity (p), diameter of the nanoposts and nanoholes (d), height or depth of the nanoposts and the nanoholes (t_p), thickness of the perforated Au films (t_m), and thickness of the dielectric spacer (t_d). Here, the SU-8 layer serves as an IR transparent spacer through which the light can transmit at a wavelength of 3-10 µm.(Digaum et al., 2014; Mattsson et al., 2007) As schematically illustrated in Figure 3.2, the fabrication of these nanoantennas began with a Si mold that contains pre-formed quasi-3D nanoposts or nanoholes via electron beam (e-beam) lithography. Thin-films of Ni (10 nm)/Au (50 nm) were deposited on the Si mold using an e-beam evaporator, followed by the deposition of SU-8 (600 nm)/PMMA (1 µm) via spin-casting. The entire structure was immersed in a bath of Ni etchant (TFB, Transene) to selectively etch the underneath Ni layer, and then rinsed with distilled (DI) water. A water-soluble tape (Aquasol) was attached to the top surface of the PMMA layer and then gently peeled off, allowing the remaining thin films (i.e., Au/SU-8/PMMA) to be cleanly delaminated from the Si mold. Both the water-soluble tape and the PMMA layer were subsequently removed by placing on a bath of water and acetone sequentially. The underlying mechanics of this defect-free debonding process is discussed in the following section. Finally, the resulting structure (i.e., Au/SU-8 or quasi-3D nanoantennas) was transferred to a desired receiver substrate.

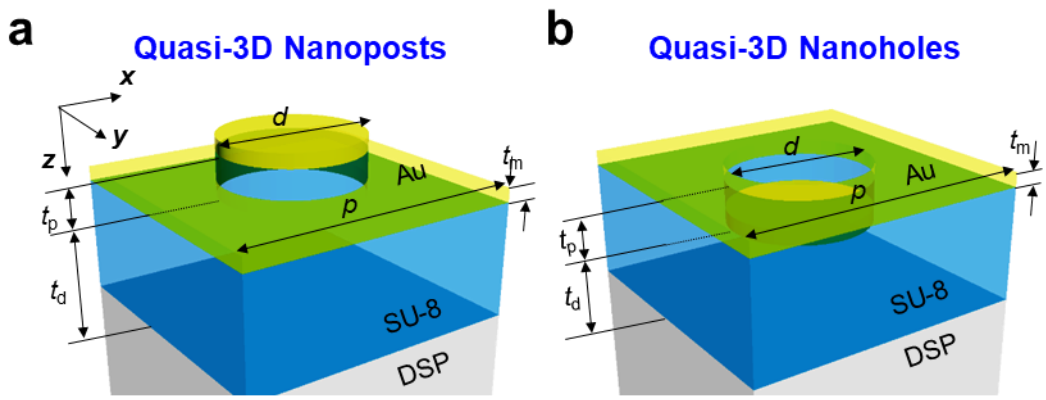

Figure 3.4. Schematic illustrations of quasi-3D nanoposts (p = 3 µm; d = 1.2 µm; t_m = 50 nm; t_p = 250 nm; t_d = 400 nm) and nanoholes (p = 3 µm; d = 1.2 µm; t_m = 50 nm, t_p = 330 nm, t_d = 230 nm), respectively.

Figure 3.5 present a series of optical and scanning electron microscopy (SEM) images of the transferred nanoantennas on a double-side polished (DSP) Si wafer (UniversityWafer). The results showed no evidence of visible damages or defects across the entire surface of the nanoantennas. The enlarged tilted-angle and cross-sectional views of the SEM images (bottom panels) highlight the clear physical separation at the gap between the SU-8 spacer and the Au arrays. Importantly, the donor Si mold was intact throughout the assembly process, allowing it to be reused multiple times after a piranha cleaning (Figure 3.6). The reusability of the Si mold can obviate the need for repetitive implementation of the e-beam lithography, which serves as a major cost- and time-saving factor of this assembly method.

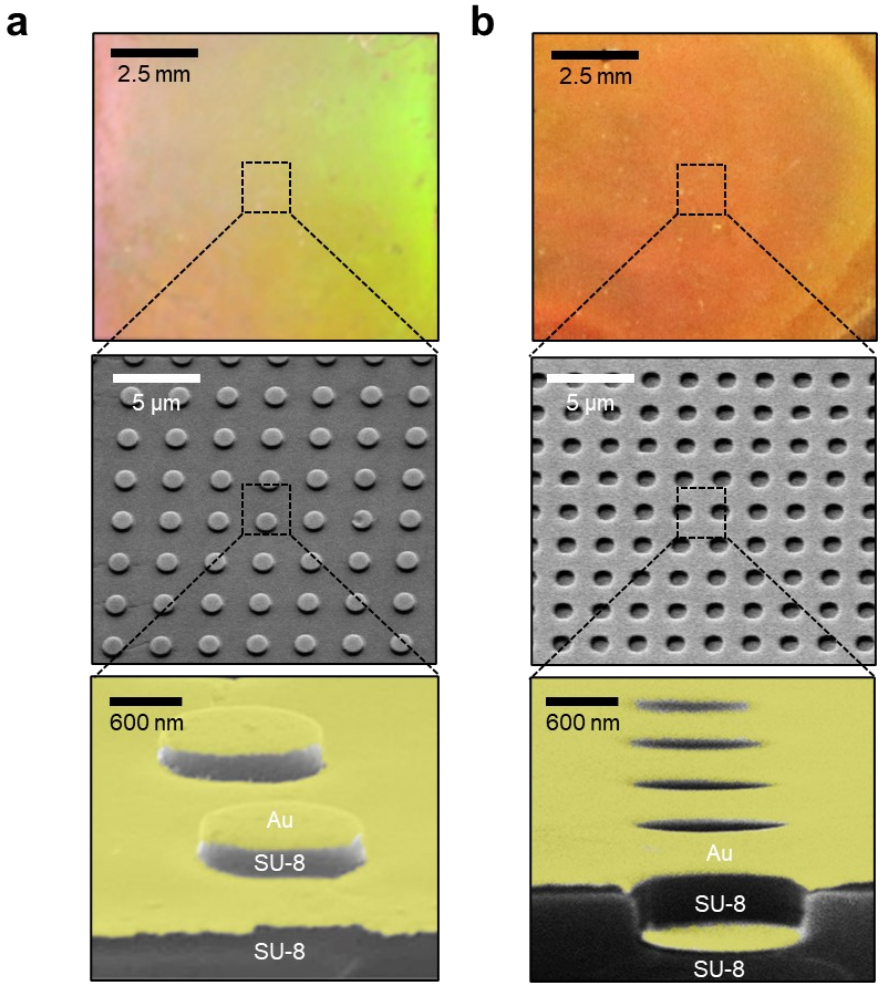

Figure 3.5. Optical photograph and scanning electron microscopy (SEM) images of the transferred nanoantennas.

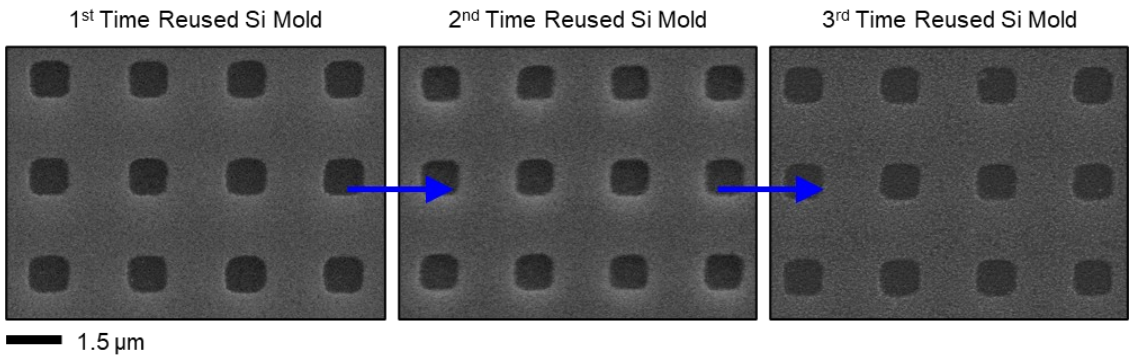

Figure 3.6. SEM images of a donor Si substrate through three times recycle.

3.3 Underlying mechanism of defect-free replication process

The defect-free debonding of the quasi-3D nanoantennas from the Si mold, even with the brittle SU-8 spacer, is attributed to the use of the temporary stress-absorbing layer (i.e., PMMA) that is capable of efficiently accommodating induced strains under mechanical deformations (i.e., debonding process). Figure 3.7 presents the FEM results displaying the distribution of principal strain (ε) for a 3 × 3 array of quasi-3D nanoposts (p = 3 μm; d = 1.2 μm; t_m = 50 nm; t_p = 250 nm; t_d = 400 nm) with (top panel) and without (bottom panel) a PMMA layer (1 μm) under debonding process at the peeling force of 40 mN. The inset images present that the maximum strains (ε_{max}) of 7% and 4% appeared at the edge of the quasi-3D nanoposts and nanoholes where the stresses are concentrated, respectively. For comparison, Figure 3.9 shows the corresponding FEM results in the presence of the interfacial adhesion (200 MPa) using a single unit of quasi-3D nanopost (left panel) and nanohole (right panel) with the Si mold. The ε_{max} of the nanoposts was < 1.8% with the presence of the PMMA layer, which is below the fracture limit of the SU-8 spacer (ε = 2-3%).(Robin et al., 2014) Whereas, the ε_{max} of the nanoposts increased up to 7.1% with the absence of the PMMA layer, which thereby may lead to cracking through the SU-8 dielectric spacer. The corresponding results for a 3 × 3 array of quasi-3D nanoholes (p = 3 μm; d = 1.2 μm; t_m = 50 nm, t_p = 330 nm, t_d = 230 nm) are shown in Figure 3.8, producing consistent outcomes. The ε_{max} of the nanoholes decreased from 3.7% to 1.2%, by more than 3-fold, with the presence of the PMMA layer. These results confirm that the PMMA layer is effective to protect the brittle SU-8 spacer from fracture throughout the debonding process. This is mainly attributed to the increased bending stiffness of the entire structure with the presence of the PMMA layer. Figure 3.10 present the bending stiffness (blue dotted line) and the ε_{max} (black dotted line) of the nanoposts and nanoholes

as a function of the PMMA thickness, respectively. The bending stiffness increased from 0.3 to 28 $\times 10^3$ GPa·μm^4 with the increased PMMA thickness from 0 to 2 μm, which resulted in the exponential decrease of the ε_{max} for both the nanoposts and the nanoholes. The green-filled area in these graphs indicates a zone where the defect-free debonding process occurred at the ε_{max} below the fracture limit of the SU-8 spacer (ε = 2 - 3%).(Robin et al., 2014) The results also suggest that the PMMA layer is required to be thicker than at least 1 μm and 0.4 μm for the defect-free debonding of the nanoposts and nanoholes, respectively. Representative images of the damaged nanoantenna that includes a PMMA layer thinner than these thresholds are shown in Figure 3.11.

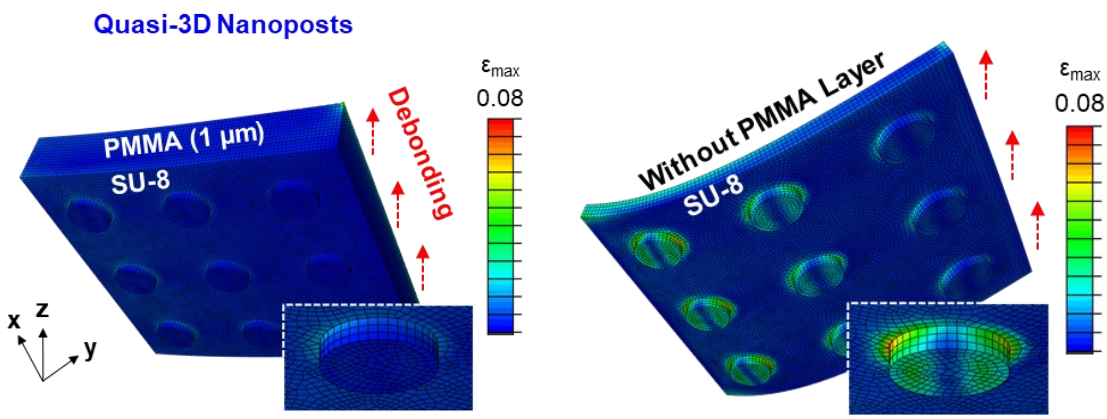

Figure 3.7. Principal strain distribution (ε) of nanoposts, comprising 3 x 3 square arrays without and with PMMA stress-absorbing layer.

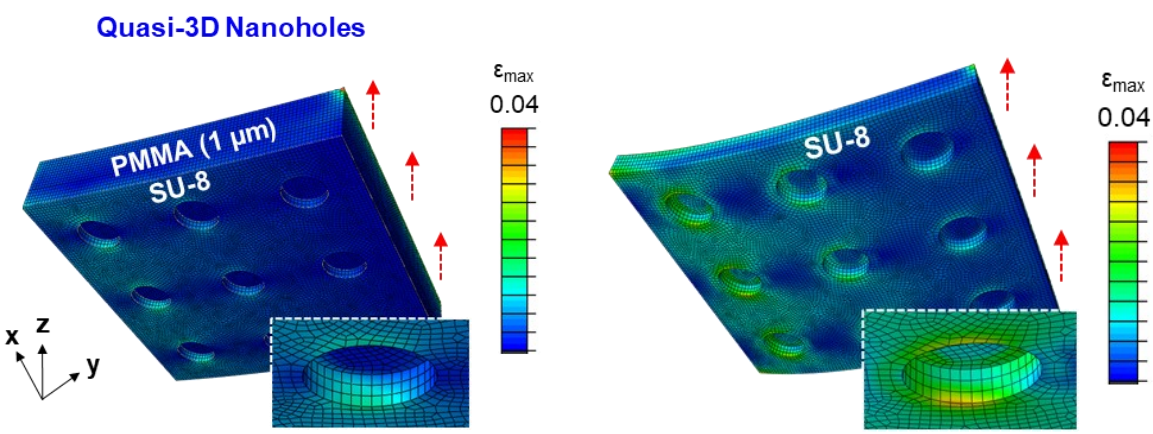

Figure 3.8. Principal strain distribution (ε) of nanoholes, comprising 3 x 3 square arrays without and with PMMA stress-absorbing layer.

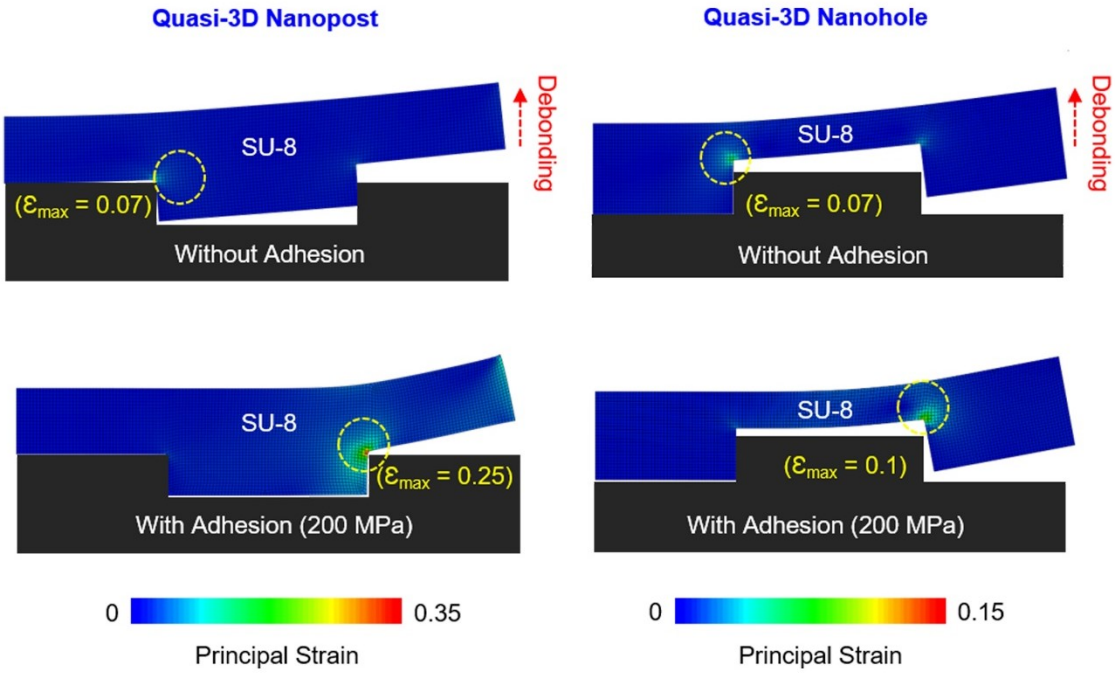

Figure 3.9. Principal strain distribution (ε) of nanoposts, comprising 3 x 3 square arrays without and with PMMA stress-absorbing layer.

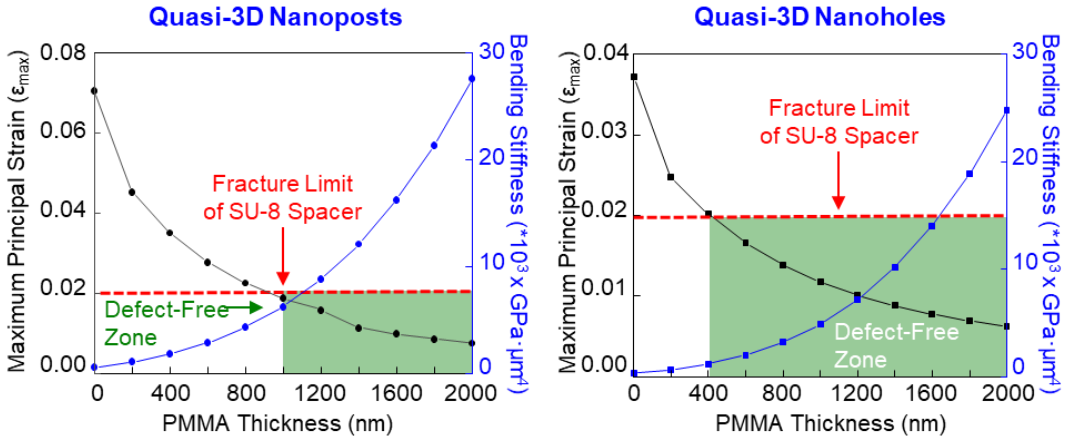

Figure 3.10. The maximal principal strain and bending stiffness of nanoantennas of function as the thickness of PMMA stress-absorbing layer increase from 0 to 2 μm.

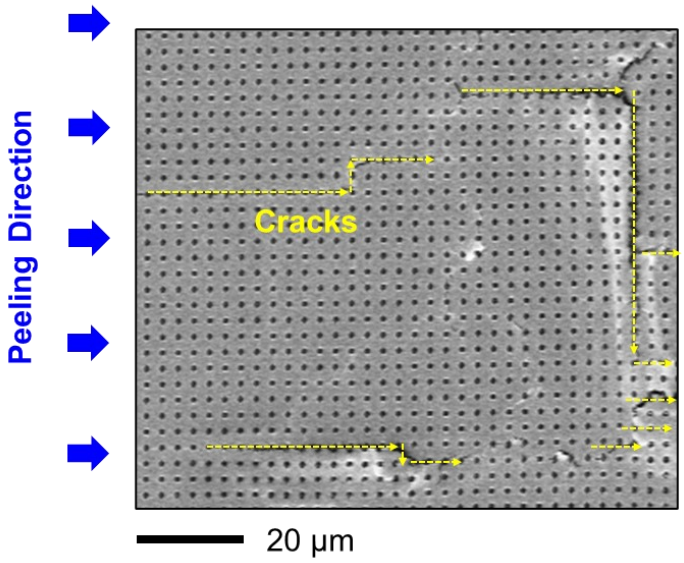

Figure 3.11. Representative SEM image of the damaged nanoantenna out of the defect-free zone.

Figure 3.12 shows the schematic illustration for a 3 × 3 square array of the nanoposts and nanoholes under debonding process from an edge, respectively. The dashed lines show the surface topology along the *i-i'* and *j-j'* directions. The corresponding FEM results in Figure 3.13 reveal the local strains of the nanoposts and nanoholes with (black dotted lines) and without (red dotted lines) the presence of a PMMA layer (1 μm-thick). Without the PMMA layer, the peak strains were sharply localized at the edges of the nanoposts and nanoholes along with both directions. The localized peak strains were attenuated along the direction of applied peeling force (i.e., *i-i'* direction) while they were unchanged in its perpendicular direction (i.e., *j-j'* direction). Overall, the localized peak strains along the *i-i'* direction were larger than those along the *j-j'* direction, all of which were beyond or near the fracture limit of the SU-8 spacer (ε = 2-3%).(Robin et al., 2014) These results indicate that cracks were initiated at the edge of where the peeling force was applied and then propagated along the *i-i'* direction more than the *j-j'* direction, as also evidenced in Figure 3.11. With the PMMA layer, the sharp localization of peak strains at the edges of the nanoposts and nanoholes was alleviated due to the stress-absorbing effect. This also resulted in the substantial reduction of the localized peak strains, by at least 57%, below the fracture limit of the SU-8 spacer along with both directions. These observations were consistent with experimental observations, providing important insights into identifying an optimal condition for the defect-free debonding of various quasi-3D nanoarchitectures with high-fidelity.

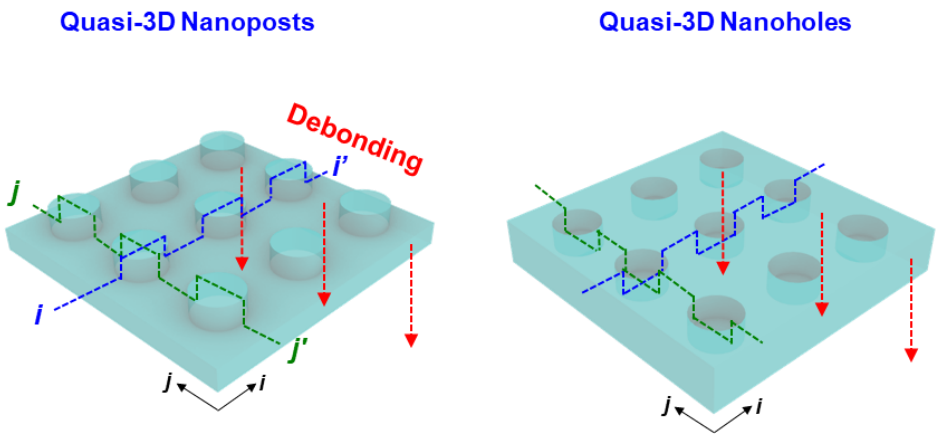

Figure 3.12. Schematic illustration for a 3 × 3 square array of nanoantennas under debonding process from an edge, respectively.

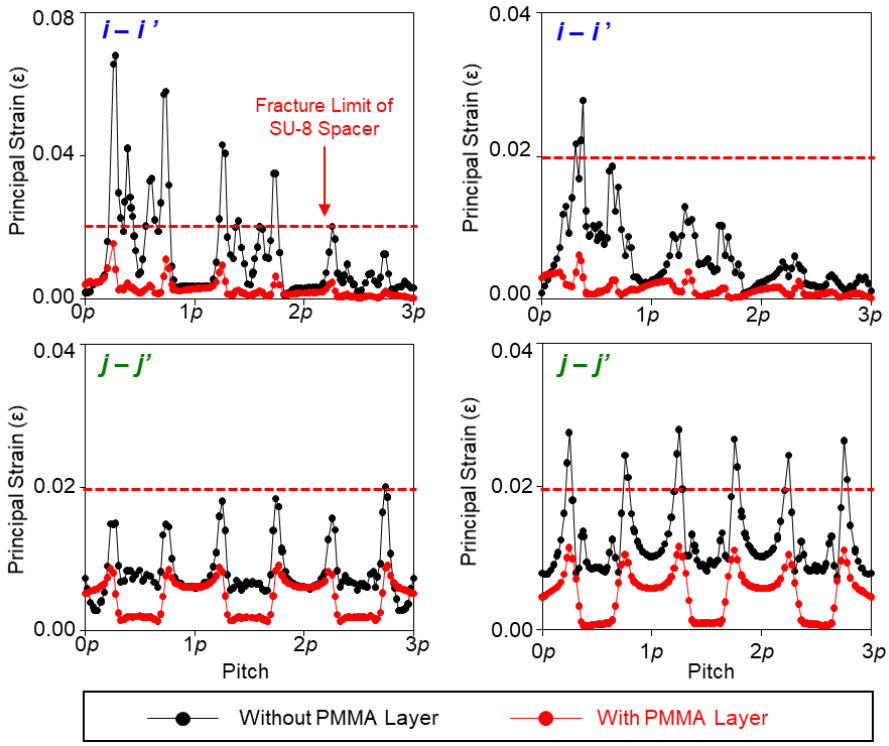

Figure 3.13. The scanned principal strain profile along *i-i'* and *j-j'* directions across the surface of quasi-3D nanoposts and nanoholes without and with 1 μm thick PMMA stress-absorbing layer.

3.4 Application in IR bandpass filtering

Figure 3.14 shows experimental (red dotted line) and computational (blue dotted line) results for the transmission filter effect of quasi-3D nanoantennas that contain the nanoposts and

nanoholes, respectively. The transmissions of these nanoantennas were measured at normal incidence using a Fourier transform infrared (FTIR) spectrometer (Nicolet 5700) in a wavelength range of 2.5–10.0 μm. An unpolarized FTIR beam was used to measure the transmission. The numerical simulation was performed using a 3D FIT solver (CST Microwave Studio), of which the details are shown in the Materials and Methods section. The results show that bandpass filtering occurred within the IR range at the peak wavelength of ~4.9 μm and ~5.3 μm for the nanoposts and nanoholes, respectively. The corresponding FWHMs occurred at the peak wavelength of 1.4 μm and 1.3 μm. The experimental and computational results were in an agreement with a discrepancy of less than 7% (peak wavelength) and 2% (FWHM), which may come from imperfection and variation in the fabrication of Si molds. Also, repetitive transmission spectra measured across the transferred quasi-3D posts and holes samples (1 × 1 cm^2) show very good uniformity with only small variations in spectra.

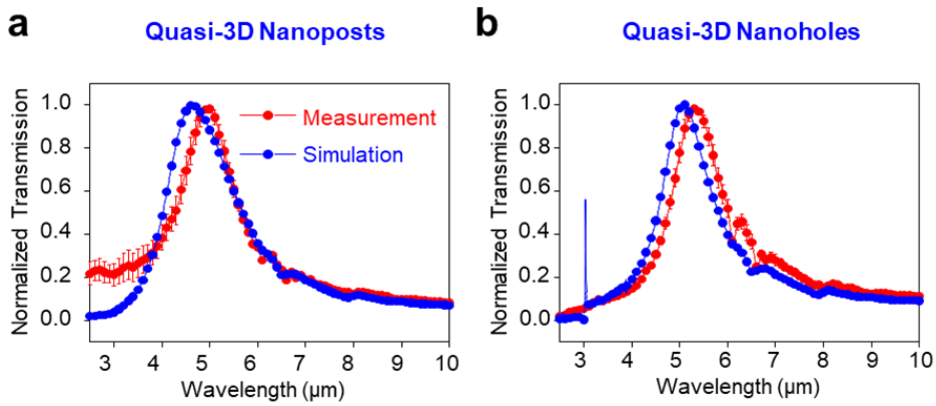

Figure 3.14. Analysis of transmission spectra of nanoantennas. Note that spectra measured across the sample (1 x 1 cm^2) show very good uniformity with only small variations in spectra.

Figure 3.15 shows the 2D surface plots of normalized transmission for these nanoantennas as functions of wavelength and periodicity (p). The results exhibited a clear spectral shift of the transmission peak toward a longer wavelength for both the nanoposts (from 3.2 to 6.0 μm) and nanoholes (from 3.3 to 6.3 μm) as the p increased from 2 to 4 μm with weak absorption at the wavelength of 3.3, 6.2, 6.6 and 8 μm. The peak wavelength and FWHM of these nanoantennas were tunable within the ranges of from 3 to 6 μm and from 0.5 to 2.5 μm through the adjustment of their geometrical parameters such as d, t_p, t_m, and t_d (Figure 3.16). Here, the t_d is a critical

parameter to determine a Fabry-Perot optical cavity through which multiple light reflections occur between the perforated Au film and the Si surface.(Chanda, Shigeta, Truong, et al., 2011) The peak wavelength is susceptible to any change of the gap space ($t_g = t_p - t_m$) between the perforated Au film and the Au disks which results in the spectral shift of a localized surface plasmon resonance wavelength.(C. Wang, Zhang, Song, & Chou, 2014) Specifically, a red-shifting of the peak wavelength occurs as the t_p decreases or the tm increases due to an excited electric field at the edge of the Au disks via a localized surface plasmon resonance.(W.-D. Li, Ding, Hu, & Chou, 2011) Therefore, any residual deposition of Au to the sidewall of the quasi-3D nanoposts and nanoholes would affect the performance of the IR filters due to the reduced gap space (t_g) (Figure 3.17). Figure 3.18 shows the corresponding results of the nanoantennas that contain a PMMA spacer (1 µm-thick) as a control comparison. The results show that strong spectral interferences (i.e., the absorption of IR radiation) occurred at wavelengths of 3.3, 5.8, 7.0, 8.3, and 8.7 µm due to the stretching vibration of C-O-C and C-H bonds in the PMMA spacer, thereby hindering IR bandpass filtering.(Jitian & Bratu, 2012b)

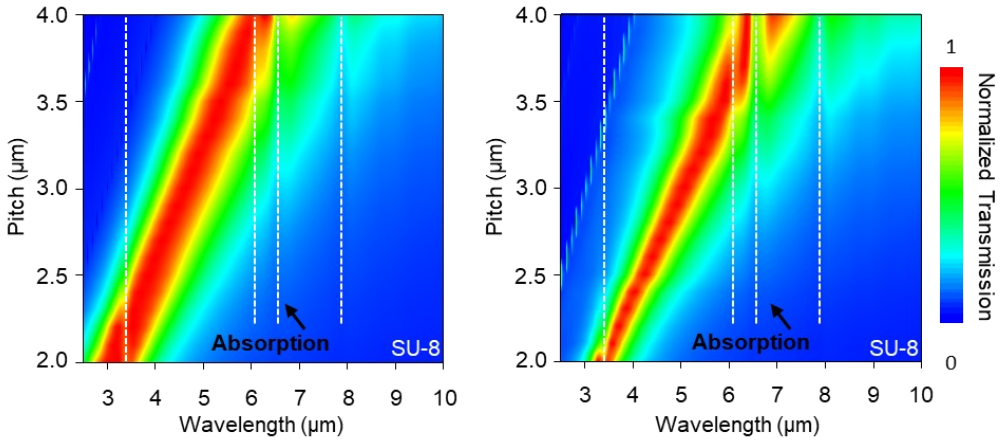

Figure 3.15. 2D surface plots of normalized transmission of quasi-3D nanoposts and nanoholes, as a function of array periodicity (p) and wavelength (µm) with SU-8 dielectric spacer.

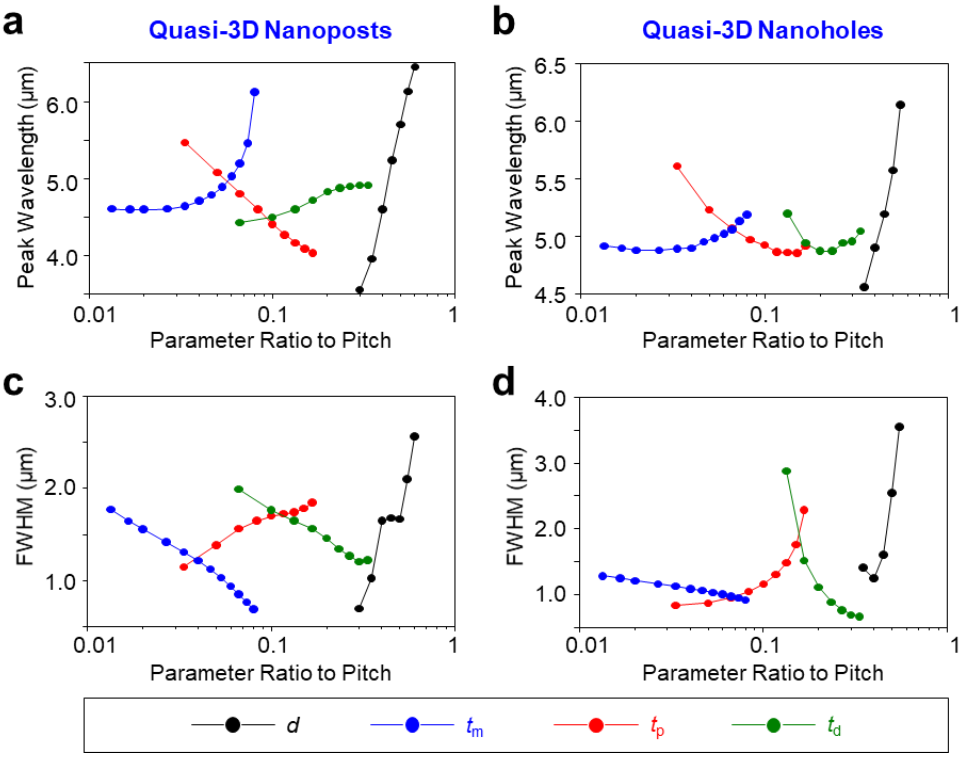

Figure 3.16. Peak wavelengths and FWHMs of quasi-3D nanoposts and nanoholes depending on the geometrical parameters (d, t_p, t_m, t_d).

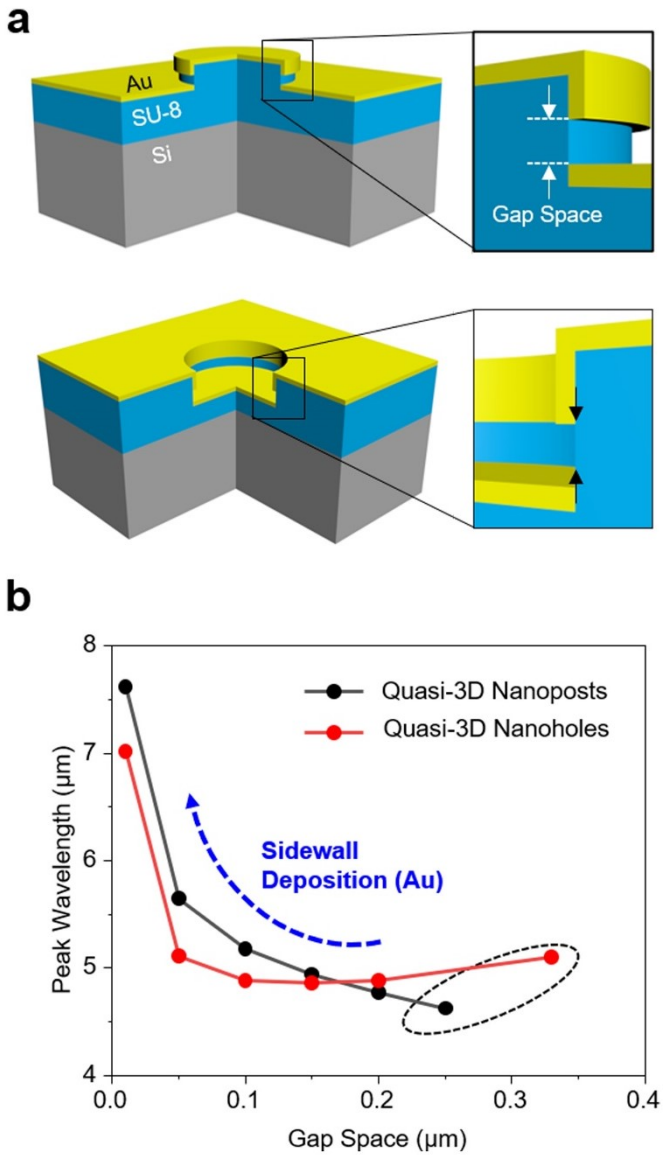

Figure 3.17. (a) Schematic illustrations of a single unit of the quasi-3D nanoposts (top panel) and nanoholes (bottom panel) with the residual deposition of Au at the sidewall. (b) Simulated peak wavelength with the reduce gap space by the sidewall deposition of Au.

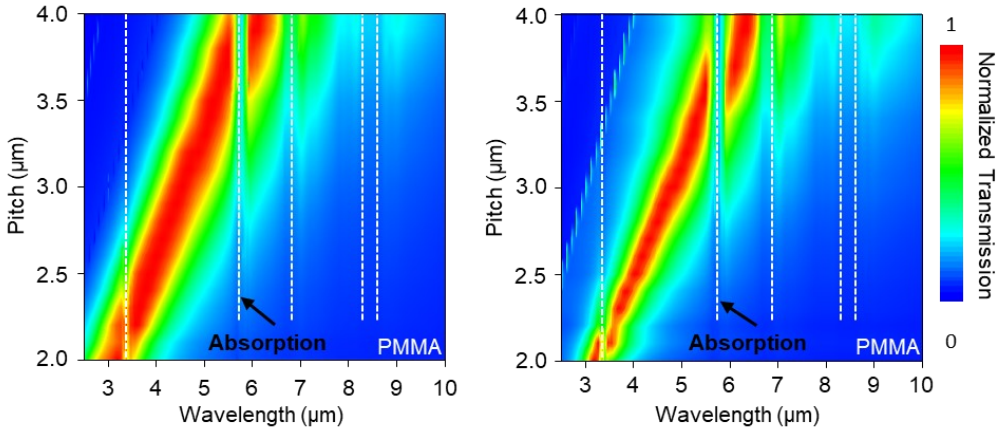

Figure 3.18. 2D surface plots of normalized transmission of quasi-3D nanoposts and nanoholes, as a function of array periodicity (p) and wavelength (μm) with PMMA dielectric spacer.

3.5 Methods

3.5.1 Fabrication of Donor Si Mold

The fabrication of the donor Si mold began by producing a quasi-3D array of circle-shaped apertures (i.e., pillars) on a Si wafer through the photolithographic patterning of a negative (positive)-tone photoresist (AZ5214, MicroChemicals). A thin layer (20 nm-thick) of Cr was then deposited to serve as a mask layer using an electron beam (e-beam) evaporator. A predominately anisotropic CF_4/O_2 plasma reactive ion etch (RIE) was applied to generate an undercut at the RF power of 100 W with CF_4 (13 sccm) and O_2 (2 sccm) gases under the pressure of 45 mTorr. Finally, the Cr mask layer was removed by immersing in a bath of a Cr etchant (Transene 1020) for 30 seconds to complete a donor Si mold. The orthogonal pitches of both the 2D gratings p_x (pitch along x-axis) and the p_y (pitch along y-axis) were fixed at 3.0 μm ($p_x = p_y = p$). The diameter of the circular holes (pillars) was fixed at 1.2 μm.

3.5.2 Numerical Simulation of Transmission

Numerical simulation was performed using a commercial 3D finite integration technique (FIT) solver (CST Microwave Studio). This simulation was to obtain the transmission spectra of the nanoantennas and therefore to understand the underlying physics and optics including Fabry-Perot optical cavity, guided-mode resonance, localized surface plasmon resonance, and surface

plasmonic resonance. (E. K.-w. Huang et al., 2011; E. K.-w. Huang et al., 2012; S. J. Lee et al., 2011; J. A. Montoya, Z.-B. Tian, S. Krishna, & W. J. Padilla, 2017; Murray & Barnes, 2007; Ooi, Chu, Ang, & Bai, 2013; Ozbay, 2006) As schematically illustrated in Figures 3.4, we implemented a single unit cell with appropriate boundary conditions that include (1) perfect magnetic conductor (PMC for short, $H_t = 0$) in the xz-plane; (2) perfect electric conductor (PEC for short, $E_t = 0$) in the yz-plane; and (3) a transverse electromagnetic (TEM) plane wave propagating in the z-direction. The direction of polarized incoming light was set to be parallel to the x-axis. We obtained the wavelength-dependent complex S-parameters, S_{ij}, where the subscripts i and j represent the waveguide ports at Si substrate and air, respectively. The simulated transmission from j (air) to i (Si) was calculated by $|S_{ij}|^2$. The refractive index of Si was taken as $n_{Si} = 3.42$. (Y.-B. Chen, 2009) The Au was defined by the Drude model with the plasma frequency of $w_p = 1.38 \times 10^{16}$ Hz and the collision frequency of $w_c = 5.71 \times 10^{13}$ Hz.(Ordal, Bell, Alexander, Long, & Querry, 1985) The values of real and imaginary parts of permittivity in SU-8 and PMMA were used from the literature.(Digaum et al., 2014; Jitian & Bratu, 2012a)

3.5.3 FEM Analysis

The FEM analysis was performed using a commercial ABAQUS/standard package (Dassault Systems). The materials used in this study (e.g., Au, SU-8, and PMMA) were modeled by C3D8R elements (8 nodes linear brick; reduced integration solid elements). These materials were deformed by elastic behavior with the mechanical modulus (E) of 77.2, 4.1, and 3 GPa and the Poisson's ratio (ν) of 0.42, 0.22, and 0.37, respectively.(Korsunsky, Cherian, Raiteri, & Berger, 2007; Marcin et al., 2010; T. Xu et al., 2016) The pulling force (40 mN) to initiate the delamination was applied at a corner of the nanoantennas.

3.5.4 FTIR measurements

The normal incidence transmission was measured using a Fourier transform infrared (FTIR) spectrometer (Nicolet 5700) in a wavelength range of 2.5–10.0 μm using a KBr beam splitter and a mercury-cadmium telluride (MCT) detector. The transmission spectra were recorded with a resolution of 4 cm^{-1}. A square pinhole (1 mm × 1 mm) was used to measure the structural uniformity of the nanoantennas across a large area (1 × 1 cm^2).

3.6 Conclusion

The results in this study revealed the underlying mechanism for the defect-free transfer of quasi-3D nanoantennas from their donor Si molds to a receiver substrate, even with the presence of an extremely brittle IR-transparent spacer, such as SU-8. This fundamental understanding enabled the reuse of the donor Si molds multiple times without degradation, thereby eliminating the need for repetitive implementation of nanolithography unlike current approaches. The replicability of Si molds could lead to a significant reduction of cost and time for the production of various quasi-3D nanoantennas of interest. The quality, reliability, and performance of the resulting nanoantennas in IR bandpass filtering were validated through experimental and computational analysis, suggesting a route for their pragmatic application in multispectral imaging systems.

4. ELECTROCHEMICAL REACTION-DRIVEN DELAMINATION OF THIN FILM ARCHITECTURES OVER 4 INCH WAFER-SCALE

4.1 Background

In the previous section, nanoassembly methods of thin-film architectures have been developed to circumvent the limitation of mismatch between conventional manufacturing process conditions and nonconventional flexible, stretchable substrates. The novel methodology can require no chemical and thermal treatments and physical forces (except weak van der Waals contact force), which enable assembly on the nearly arbitrary materials and structures. However, these steps require time-consuming processes, limiting the large-scale production of thin-film nanoarchitectures. To tackle this challenge, we have developed a microbubble-driven transfer printing method that allows a one-step debonding of large-scale thin-film architectures from the donor substrate by bubble generation without any physical contact. The delaminated thin-film architectures can be afloat on the surface of the water, allowing them to be aligned and placed on the arbitrary receiver substrate. Importantly, this method requires no temperatures and chemicals, except electrolyte solution, on the target receiver substrates, and therefore almost any kind of substrates can serve as the receiver substrate.

4.2 Microbubble-driven delamination of Quasi-3D plasmonic nanoarchitectures

The process begins by deposing a titanium (Ti) layer (5 nm) and gold (Au) layer (20 nm) using a PVD sputtering system to serve as an anode at following electrochemical reactions, followed by deposition of a Silicon dioxide (SiO_2, 10nm thick) and gold (Au, 50nm thick) to serve as separation layer and surface plasmon layer using e-beam evaporator with 0.3 Å/s deposition rate. The next step involves spin-casting of SU-8 (500 nm) and PMMA (50nm) to serve as a dielectric spacer and supporting layer. The entire architecture is then immersed in a solution of sodium chloride (NaCl) electrolyte solution. An edge of the Si wafer was scratched by using a commercial razor blade to be directly contacted to the electrolyte solution, leading to the following electrochemical reactions (Figure 5.1):

$$4\ H_2O + 4\ e^- = 2H_2\ \text{(microbubbles)} + 4\ OH^-\ \text{(@ Cathode)}$$

$$2\ H_2O - 4\ e^- = O_2 + 4\ H^+\ \text{(@ Anode)}$$

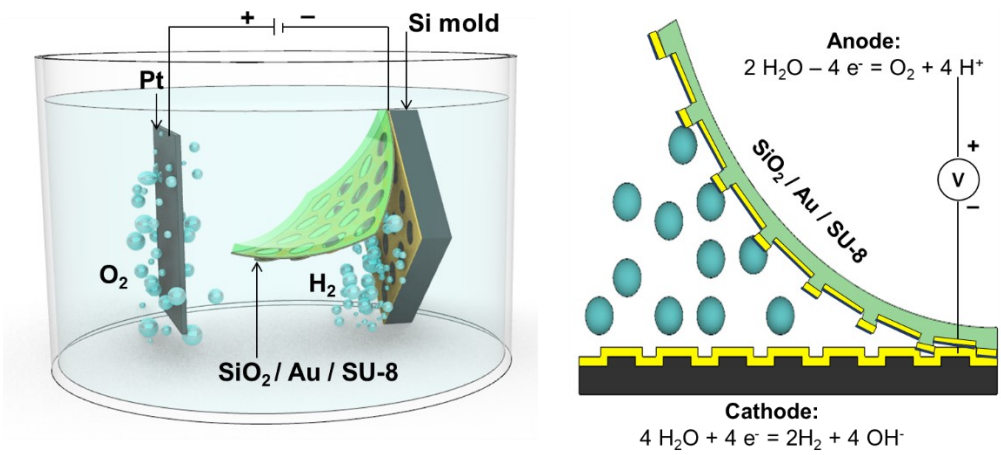

Figure 4.1. Schematic illustration of basic procedures of the microbubble-driven delamination of quasi-3D plasmonic nanoarchitectures.

The one-step microbubble-driven transfer printing method can provide intact separation of a quasi-3D plasmonic film with a successful yield of nearly 100%. Figure 5.2 shows the representative optical and SEM images for plasmonic nanopost arrays, each of which is transferred on the double-side-polished Si wafer without visual damages or defects during/after the one-step transfer printing process. Also, the transmission spectra of experimental results show the continued agreement between without SiO_2 (blue color) and with SiO_2 (red color), each of which is obtained using the Fourier transform infrared (FTIR) spectrometer (Nicolet 5700), showing no effect of thin separation layer on the transmission of plasmonic films.

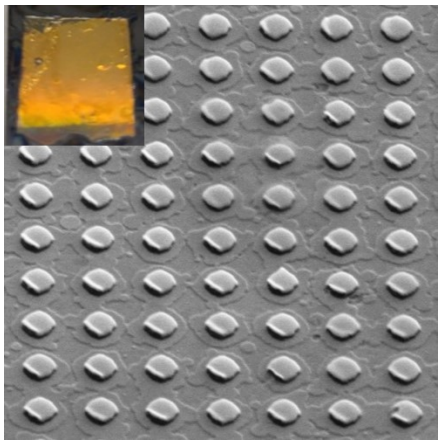

Figure 4.2. Representative optical and SEM images of the transferred plasmonic nanopost arrays on double-side-polished Si wafer.

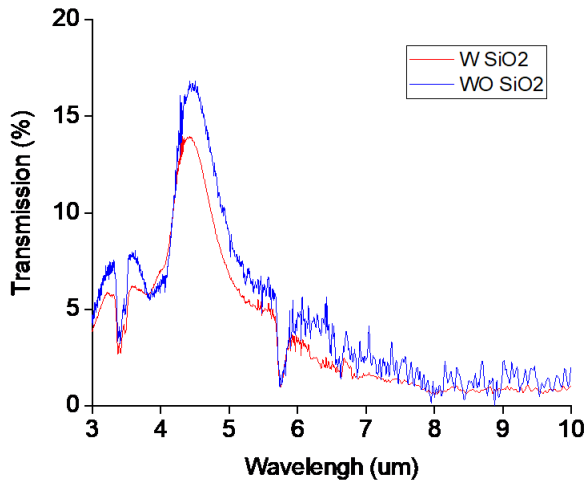

Figure 4.3. Transmission spectra measurements with and without separation SiO_2 (10 nm thick).

4.3 Microbubble-driven delamination of thin-film electronics

4.3.1 Microbubble-driven delamination process

The delamination process begins with depositing layers of Ti (5 nm) / Au (50 nm) and polyimide film (1 µm) on a Si wafer to serve as anode for microbubble-driven delamination process and a dielectric layer, respectively, followed by fabrication of various electronic devices on the top via conventional fabrication processes. The next step involves spin-casting a temporary protecting layer of PMMA on the Si wafer. Then, an edge of the Si wafer was trimmed by using a commercial razor blade to be directly contacted to the electrolyte solution, leading to the following electrochemical reactions (Figure 5.4):

$$4\ H_2O + 4\ e^- = 2H_2\ \text{(microbubbles)} + 4\ OH^-\ \text{(@ Cathode)}$$

$$2\ H_2O - 4\ e^- = O_2 + 4\ H^+\ \text{(@ Anode)}$$

A demonstration showing the interfacial debonding of a 4-inch wafer-size testbed sample in a NaCl solution bath appears in Figure 5.5. In the end, a free-standing thin-film electronic is conformably laminated onto target surfaces, such as the textile is shown in Figure 5.6.

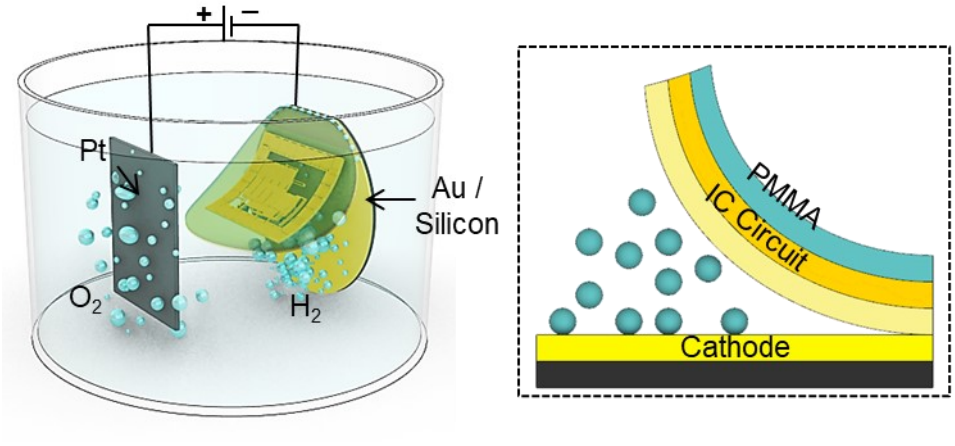

Figure 4.4. Schematic illustrations of basic procedures of the microbubble-driven delamination of thin-film nanoelectronics from its fabrication Si wafer.

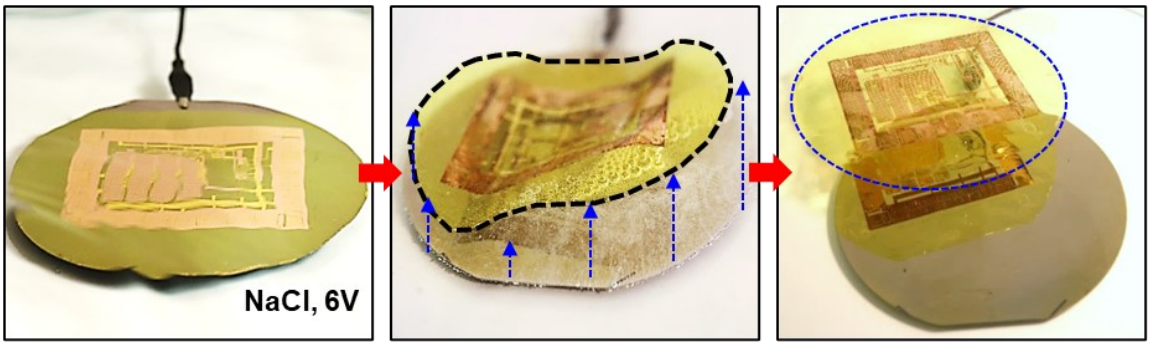

Figure 4.5. Schematic illustrations of basic procedures of the microbubble-driven delamination of thin-film nanoelectronics from its fabrication Si wafer.

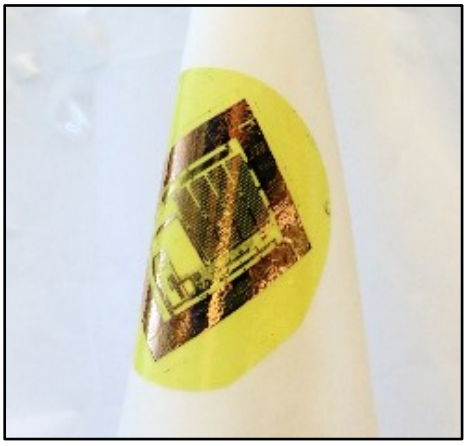

Figure 4.6. Photograph of transferred thin-film electronic laminated on textile.

4.3.2 Component-level validation of transferred thin-film nanoelectronics

Fig. 5.7 shows representative microscopic images of the component level of thin-film nanoelectronics, including a resistor (Left image), a diode (Middle image), and a transistor (Right image), each of which is transferred from its fabrication Si wafer. Fig. 5.8 presents the output characteristics obtained from these test bed samples before (black lines) and after (colored dashed line) the delamination process, showing no degradation of component-level thin-film nanoelectronics.

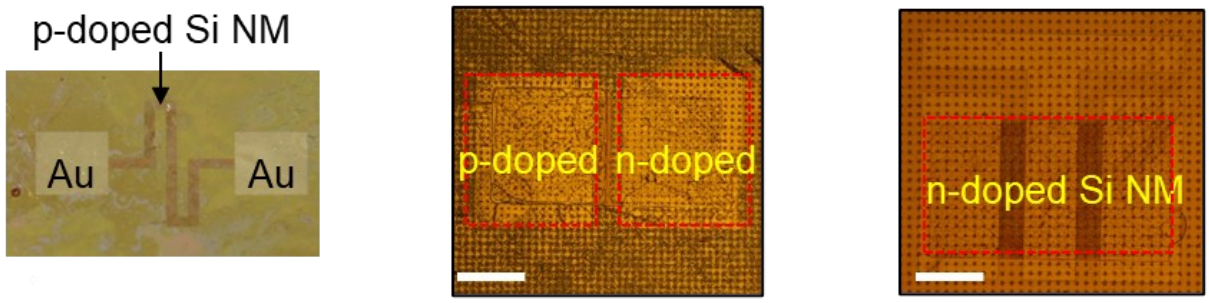

Figure 4.7. Microscope images showing the transferred Si NM-based resistor (Left), Si NRs-based diode (Middle), and Si NM-based transistor (Right) from its fabrication Si wafer. (Scale bars: 40, 200, and 250 μm, respectively.).

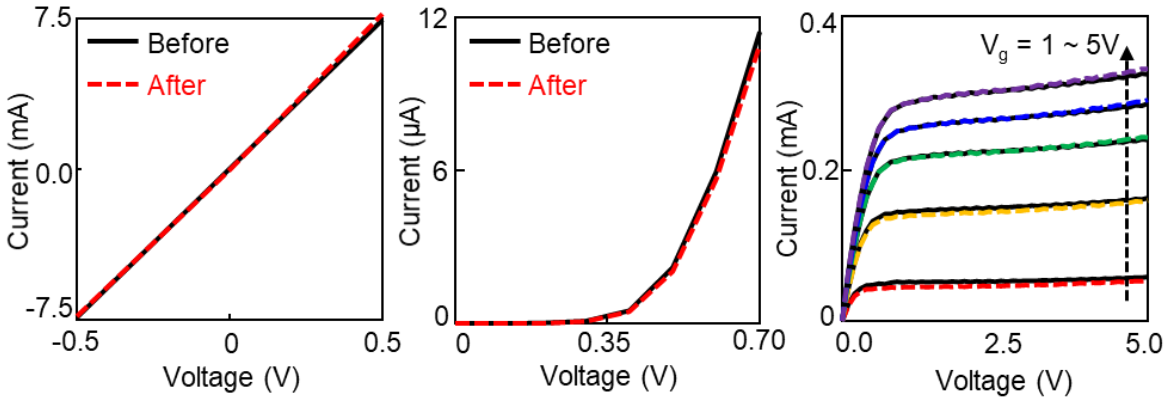

Figure 4.8. Corresponding electrical characteristics to each device before and after the transfer printing process.

4.3.3 Transferred thin-film biosensors

An interesting aspect of this transfer printing process arises from its unique ability that can create complex shapes of final products including bio-integrated electronics. Fig. 5.9 presents an experimental demonstration of the testbed biosensor, including a thin layer of Au (100 nm) and PI (1 μm) in the form of filamentary serpentine traces. This transferred biosensor allows high-quality recordings of electrocardiograms (ECG) and electromyograms (EMG) by applying the device on the chest (Figure 5.9, Left) and the forearm (Figure 5.9, Right). The resulting ECG and EMG data by exploiting the transferred biosensor are qualitatively comparable to those recorded with the commercial pads.

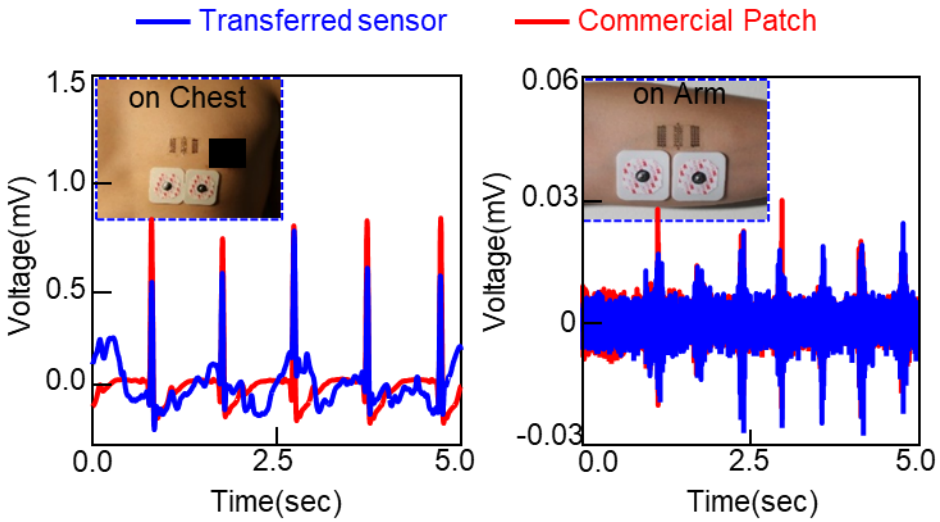

Figure 4.9. Corresponding electrical characteristics to each device before and after the transfer printing process.

5. RAPID CUSTOM PRINTING OF SOFT POROELASTOMERS FOR BIOMEDICAL DEVICES

A version of this chapter is pending publication in Nature Communications.

5.1 Background

Printed biosensors are integral to the development of various medical research platforms and their broad applications at all scales, from cellular to organ level.(Jin et al., 2017; Lind et al., 2017; Loo, Ho, Turner, & Mak, 2019; L. Xu et al., 2015; Zhu et al., 2018) Direct ink writing (DIW) of multidimensional functional architectures on various biological substrates enables rapid prototyping and customization of a range of biosensors with geometrical complexities.(Muth et al., 2014; A. D. Valentine et al., 2017; Zhu, Park, & McAlpine, 2020) This approach eliminates the need for multiple steps, masks, and dedicated tools that are typically required in conventional lithography-based techniques.(Amjadi, Pichitpajongkit, Lee, Ryu, & Park; I. Kim et al., 2018; M.-S. Lee et al., 2013; S.-M. Park et al., 2015; Tybrandt et al., 2018) Advanced strategies involve the use of conducting viscoelastic polymers or silicone composites containing conductive nanofillers to serve as dispensable inks for a nozzle injection system that allows for automated rapid prototyping.(Guo, Qiu, Meng, Park, & McAlpine, 2017; Khan et al., 2020; Kraft, Molina-Lopez, Son, Bao, & Murmann, 2020; Molina-Lopez et al., 2019) To this end, it requires precise control of the rheological properties of the inks in order to (1) ensure high-precision printability for sophisticated rendering at the microscale and (2) prevent the hindering of the densely dispersed nanofillers from the polymerization of the inks.(Daalkhaijav, Yirmibesoglu, Walker, & Mengüç, 2018) Despite great successes, these materials exhibit both mechanical and electrical hysteresis under periodic large strains due to their viscoelastic nature or/and result in irreversible degradation in conductivity due to the difficulty of maintaining the percolation network of the conductive nanofillers. (H. Liu et al., 2018; Sekitani et al., 2008; Z. Wang et al., 2020) Besides, these materials may produce a risk for delamination from the biocompatible substrates under a large deformation due to the low interaction energy at the interface and the discrepancy in their intrinsic elasticity.(Mei, Landis, & Huang, 2011) The fundamental limitations of these materials impede their implementation in medicine, particularly under conditions that demand long-term reliable recording against repetitive loading such as the cardiac cycle.

Herein, we introduce a sponge-like form of poroelastic silicone composite with optimal rheological properties that allow it to be printed in a nozzle injection system at the microscale. The resulting composite material provides the following unique features: (1) poroelastic behavior (rather than viscoelastic behavior) with reversible compressibility that can effectively suppress both mechanical and electrical hysteresis against repetitive loading cycles;(G. Chen et al., 2019) (2) exceptional softness due to the ultralow mechanical modulus ($E < 30$ kPa) of the sponge-like foam, which is lower than that of commercial dispensable inks ($E > 1.11$ MPa; SE 1700, Dow Corning) by more than 10-fold and comparable to that of human cardiac tissues (29-41 kPa);(J. Park et al., 2016) and (3) reliable structural integrity in which conductive nanofillers are integrated through the internal pores of the sponge-like foam to minimize the risk of delamination or separation against cyclic deformations.(Jeong et al., 2012) The comparison of this poroelastic silicone composite with other existing materials in terms of the mechanical and electrical properties is shown in Table 4.1. In this report, we elucidated the structure-property relationships of this composite material at the molecular and microsystemic levels and then evaluated its applicability in rapid custom prototyping of stretchable biosensors. To demonstrate the utility of this concept in medical practice, we produced a range of custom-fit biosensor arrays tailored for simultaneous recording and imaging of acute myocardial infarction *in vivo*.

Table 5.1. Comparisons of the poroelastic silicone composite with other existing materials in terms of the mechanical and electrical properties. The following abbreviations are used in this table. Nanowire (NW); Carbon Nanotube (CNT); Poly(Ethylene Oxide) (PEO); Carbon Black (CB); Thermoplastic PolyUrethane (TPU); Styrene-Butadiene-Styrene (SBS); Polydimethylsiloxane (PDMS)

Patterning Process	Materials	Conductivity	Maximum Stretchability	Young's Modulus
Direct Ink Writing	Poroelastic Biosensor (This Work)	$7.72 \pm 1.52\ \Omega\cdot sq^{-1}$	150%	0.15 MPa
	Ag Flakes/PEO	$13{,}800\ S\cdot cm^{-1}$	300 %	0.4 MPa
	CB/TPU	$0.841\ S\cdot cm^{-1}$	-	8.8 MPa
	Ag/PA	$15{,}200\ S\cdot cm^{-1}$	-	-
	Ag Flakes/TPU	$10^4\ S\cdot cm^{-1}$	240%	2.3 MPa
	Ag/Dragon Skin	500 Ω	250%	0.8 MPa
Moulding	Ag NWs/SBS	$11{,}210\ S\cdot cm^{-1}$	50%	40 MPa
	Ag-Au NWs/SBS	$72{,}600\ S\cdot cm^{-1}$	840%	37.4 MPa
Photolithography	Graphene-Ag NWs/PDMS	$33\ \Omega\cdot sq^{-1}$	100%	-
	Ag NWs/PDMS	$26.1\ \Omega\cdot sq^{-1}$	73%	-
	Au/Ni/PDMS	$1.9\ \Omega\cdot sq^{-1}$	80%	-
Screen Printing	Ag Flakes/Fluoroelastomer	$0.06\ \Omega\cdot sq^{-1}$	450%	-
	CNTs/Fluorinated rubber	$57\ S\ cm^{-1}$	134%	-
Mask Patterning	Ag NWs/PDMS	7.5 Ω	70%	6.32 MPa
	Au-TiO_2 NWs/PDMS	$0.63\ \Omega\cdot sq^{-1}$	100%	-
	Ag Flakes/PDMS	$5{,}695\ S\cdot cm^{-1}$	80%	-

5.2 Custom design and prototyping of poroelastic biosensors

Figure 4.1 displays schematic illustrations and the corresponding optical images for procedures to design and fabricate a custom poroelastic biosensor array. The initial design process began by capturing the overall size, geometry, and structure of the infarcted area of a specific heart

through four-dimensional (4D) segmentation (i.e., 3D geometric volume over a cardiac cycle) of the myocardium constructed by lofting sequential short axis (SAX) endocardial and epicardial boundaries from ultrasound images (Figure 4.1a).(Soepriatna et al., 2019; Updegrove et al., 2017) Details of the 4D heart segmentation and lofting are included in the Methods section. This 3D geometry was taken into consideration to precisely scale, adjust, and tailor the overall layout of the device to meet the requirement of a specific geometric accuracy. This aspect allowed the device to seamlessly cover the entire infarcted area when placed on the curvilinear epicardial surface of the heart in a manner that enabled the accurate alignment of the embedded recording electrodes to the position and orientation of the infarcted area. The subsequent printing process began by directly writing a formulated ink on a Si wafer using an automated nozzle injection system equipped on a three-axis computer-controlled translation stage (Nordson EFD; minimum inner diameter of nozzles = 100 μm; repeatability = ±3 μm; dispensing rate = 20 $mm \cdot min^{-1}$). This setting provides the capability to uniformly render microscale motifs (thickness ≥ 50 μm-thick; width ≥ 100 μm-wide) that fit into the pre-designed layout of the device.

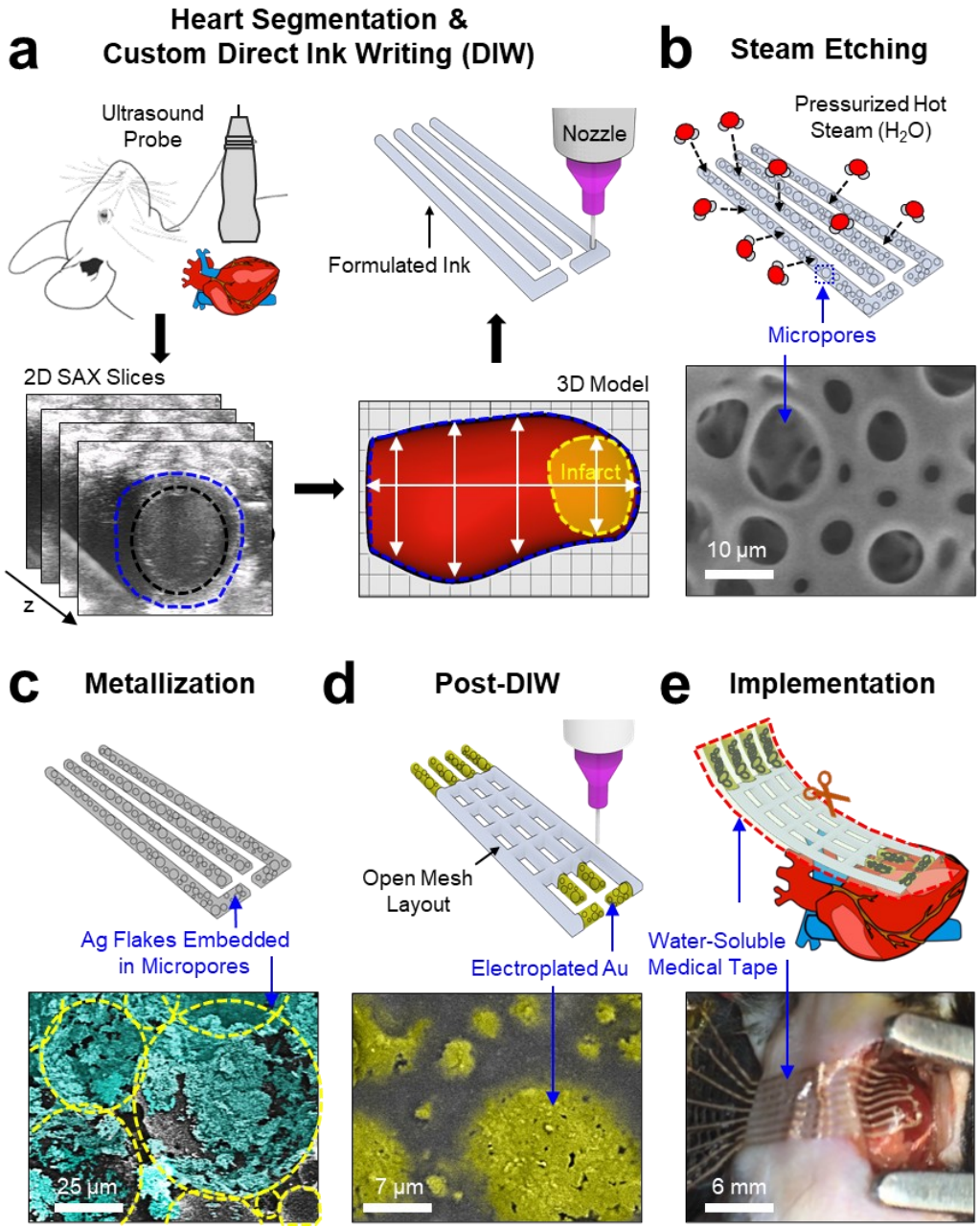

Figure 5.1. Schematic illustrations and optical images for the key process steps: (a) 3D imaging and custom direct ink writing (DIW), (b) steam etching, (c) metallization, (d) post-DIW, and (e) implementation on the epicardial surface of a murine heart.

Herein, the formulated ink, as described in more detail later, contains an optimal mixture of silicone resins and silica particles to provide both high-precision printability and the capability of turning the ink into a sponge-like foam. As presented in Figure 4.1b, the selectively patterned traces of the as-printed (i.e., prepolymer) ink were polymerized into an amorphous sponge-like morphology with a pore diameter ranging from 5 to 50 μm under a pressurized hot steam condition of 120 °C and 15 psi using a pressure rice cooker (Max, Instant Pot, Inc). Figure 4.2 shows representative results of the differential scanning calorimetry (DSC) of the ink to confirm its amorphous character. The formation of the micropores under this condition is likely attributed to the massive penetration and evaporation of the pressurized water molecules to/from the prepolymer.(Jeong et al., 2012) The resulting sponge-like foam was then immersed in a mixture solution of hexane (200 ml) and Ag flakes (0.5 mg; 200 nm-5 μm in diameter; Inframat Advanced Materials, LLC), allowing it to absorb the hexane quickly by capillary action in a manner that traps the Ag flakes into the internal pores (Figure 4.1c). The Ag flakes were then plated with Cu for 30 minutes to secure their mechanical and electrical interconnections. The resulting sheet resistance and stretchability were lower than $7.72 \pm 1.52\ \Omega \cdot sq^{-1}$ and greater than 100%, respectively (Figure 4.2b). Here, the Cu-plated Ag flakes were alternatively used as substitutes to expensive Au products, while their entire surface was plated with Au for 2 minutes to promote biocompatibility.(Vafaiee, Vossoughi, Mohammadpour, & Sasanpour, 2019) Next, another direct writing of the formulated ink was followed to define the remaining traces of the device in an open mesh layout to ensure breathability and stretchability (Figure 4.1d). (D.-H. Kim et al., 2010) Finally, a water-soluble medical tape made of polyvinyl alcohol (PVA, Sigma-Aldrich; 50 μm-thick) was applied to gently peel the device from the Si wafer and then trimmed to remove excess areas using scissors (Figure 4.1e). The water-soluble medical tape was used as a temporary supporting layer to facilitate its easy integration across the surface of the heart under median sternotomy, which thereafter was dissolved within no more than 30 seconds by applying a warm saline solution. Figure 4.3a presents a series of images for the complete dissolution of the water-soluble medical tape in 10 seconds when inserted into a warm water bath (35 ºC). Figure 4.3b provides the corresponding results of computational analysis, revealing that the total bending stiffness (or flexural rigidity) of the device decreased exponentially as the supporting layer (i.e., water-soluble medical tape) was dissolved over time due to its cubic dependence on thickness. (D.-H. Kim et al., 2010)

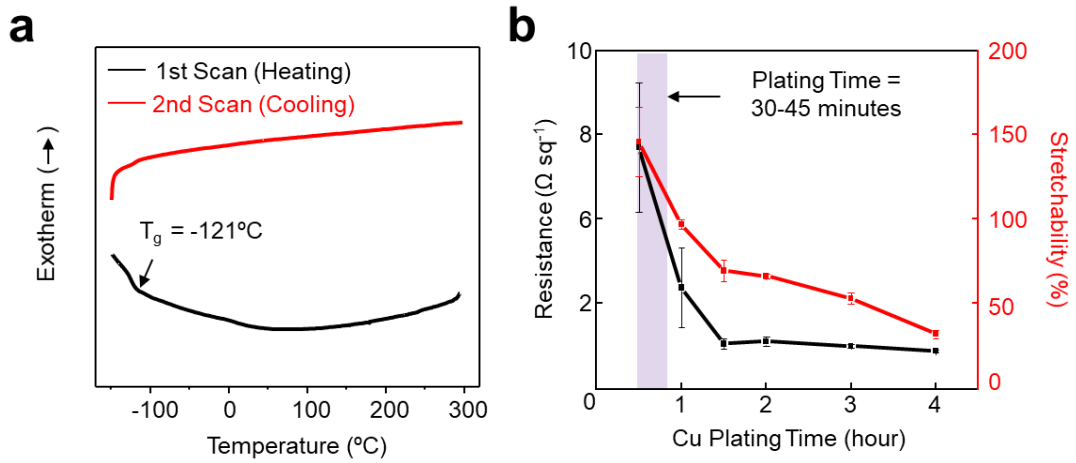

Figure 5.2. (a) Results of differential scanning calorimetry (DSC) for the sponge-like foam. (b) Change in the resistance and stretchability of the custom-printed sensor array with respect to the plating time of Cu.

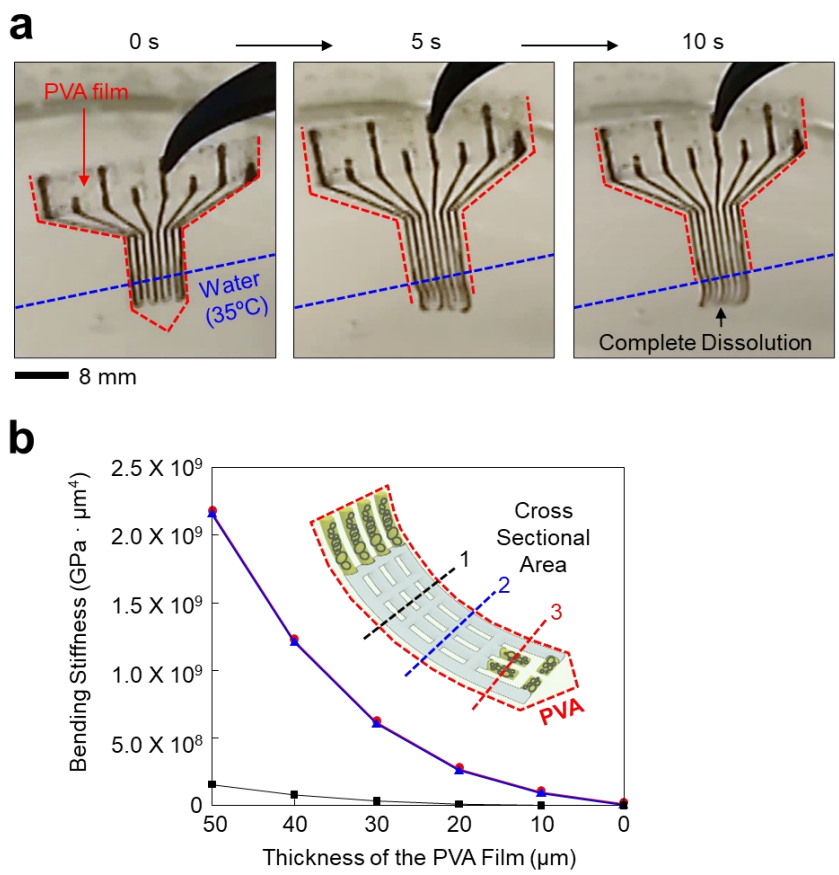

Figure 5.3. (a) Photographs of the custom-printed sensor array immersed in a warm water bath (35°C) for 10 seconds. (b) Results of the bending stiffness of the custom-printed sensor array with respect to the thickness of the water-soluble medical tape.

5.3 Material structure-property relationships

The rheological properties of the formulated ink are key parameters governing the printability and structural integrity of the printed device.(Daalkhaijav et al., 2018) To achieve the optimal rheological properties, we formulated the ink by blending (1) a base resin comprised of vinyl terminated diphenylsiloxane-dimethyl silicone copolymer, methylhydrosiloxane copolymer, and siloxane monomer with the weight ratio of 6.5:3.3:0.2, (2) a dilute resin (Sylgard 184, Dow Corning; 10:1 weight ratio of base and curing agents), and (3) a physical cross-linker of polysiloxane-treated hydrophobic silica (SiO_2-PS) particles (CAB-O-SIL® fumed silica TS-720, CABOT Corp). To predict the miscibility of the blended inks, we first conducted molecular dynamics (MD) simulations and quantitatively evaluated the interfacial interaction energy between the physical cross-linker (i.e., SiO_2-PS particles) and the surrounding resins. Figure 4.4 shows a representative snapshot image of the MD simulation for a SiO_2-PS particle, compared to a non-treated (hydroxyl-terminated) silica (SiO_2-OH) particle as a control. Details of the MD simulation results are summarized in Table 4.2. The results show that the interaction energy of the SiO_2-PS particle (-1.852 × 1021 kcal·mol^{-1}·g^{-1}) remained substantially lower than the control SiO_2-OH particle (-6.969 × 1021 kcal·mol-^{1}·g^{-1}), implying that the SiO_2-PS particle provides enhanced miscibility with the surrounding resins to better serve as a tractable modifier for the rheological properties of the ink.(Lewis, 2006)

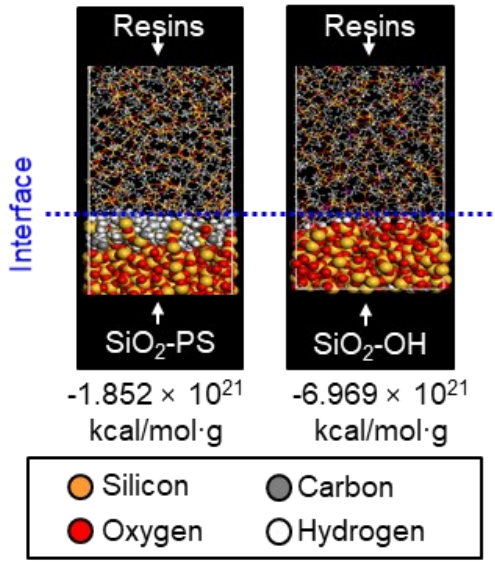

Figure 5.4. Snapshot image of the MD simulation for the interfacial interaction energy of a SiO2-PS particle (left panel) and a SiO2-OH particle (right panel) with the surrounding resins.

Table 5.2. Printing methods in terms of the working principles, printable materials, and key advantages and challenges.

Silica Type	Surface Property	Interaction Energy (kcal/mol)			Interaction Energy Per Area (kcal/mol Å^2)	Interaction Energy Per Silica Weight (kcal/mol g-silica)
		Total Energy	Van der Waals Energy	Electrostatic Energy		
SiO_2-PS	Superhydrophobic	-119.1	-118.8	-0.3	-0.1610	-1.852 x10^{21}
SiO_2-OH	Hydrophilic	-160.4	-149.3	-8.0	-0.2144	-6.969 x10^{21}

To characterize rheological properties, we prepared variously blended inks by varying the weight ratio of the base resin, dilute resin, and SiO_2-PS particles from 5.7:3.3:1.0 to 6.0:3.3:0.7, 4.2:5.0:0.8, and 4.5:5.0:0.5, compared to commercial control groups of a dispensable silicone ink (SE 1700, Dow Corning) and a bare PDMS ink (Sylgard 184, Dow Corning). Figure 4.5 presents the measurement results for the storage (G'; lines) and loss (G"; dotted lines) modulus of these blends. The inks with 5.7:3.3:1.0, 6.0:3.3:0.7, and 4.2:5.0:0.8 ratios and the SE 1700 ink exhibited a gel-like viscoelastic behavior (i.e., G' > G") within the linear viscoelastic (LVE) region (plateau regions) that indicates a printable range without distorting the structural integrity. For example, Figure 4.6 provides a set of optical images for various as-printed (prepolymer) structures with the minimum linewidth and spacing of 200 µm and 300 µm, respectively. On the other hand, the ink with a 4.5:5.0:0.5 ratio and the Sylgard 184 ink exhibited a liquid-like viscoelastic behavior due to their dominating G" at all shear stresses, which thereby precludes their use for dispensing through a nozzle. The inks exhibited the shear-thinning behavior in which their viscosity decreased with an increase of the shear rate, whereas the Sylgard 184 ink exhibited a zero-shear-rate behavior (plateau curve) at all shear rates (Figure 4.7). The purple-highlighted area in the graph indicates a range of viscosity where the high-fidelity formation of micropores (i.e., sponge-like foam) occurred under the hot pressurized steam condition. The results also show that the ink with a 6.0:3.3:0.7 ratio remained within this range at low shear rates. As shown in Figure 4.8, this ink also substantially extended the working lifetime (i.e., the time to reach the crossover between G' and G") up to 34 hours, as compared to the SE 1700 ink (2 hours) and the Sylgard 184 ink (8 hours). This substantially prolonged working lifetime is essential not only to maintain the structural integrity of the as-printed (i.e., prepolymer) ink prior to complete polymerization,(Ozbolat et al., 2018) but also to provide sufficient time for the micropores to form

across the entire thickness of the structure up to 150 µm (Figure 4.9). For comparison, Figure 4.10 presents experimental results showing that the formulated ink was completely polymerized after 15 minutes of annealing at 160 °C (i.e., the plateau curve of G'), whereas the ink mixed with conductive nanofillers (i.e., Ag flakes) remained unpolymerized even after 1 hour of annealing at the same condition. In conclusion, the ink with a 6.0:3.3:0.7 ratio meets all requirements of both the appropriate shear-thinning flow behavior and the prolonged working lifetime, allowing for rapid custom prototyping of the sponge-like poroelastic foam.

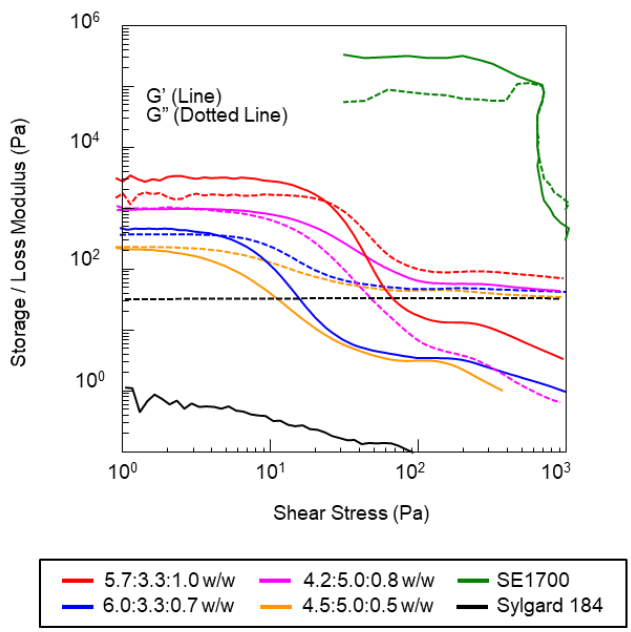

Figure 5.5. Storage and loss modulus of the inks with respect to shear stress.

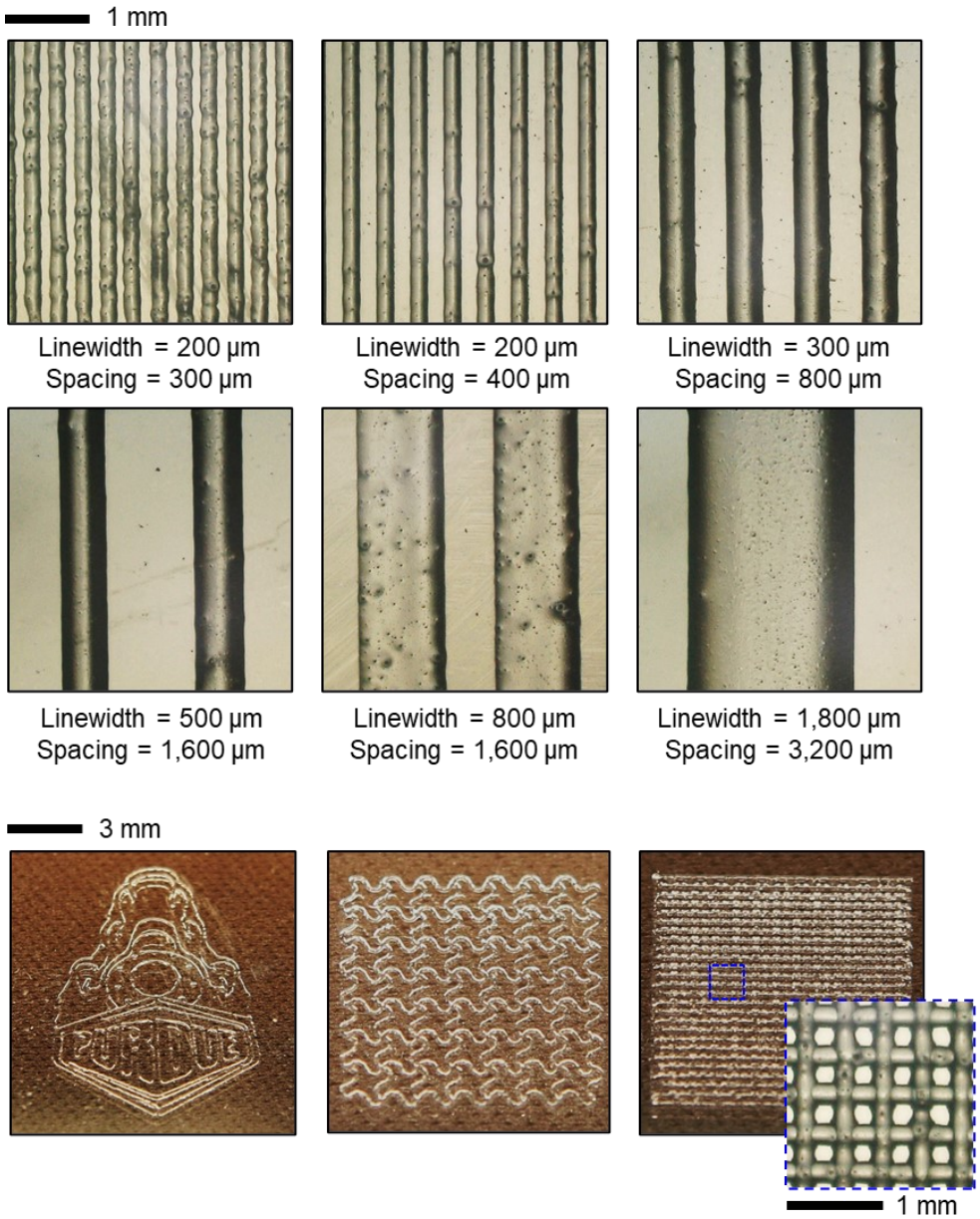

Figure 5.6. Photographs of various as-printed structures using the formulated ink with the weight ratio of 6.0:3.3:0.7.

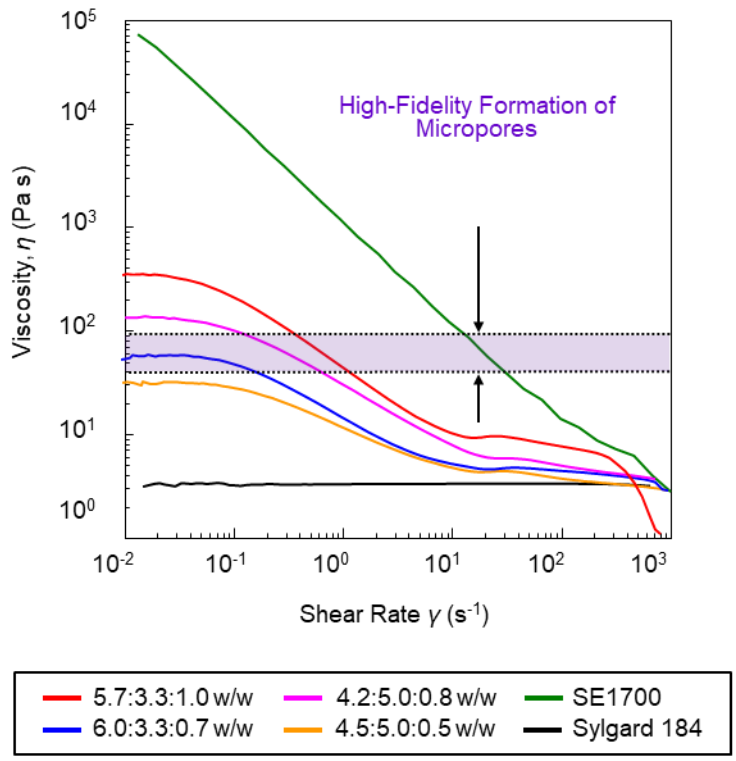

Figure 5.7. Viscosity of the inks with respect to shear rate.

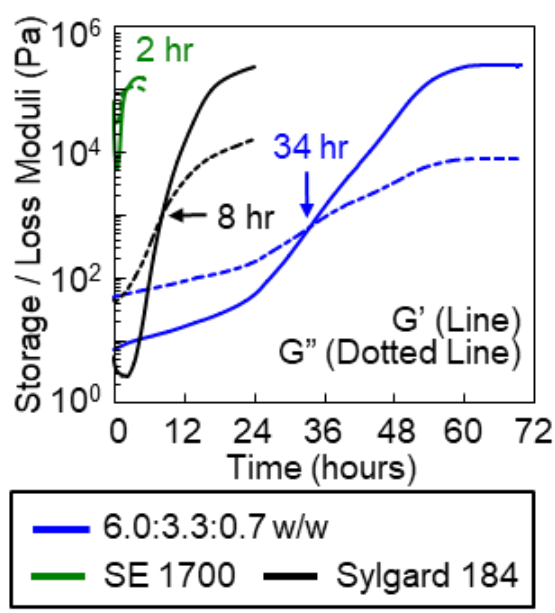

Figure 5.8. Change in the storage and loss modulus of the inks over time.

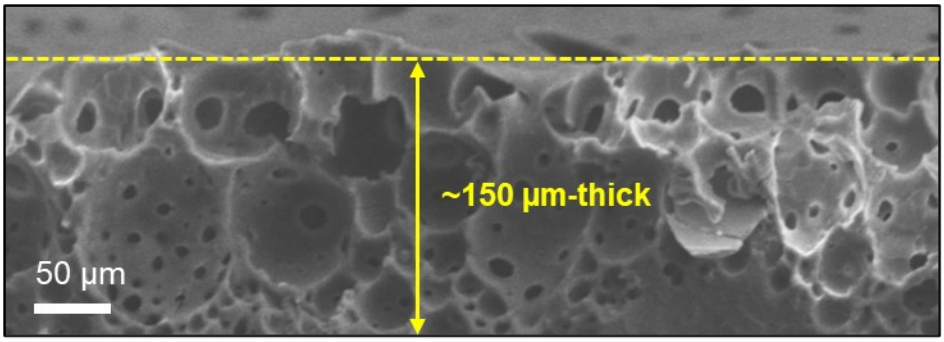

Figure 5.9. Cross-sectional side view of an SEM image for the sponge-like foam.

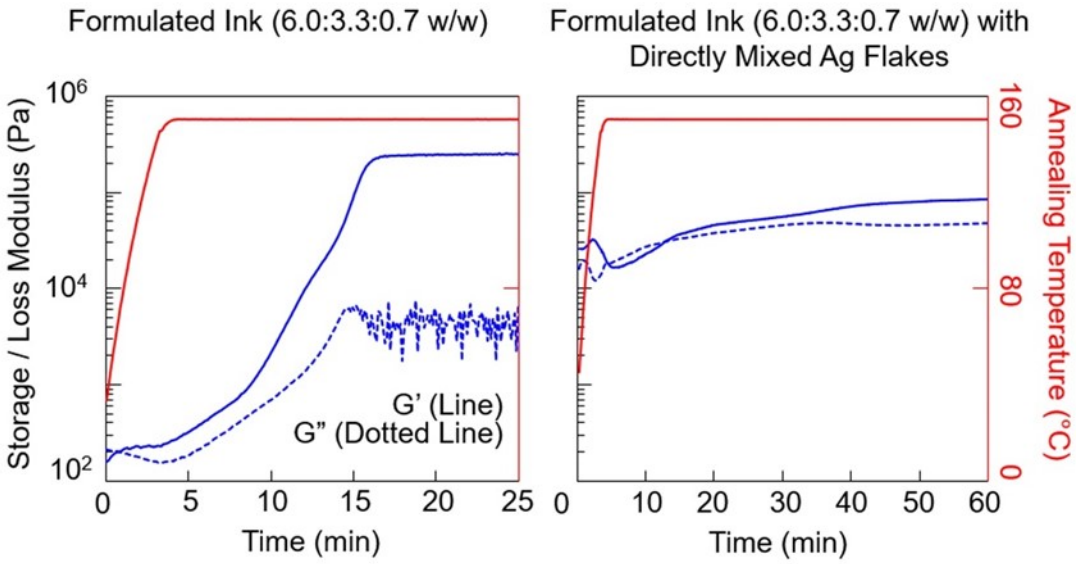

Figure 5.10. Change in the storage and loss modulus of the formulated ink with the weight ratio of 6.0:3.3:0.7 (left panel) and the ink with directly mixed Ag flakes (right panel) over time.

Figure 4.11 shows the stress-strain curve for a printed line (2 cm-long × 2 mm-wide × 150 μm-thick) made of the ink with 6.0:3.3:0.7 ratio before (blue line) and after (red line) the formation of micropores, compared to control groups made of the SE 1700 ink (green line) and the Sylgard 184 ink (black line). The mechanical modulus of the printed line decreased more than 3-fold (E = 0.15 ± 0.02 MPa) in the presence of micropores due to their large volumetric porosity (~70%), which remained substantially lower than the control groups (> 1.11 MPa) by nearly or more than 10-fold. The inset graph presents the corresponding results obtained from this ink configured into an open mesh layout (8 mm × 20 mm), providing an ultralow effective mechanical modulus (E = 29 ± 12 kPa) that is comparable to that of human cardiac tissues (E = 29-41 kPa). (J. Park et al., 2016) These results imply that the printed device is capable of gently interfacing across the epicardial surface in a way that imposes minimal stress on the tissue. Figure 4.12 and 4.13 summarize the mechanical hysteresis and the corresponding energy loss of the printed device under repetitive loading-unloading cycles (> 5 times each) at a strain (ε) of 50%, respectively. The results show that the printed device exhibited substantially suppressed mechanical hysteresis with the lowest energy loss of 4.3 ± 0.5 $kJ \cdot m^{-4}$; a value that was substantially lower than the control group made of the SE 1700 ink (23.6 ± 8.7 $kJ \cdot m^{-4}$) by more than 5-fold. This energy loss gap increased proportionally to the strain (Figure 4.14). Figure 4.15 shows that the electrical hysteresis of the printed device remained substantially low between 0.006 and 0.192 with a strain of up to 30% that corresponds to the maximum strain of the human heart,(S. Choi et al., 2018) which is also at least 10-fold lower than similar counterparts reported previously.(Costa, Ribeiro, & Lanceros-Mendez, 2015; A. D. Valentine et al., 2017) The printed device was stretched up to nearly 150% prior to its fracture while maintaining its resistance (R/R0) below 9.0 (Figure 4.16). Figure 4.17 confirms that the resistance remained constant below 5.0 throughout multiple loading-unloading cycles (> 1,000 times) with a strain of up to 30%. Throughout these tests, no evidence of the delamination or leakage of the embedded conductive nanofillers (i.e., Ag flakes) was observed. Moreover, the sheet resistance of the printed device remained nearly unchanged within a range of variation (0.5–2.5 Ω·sq-1) when soaked in a bath of distilled (DI) water, phosphate-buffered saline (PBS), and ethanol for 12 hours (Figure 4.18).

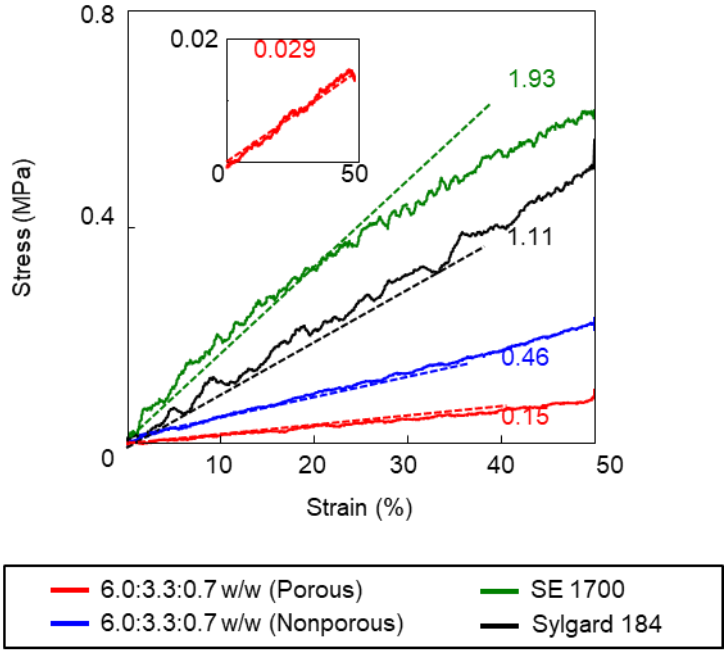

Figure 5.11. Stress-strain curves of the inks. Inset graph shows the corresponding results obtained from the ink with 6.0:3.3:0.7 ratio configured into an open mesh layout.

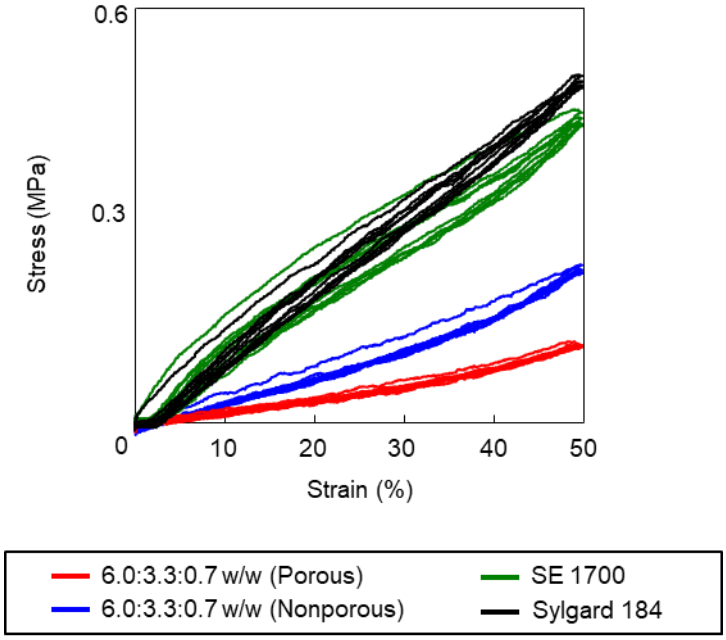

Figure 5.12. Mechanical hysteresis of the inks for 5 loading-unloading cycles at a strain of 50%.

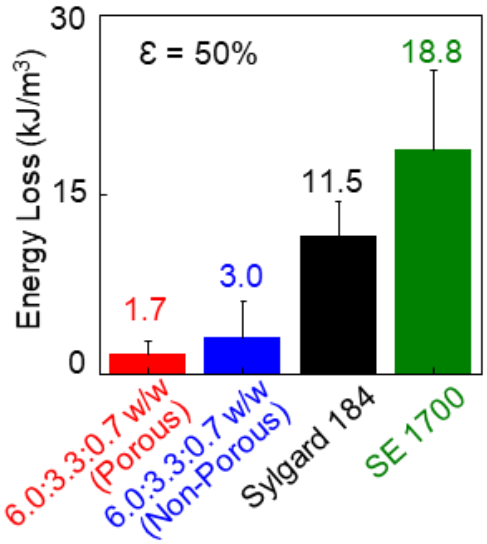

Figure 5.13. Energy loss of the inks.

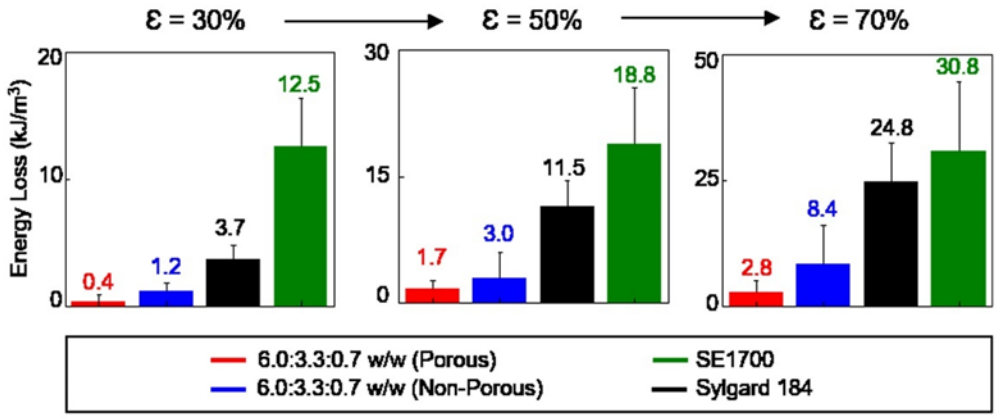

Figure 5.14. Change in the energy loss of the custom-printed sensor array with respect to a strain ranging from 30% to 70%.

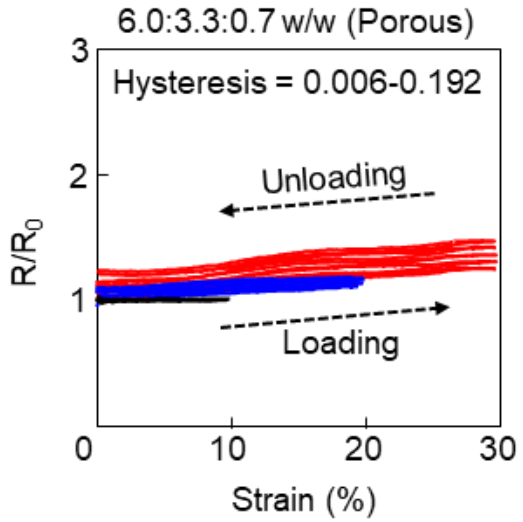

Figure 5.15. Electrical hysteresis of the inks with respect to the strain from 10% to 50%.

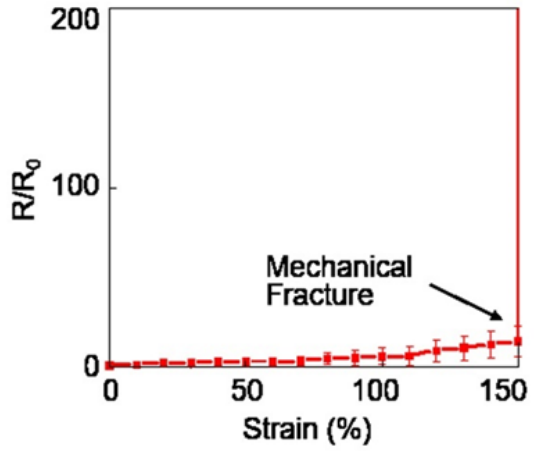

Figure 5.16. Change in the resistance of the custom-printed sensor array with respect to the strain up to 150%.

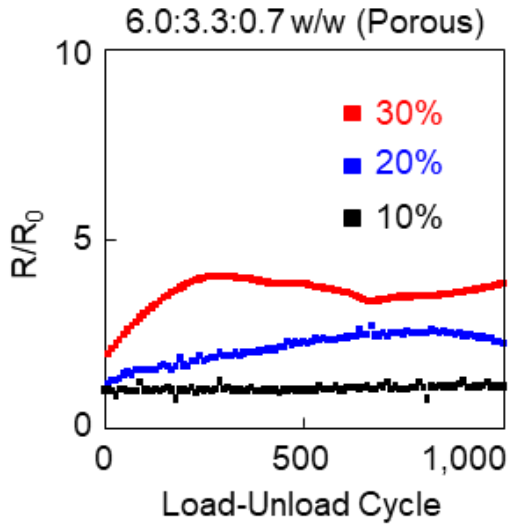

Figure 5.17. Change in the resistance of the inks throughout 1,000 times of loading-unloading cycles with the strains ranging from 10% to 30%.

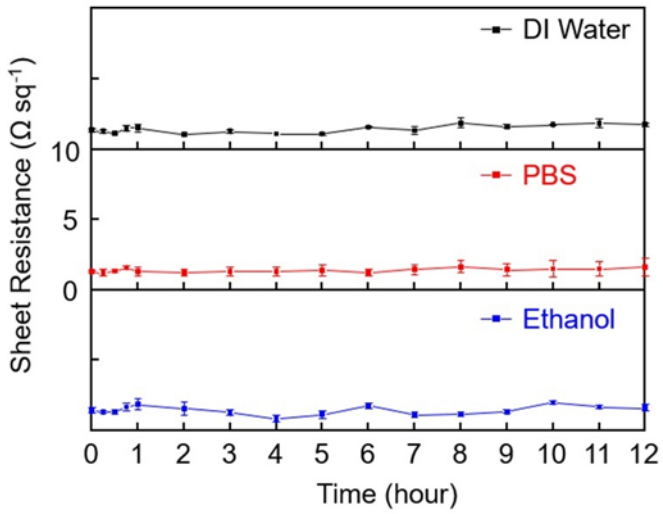

Figure 5.18. Change in the sheet resistance of the devices soaked in a bath of DI water (top panel), PBS (middle panel), and ethanol (bottom panel) for 12 hours.

5.4 Rapid custom prototyping

The well-regulated rheological and mechanical properties of the formulated ink drove the exploration for the rapid prototyping of a custom-designed poroelastic biosensor, in a few hours per batch of a dozen, that provides a tailored geometry to cover a wide range of heart sizes and shapes. Figure 4.19 displays photographs of custom-printed devices, each of which was customized to fit with the enucleated piglet, ovine, porcine, and bovine hearts from the upper left to bottom right clockwise. Figure 4.20 schematically illustrates the cross-sectional view of the hearts to compare their sizes. All these devices were able to accommodate the different sizes and shapes of the hearts at various length scales, while simultaneously forming a seamless contact to the irregular epicardial surfaces due to their substantially low bending stiffness ($< 8.0 \times 10^7$ GPa·μm^4). Here, the spatial resolution of these devices (i.e., the number of electrodes within a given region) was determined by the feature resolution of the nozzle injection system (i.e., the minimum nozzle size of about 100 μm). For instance, a total of 64 electrodes (i.e., 32 recording channels) on the device were uniformly distributed across the entire surface of the enucleated porcine heart that is similar in size to the human heart.(Lelovas, Kostomitsopoulos, & Xanthos, 2014)

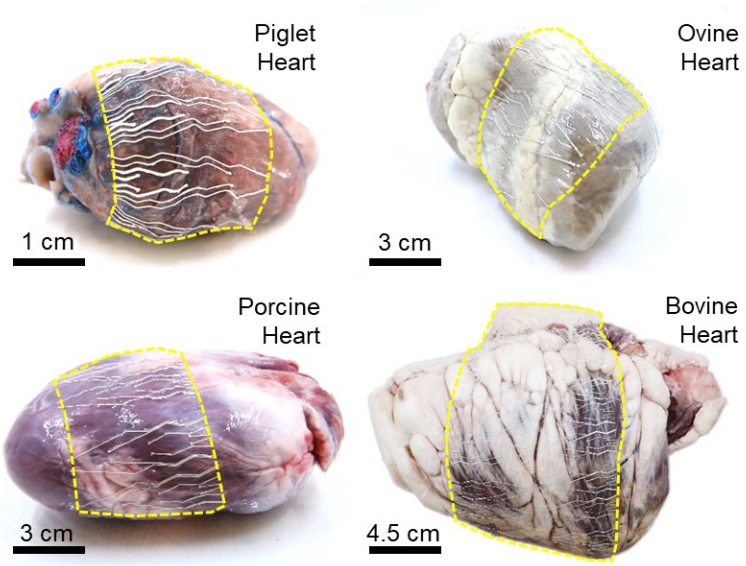

Figure 5.19. Photographs of the custom-printed sensor arrays, each of which was customized to fit with the enucleated piglet, ovine, porcine, and bovine hearts from upper left to bottom right clockwise.

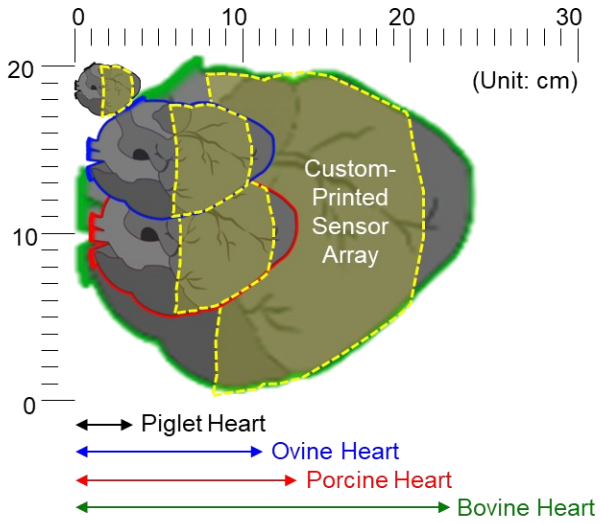

Figure 5.20. Schematic illustration of the cross-sectional view of the hearts.

The poroelastic nature and the open mesh layout of these devices also ensured minimal normal (peeling) stress to the epicardium tissue (i.e., the minimum adhesion energy per unit area ≈ 0.5 mJ·m-^{2}) and thereby induced a strong capillary adhesion at the interface. (D.-H. Kim et al., 2010) This aspect allowed the devices to reliably adhere onto the epicardial surface without slipping and be also detached without significant mechanical impact on the epicardium tissue. Figure 4.21 presents representative epicardial ECG signals obtained from the enucleated porcine heart by applying an artificial ECG waveform (frequency = 1 Hz; amplitude = 20 mV) using a signal generator (Keithley 3390). The results showed that the measured ECG signals were followed consistently by those generated from the signal generator, confirming that all 64 electrodes seamlessly interfaced with the epicardial surface. These observations were consistent when the device was integrated with other organs, such as the enucleated porcine liver (Figure 4.22a). Notably, the quality of the conformal coverage was maintained even when the device was interfaced with the deeply wrinkled surface of a human brain model (Figure 4.22b).

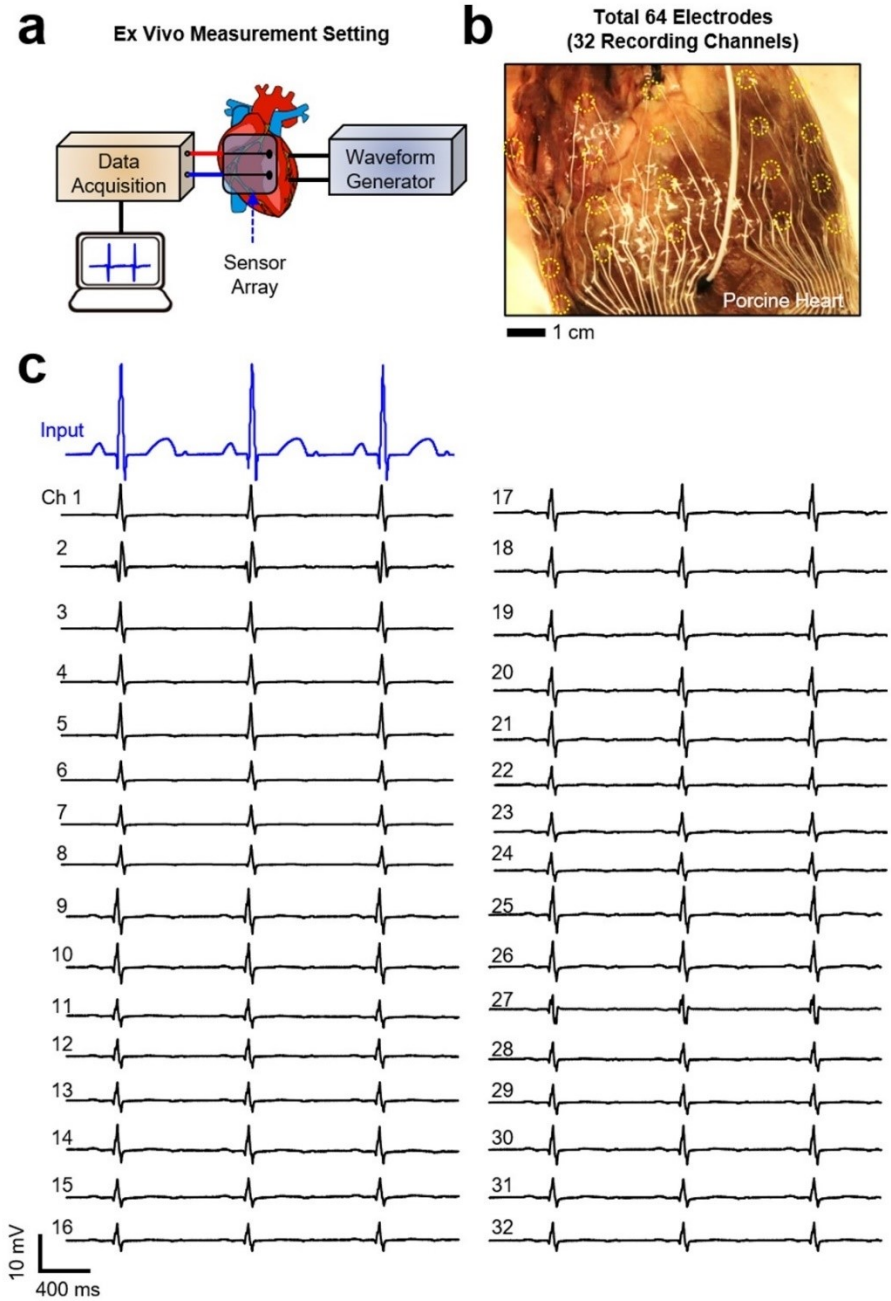

Figure 5.21. (a) Schematic illustration of an experiment setup for the ex vivo measurement of epicardial ECG signals from the enucleated porcine heart. (b) Photograph of the device (total 64 electrodes) placed on the surface of the enucleated porcine heart. (c) Measurement results of the epicardial ECG signals by applying an artificial ECG waveform.

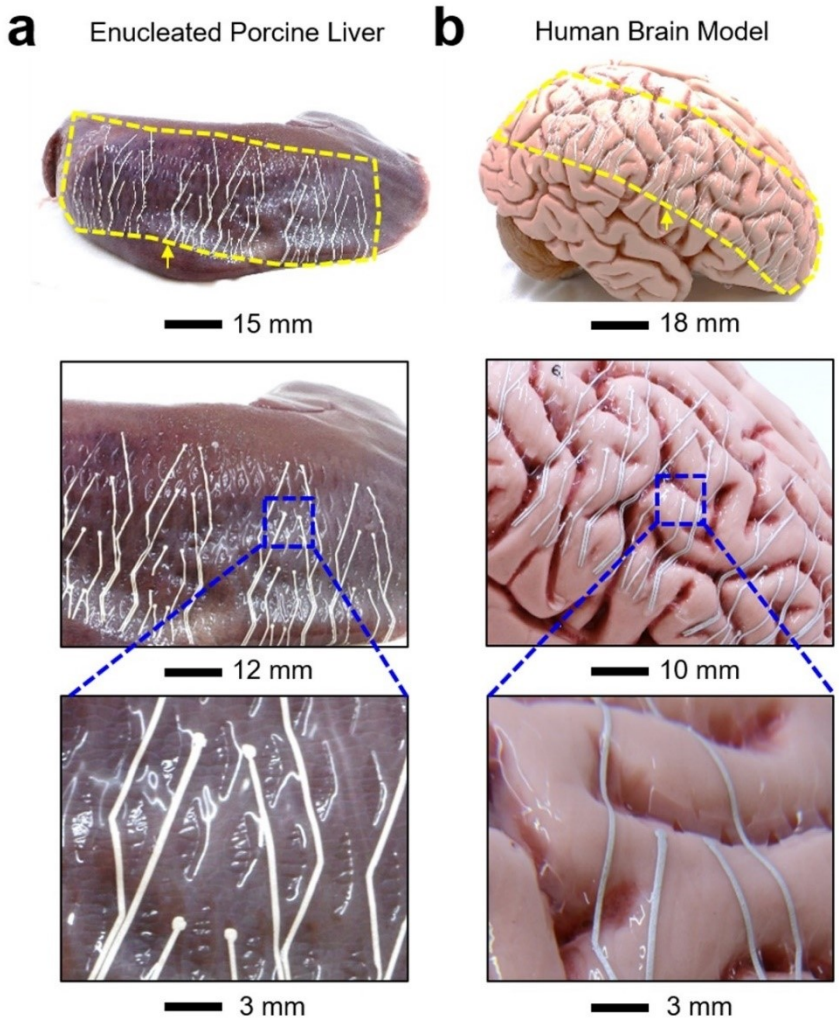

Figure 5.22. Photographs of the devices placed on the surface of (a) the enucleated porcine liver and (b) a human brain model.

5.5 Spatiotemporal recording of epicardial electrocardiogram *in vivo*

We evaluated the ability of the custom-printed devices in a spatiotemporal recording of epicardial electrocardiogram (ECG) in healthy murine (n = 5) and porcine hearts (n = 2) *in vivo*. The porcine heart provides a substantial similarity in size and shape to the human heart.(Lelovas et al., 2014) The devices were placed on the left ventricle after median sternotomy using a water-soluble medical tape (i.e., PVA). Following the dissolution of the tape with the application of a warm saline solution, the devices (~50 μm-thick) adhered intimately to the epicardial surface by capillary adhesion force (Figure 4.23). Here, the devices were configured with a total of 4 and 6 pairs of recording electrodes to cover the total areas of 1.25 cm^2 and 50 cm^2 for the acquisition of murine and porcine ECG signals, respectively. The electrochemical impedance of the individual electrodes (200 μm × 200 μm) was characterized in a phosphate-buffered saline (PBS) solution with a pH of 7.2 at 23 °C as 2.1, 1.5, and 1.0 kΩ at frequencies of 40, 150, and 1,000 Hz, respectively (Figure 4.24). The remarkably low impedances were attributed to the poroelastic properties of the devices that provide not only large interfacial areas between electrodes and electrolytes but also rapid solid-state diffusion of charge carriers.(Jo, Park, Jeong, Lee, & Lee, 2015)

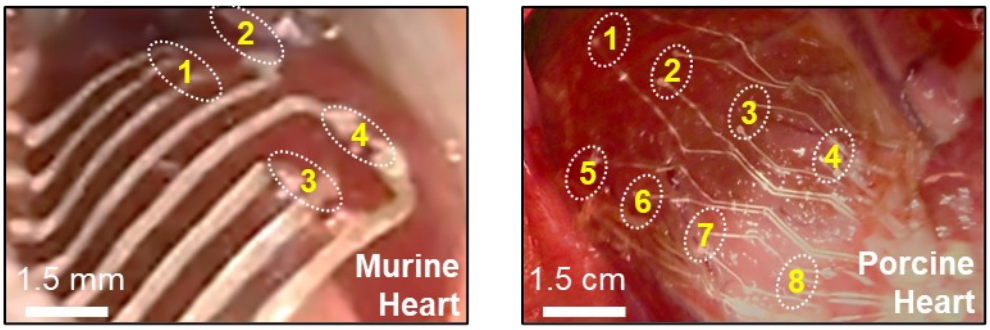

Figure 5.23. Photographs of the custom-printed sensor arrays placed on the epicardial surface of a murine (left panel) and porcine heart (right panel).

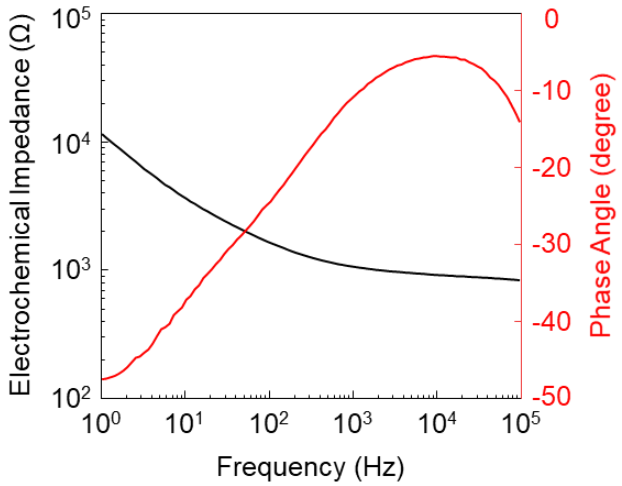

Figure 5.24. Electrochemical impedance of the device soaked in a bath of PBS as a function of frequency.

The exceptionally soft and thin nature of the devices enabled them to maintain a highly conformal contact to the epicardial surface under normal cardiac cycles with the murine and porcine heart rates of 529.9 ± 9.3 and 85.4 ± 8.5 beats per minute, respectively. The degree of conformal coverage across the epicardial surface increased with the decreased thickness of the device from 300 μm to 50 μm due to the substantially reduced bending stiffness by more than 200-fold (Figure 4.25). Figure 4.26 shows the corresponding measurement results for the post-processed 3D data of spatiotemporally recorded murine (left panel) and porcine (right panel) ECG signals. The raw data of the epicardial ECG signals obtained from all healthy murine and porcine hearts are summarized in Figure 4.27, displaying a typical ECG tracing of the cardiac cycle that consists of a P-wave (atrial depolarization), a QRS-complex (ventricular depolarization), and a T-wave (ventricular repolarization). The corresponding quantitative data of R-R interval, QRS duration, and J-point elevation are included in Figure 4.28, confirming that no J-segment elevation was observed in ECG recordings from the healthy hearts. The strain-insensitive poroelastic behavior (i.e., the negligible electrical hysteresis under cyclic loading with a strain of < 30%) of the devices and their robust conformal contact across the beating epicardial surface enabled the high-fidelity acquisition of epicardial ECG signals without noticeable degradation in signal quality over time (Figure 4.29, top panel). For comparison, Figure 4.29 (bottom panel) presents the results of the control measurements simultaneously obtained from a 3-lead electrode set (ERT Control/Gating Module Model 1030, SA Instruments, Stony Brook, NY) that presents a state-of-

the-art *in vivo* sensing tool tailored for small animal applications. The results display the shift (i.e., elevation and depression) of the signal baseline caused by the inhalation and exhalation of breathing, respectively.(Sato et al., 2018)

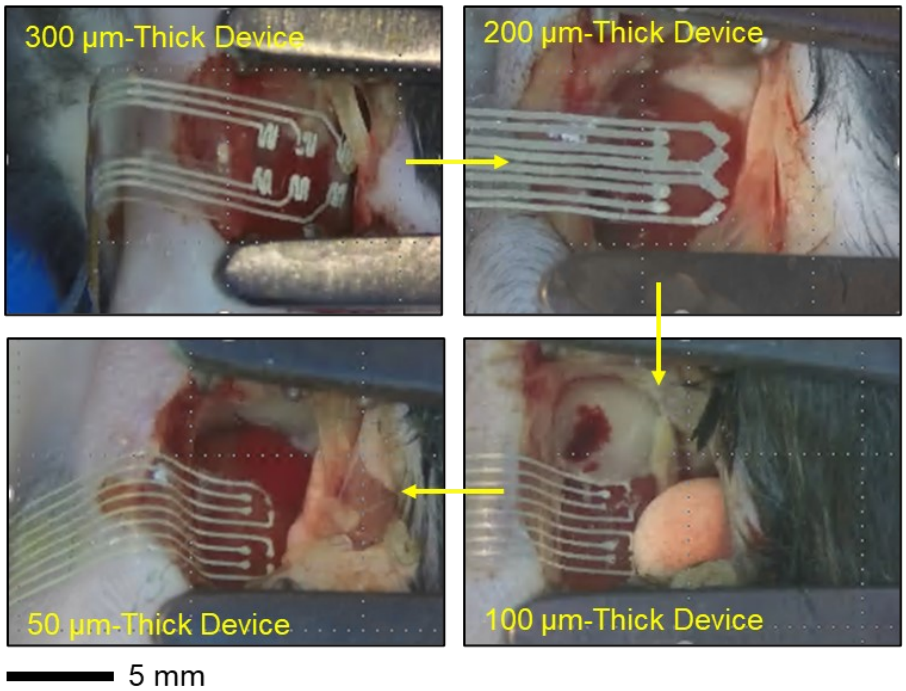

Figure 5.25. Photographs of the devices with different thicknesses ranging from 50 µm to 300 µm placed on the epicardial surface of a murine heart.

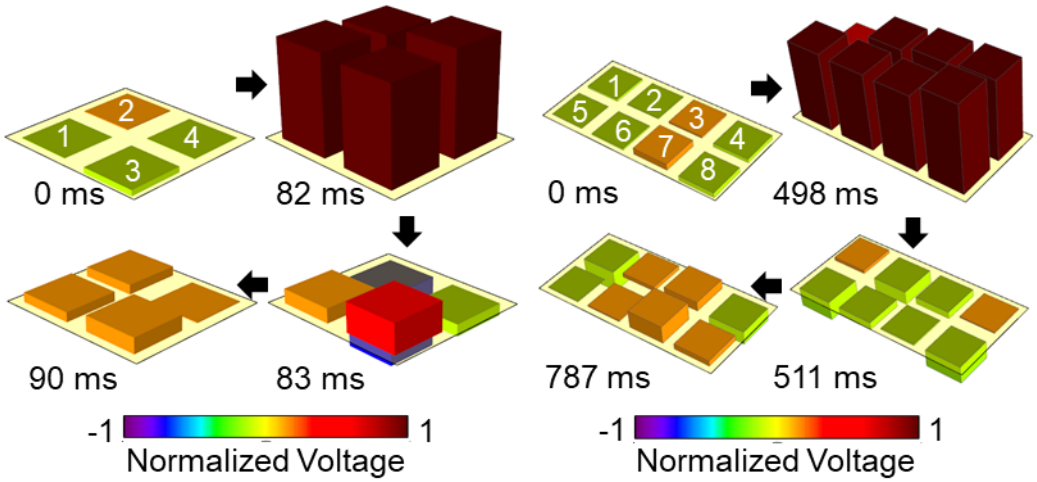

Figure 5.26. Post-processed 3D data of the spatiotemporally recorded murine (left panel) and porcine (right panel) ECG signals.

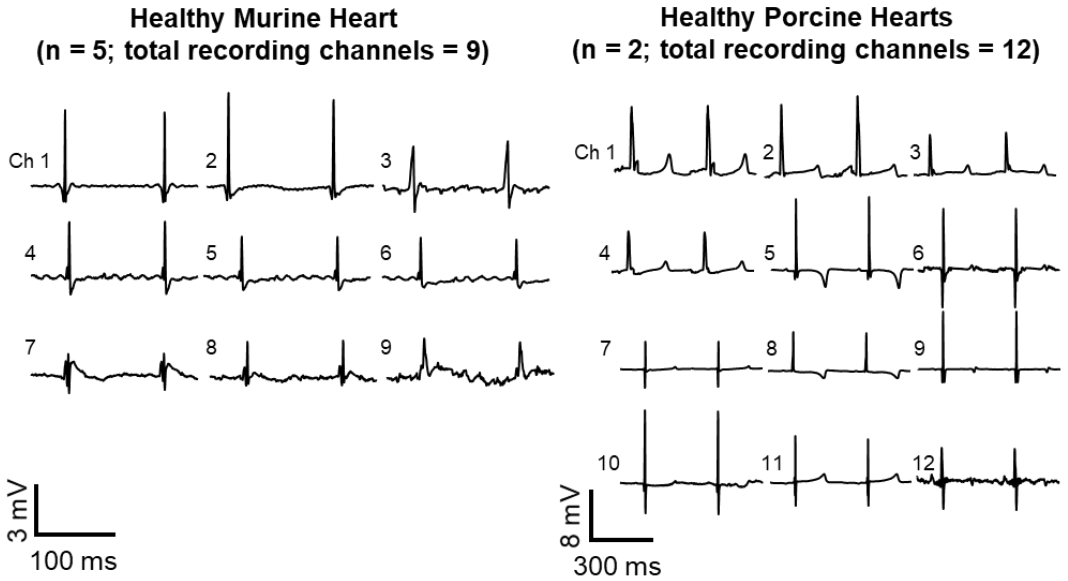

Figure 5.27. Epicardial ECG signals obtained from the healthy murine (n = 5) and porcine hearts (n = 2).

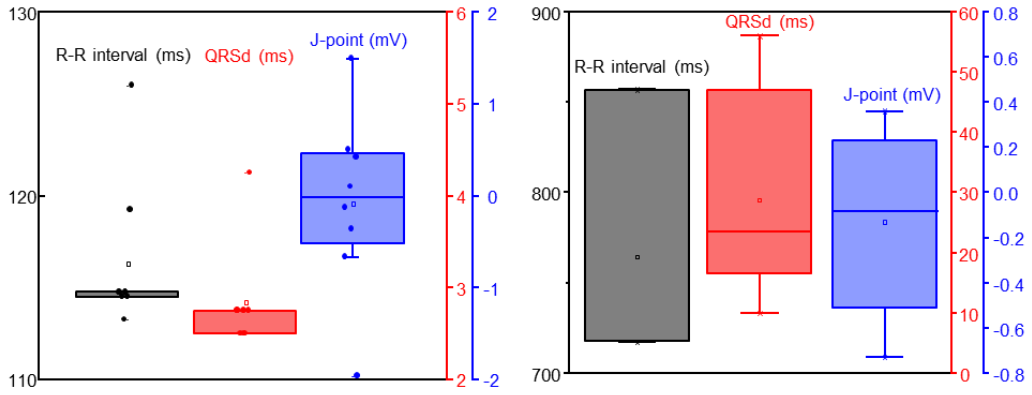

Figure 5.28. The corresponding quantitative data of R-R interval, QRS duration, and J-point elevation.

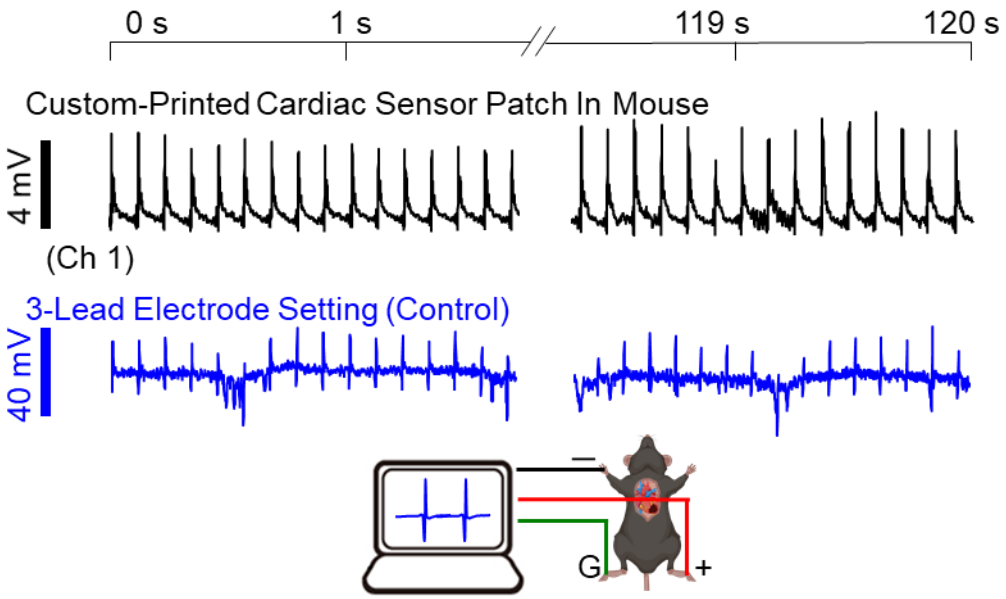

Figure 5.29. Simultaneously measured ECG signals using the custom-printed sensor array (top panel) and a control 3-lead electrode set (bottom panel) on a murine heart.

5.6 Intraoperative epicardial mapping in a murine myocardial infarction model

Intraoperative epicardial mapping is useful in localizing critical regions that indicate the origin of pathophysiological conditions such as arrhythmias after acute myocardial infarction, thereby providing important information to guide definitive surgical treatments, especially when the infarct border needs to be identified.(Cuculich et al., 2011; J. Liu et al., 2020) To demonstrate the utility of the custom-printed devices in this surgical setting, we performed the intraoperative spatiotemporal mapping of epicardial ECG signals in a murine acute myocardial infarction model *in vivo*. An adult mouse underwent left thoracotomy to expose the ventral portion of the heart, followed by the placement of a custom-printed sensor array (total 6 recording channels) on the epicardial surface to cover the entire ventricular epicardium (Figure 4.30). Surgery to permanently ligate the left coronary artery was performed following the same procedures as reported in previous studies.(Soepriatna et al., 2019) Representative results of the epicardial ECG measurements are shown in Figure 4.31. Following approximately 30 seconds of ligation, ST-segment elevation (red circles in the middle panel) occurred near the ligation point where the sensor channels 2 and 3 were located. After 60 seconds of ligation, the ST-segment elevation was also detected by the sensor channels 4-6, implying that the regional myocardial infarction propagated toward the apex of the heart with a velocity of approximately 0.6 mm·sec^{-1}. The ECG signals displayed a convex

ST-segment, indicating that the corresponding regions experienced ischemia or hypoxic conditions.(Deshpande & Birnbaum, 2014) All the ECG data obtained from the infarcted mice (n = 5; total 9 recording channels) and their corresponding quantitative data of R-R interval, QRS duration, and J-point elevation are summarized in Figure 4.32. The data exhibited the prolongation of QRS duration, the elevation of J-segment, the metrics of systolic dysfunction, and the elevation of ST-segment after about 40 seconds of ligation, showing statistical differences from those obtained before ligation using one-way ANOVA with Tukey's post hoc test with significance is set at $p < 0.05$. Figure 4.33 presents the results of control measurements obtained simultaneously using a 3-lead electrode set, displaying reciprocal ST-segment depression to confirm the occurrence of an ischemic event. The control measurements also displayed both reciprocal ST-segment depression and elevation within seconds of left coronary artery ligation (Figure 4.34), which typically occurs in the 3-lead electrode recording configuration.(Al-Salam & Hashmi, 2014; Arora & Mishra, 2020; Au - Scofield & Au - Singh, 2016; Preda & Burlacu, 2010) These ST-segment depression and elevation were consistently observed during the surgery and throughout the recording duration of 30 minutes after ligation (Figure 4.35). The results also imply that the devices maintained a robust and intimate coupling to the epicardial surface without changing position throughout the long-term recording period (30 minutes) that involved more than 10,000 individual beats.

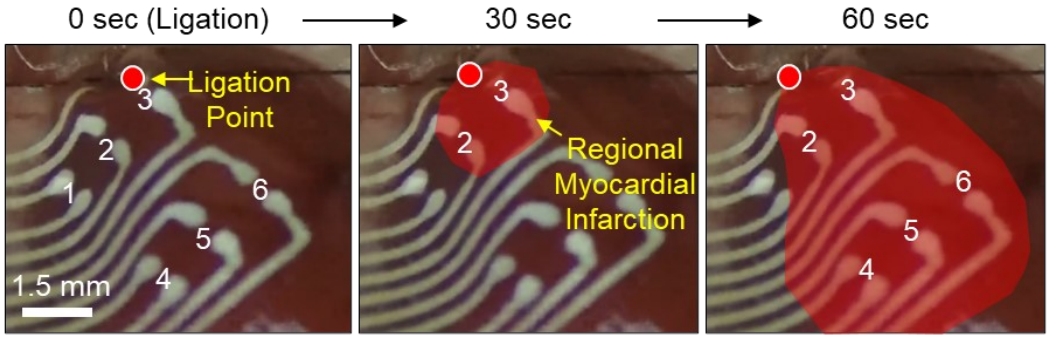

Figure 5.30. Enlarged images of the custom-printed sensor array covering the entire ventricular epicardium. The red highlighted area indicates the regional myocardial infarction propagating toward the apex of the murine heart over time.

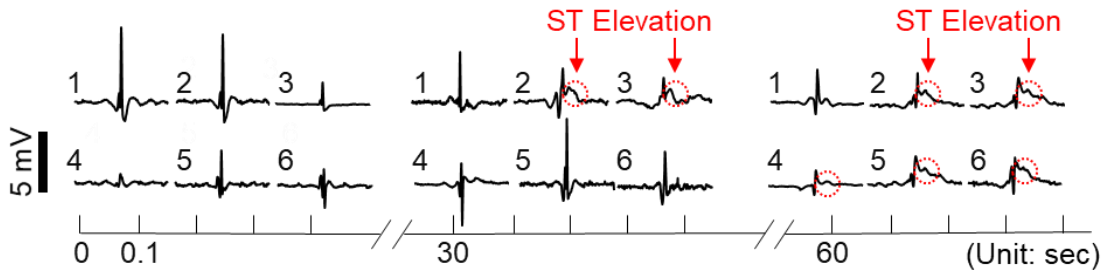

Figure 5.31. Measured epicardial ECG signals using the custom-printed sensor array.

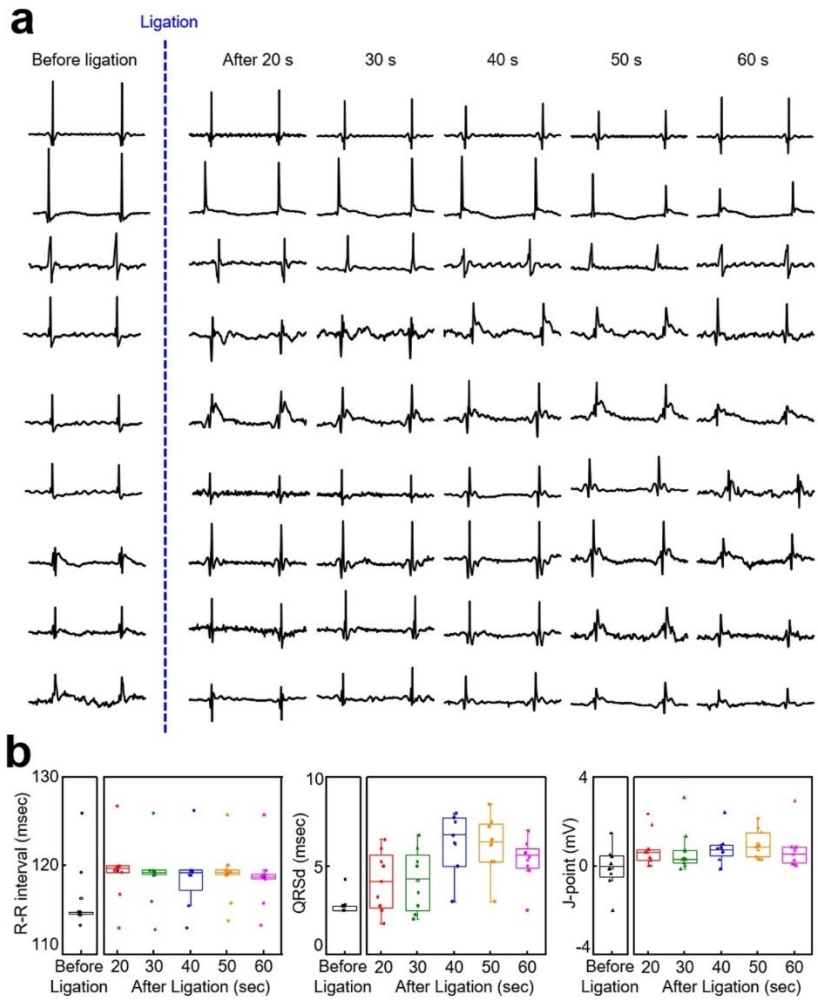

Figure 5.32. (a) Epicardial ECG signals obtained from a murine myocardial infarction model (n = 5). (b) The corresponding quantitative data of R-R interval (left panel), QRS duration (middle panel), and J-point elevation (right panel).

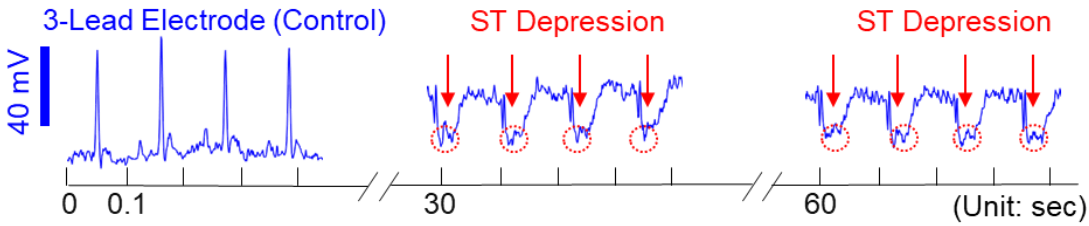

Figure 5.33. Simultaneously measured ECG signals using a control 3-lead electrode set.

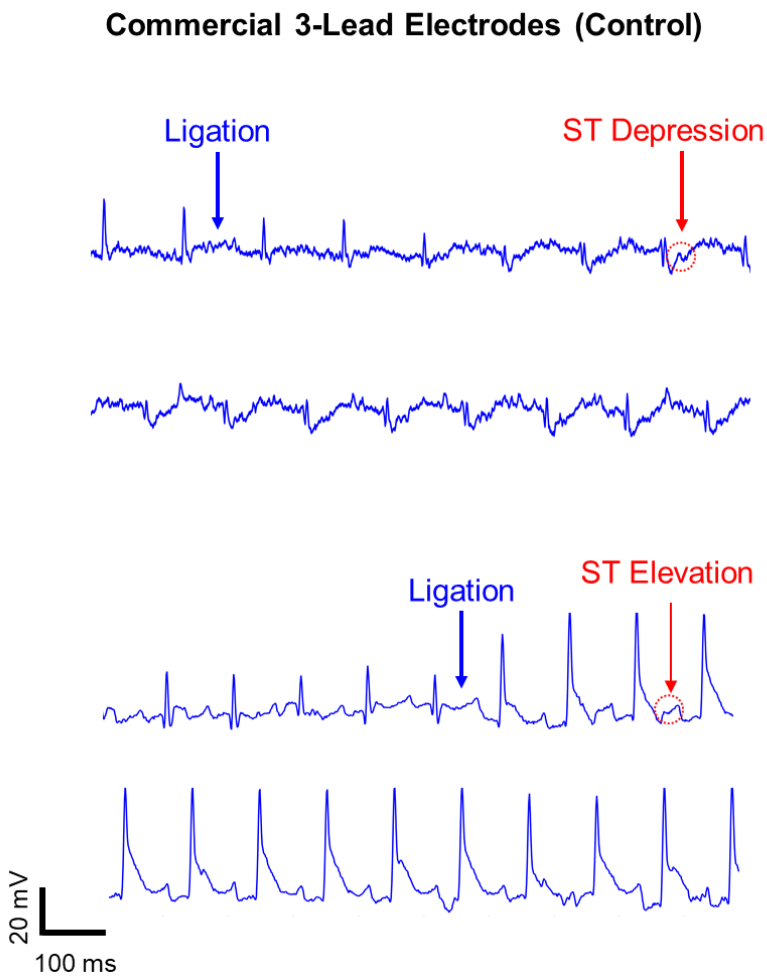

Figure 5.34. Representative global ECG data of ST-segment depression (top panel) and elevation (bottom panel) within seconds following left coronary artery ligation (blue arrows).

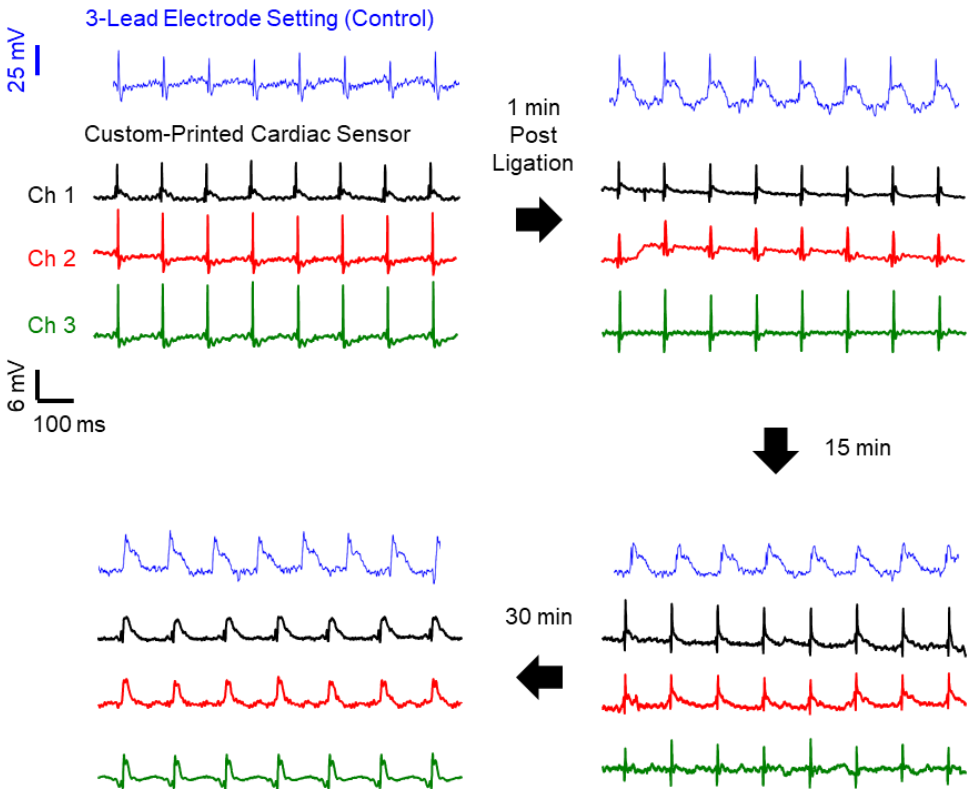

Figure 5.35. Representative ECG data with persistent ST-segment elevation at baseline and at 1, 15, and 30 minutes following left coronary artery ligation.

The semi-transparency of the devices, due to the open mesh layout and thin-film design (50 µm-thick), enabled simultaneous ultrasound mapping, as a means for validating the location and size of the myocardial infarction region in real time. (L. Xu et al., 2014) Figure 4.36 schematically illustrates an experimental setup that includes a high-frequency ultrasound system (Vevo3100, FUJIFILM VisualSonics Inc), with the enlarged photograph in Figure 4.37. A warmed ultrasound gel (Ultrasound Transmission Gel, Parker, Inc) was applied directly to the device placed on the left ventricle of the heart. Figure 4.38 shows a representative short-axis ultrasound image, clearly visualizing the device (yellow circle) along with the epicardium (blue circle) and endocardium (red circle) of the heart. The results show that QRS-complex appeared at the initiation of the left ventricle contraction while P-wave prior to the QRS-complex corresponded to the atrial kick responsible for pushing residual blood from the left atrium to the left ventricle (i.e., the phase of diastolic left ventricular filling). The overall quality of both the ultrasound images and the simultaneously recorded ECG signals were unaffected by motion artifacts (e.g., the heartbeat and respiration) through the robust conformal coupling to the epicardial surface. For comparison,

Figure 4.39 provides the ultrasound images of both relatively thick (200 µm-thick; top panel) and thin (50 µm-thick; bottom panel) devices placed on the epicardial surface of a fixed murine heart. These results confirm that the imaging artifacts (e.g., the shadow of the recording electrode pairs) were minimized with the decreased thickness of the device. Figure 4.40 presents a post-processed 3D image reconstructed from both the ultrasound images and the spatiotemporally recorded ECG signals after 60 seconds of ligation.

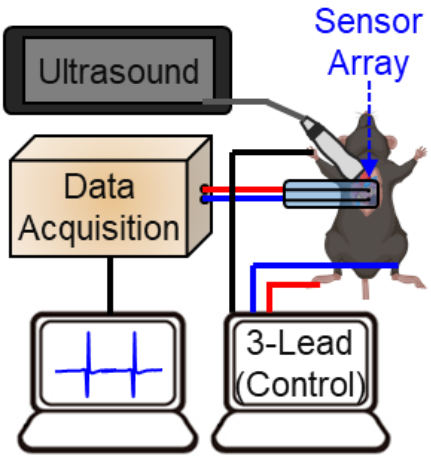

Figure 5.36. Schematic illustration of the experiment setup for simultaneous epicardial ECG recording and ultrasound imaging.

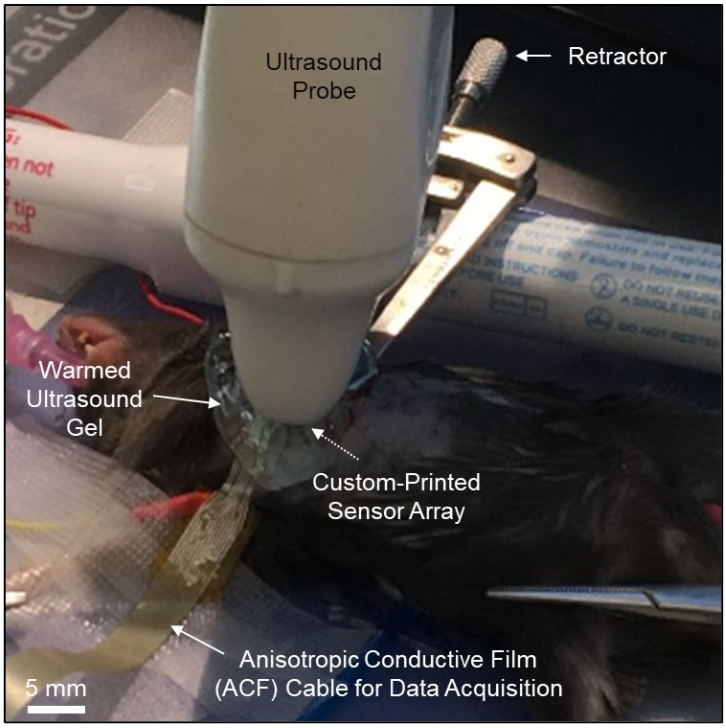

Figure 5.37. Photograph of the measurement setup for simultaneous epicardial ECG recording and ultrasound imaging.

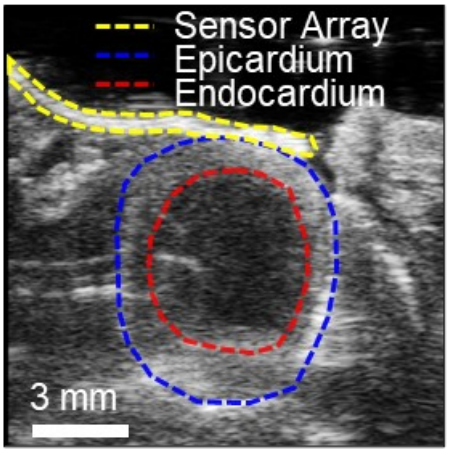

Figure 5.38. Representative short-axis ultrasound image displaying the custom-printed sensor array (yellow circle) along with the epicardium (blue circle) and endocardium (red circle) of the heart.

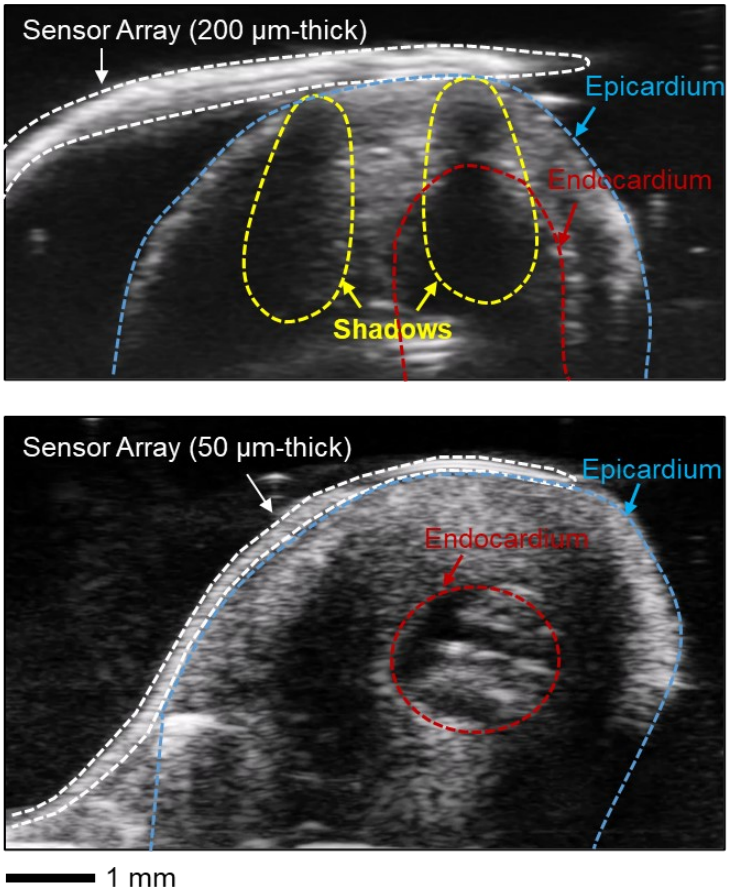

Figure 5.39. Representative ultrasound images of relatively thick (200 µm-thick; top panel) and thin (50 µm-thick; bottom panel) devices placed on the epicardial surface of a fixed murine heart.

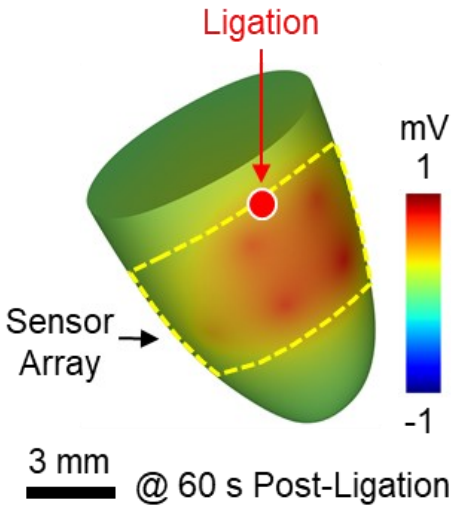

Figure 5.40. Post-processed 3D image reconstructed from the spatiotemporally recorded epicardial ECG and ultrasound signals after 60 seconds post-ligation.

5.7 Intraoperative epicardial mapping in a murine myocardial infarction model

Evaluation of the *in vivo* biocompatibility and anti-biofouling properties of the custom-printed devices and their effect on cardiac function is a critical factor for demonstrating their long-term engraftment.(Bernard, Jubeli, Pungente, & Yagoubi, 2018) To this end, we first evaluated the cellular toxicity and inflammatory response of a printed device. Figure 4.41 shows the result of a cell compatibility assay for the device that was seeded with heart myoblast (H9C2) cells in a 24-well plate (Fisher Scientific, USA), as measured using a colorimetric assay kit (MTT 3-(4,5-dimethylthiazol-2-yl)-2,5-diphenyltetrazolium bromide, Sigma-Aldrich, USA). The results indicate that the proliferation rate of the cells increased consistently throughout the assay period (24 hours), producing no significant difference compared to a control (black bar) and a bare sponge-like foam (green bar). Whereas, the device without the overcoat of Au (red bar) showed considerably reduced cell variability (< 70%), suggesting toxicity. Figure 4.42 shows representative histological cross-sectional views of the murine cardiac tissues that were stained with both hematoxylin-eosin (H&E; left panel) and Masson's trichrome (MTC; right panel) on day 14 post-implant of the device. The results revealed moderate chronic inflammation including the formation of a granuloma for the 14-days implantation. Figure 4.43 provides an overview of nearby granuloma and aorta on day 7 post-implant of the device. The magnified views of granuloma, macrophages, and multi-nucleated giant cells at the surface of the implanted device suggest chronic inflammation. Figure 4.44 presents an increased thickening of epicardium near the implanted device on days 1, 7, and 14 post-implants, showing its progression from 44.4 ± 8.3 μm to 645.9 ± 5.3 μm in thickness. The results indicate that chronic inflammatory response directed towards the implanted device. The corresponding chronic epicarditis on days 7 and 14 post-implants for pathological evaluation are shown in Figure 4.45. Detailed discussions of the histological analysis are also summarized in the Experimental Methods section.

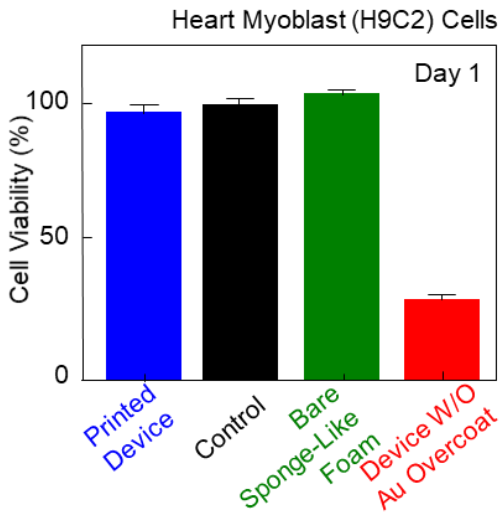

Figure 5.41. Results of cell compatibility assay for the custom-printed sensor array with heart myoblast (H9C2) cells in a 24-well plate, as measured using a colorimetric assay kit.

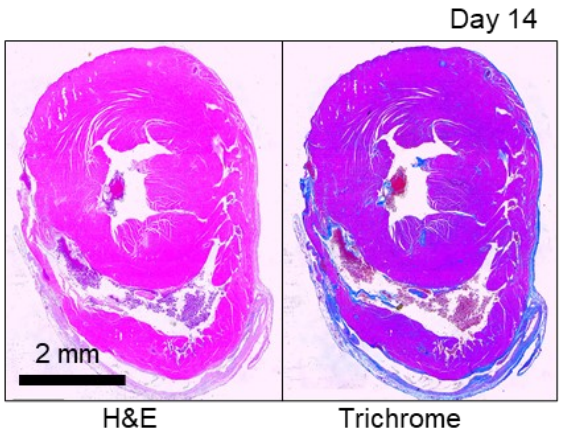

Figure 5.42. Representative histological cross-sectional views of the murine cardiac tissues that were stained with both hematoxylin-eosin (H&E; left panel) and Masson's trichrome (MTC; right panel) on day 14 post-implant of the custom-printed sensor array.

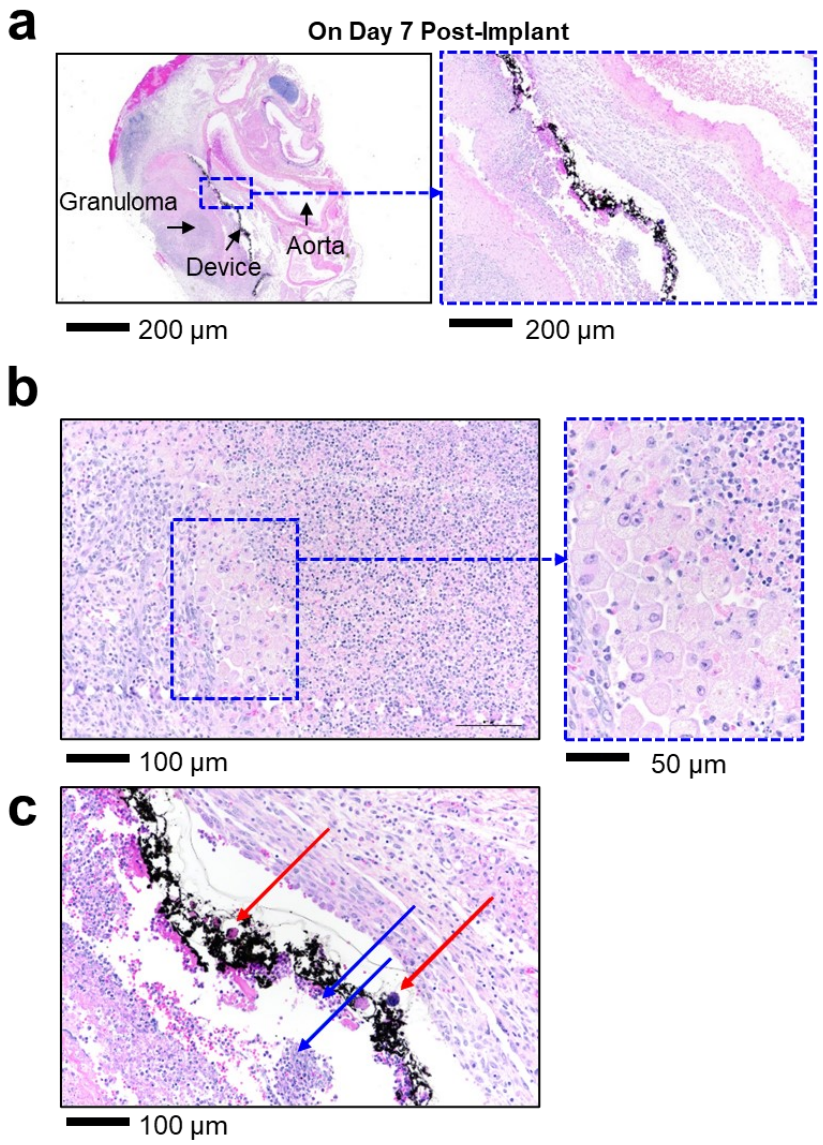

Figure 5.43. (a) Overview of granuloma and aorta on day 7 post-implant. (b) Magnified views (at 20×) of granuloma formation on day 7 post-implant. The boxed area identifies the presence of macrophages, multi-nucleated giant cells, and fibroblasts. The inset image demonstrates macrophages containing phagocytized debris resulting from the intralesional device. (c) Magnified views (20×) of macrophages and multi-nucleated giant cells at the surface of the implanted device (red arrows). The neutrophils (blue arrows) suggest acute to chronic inflammation directed at the device.

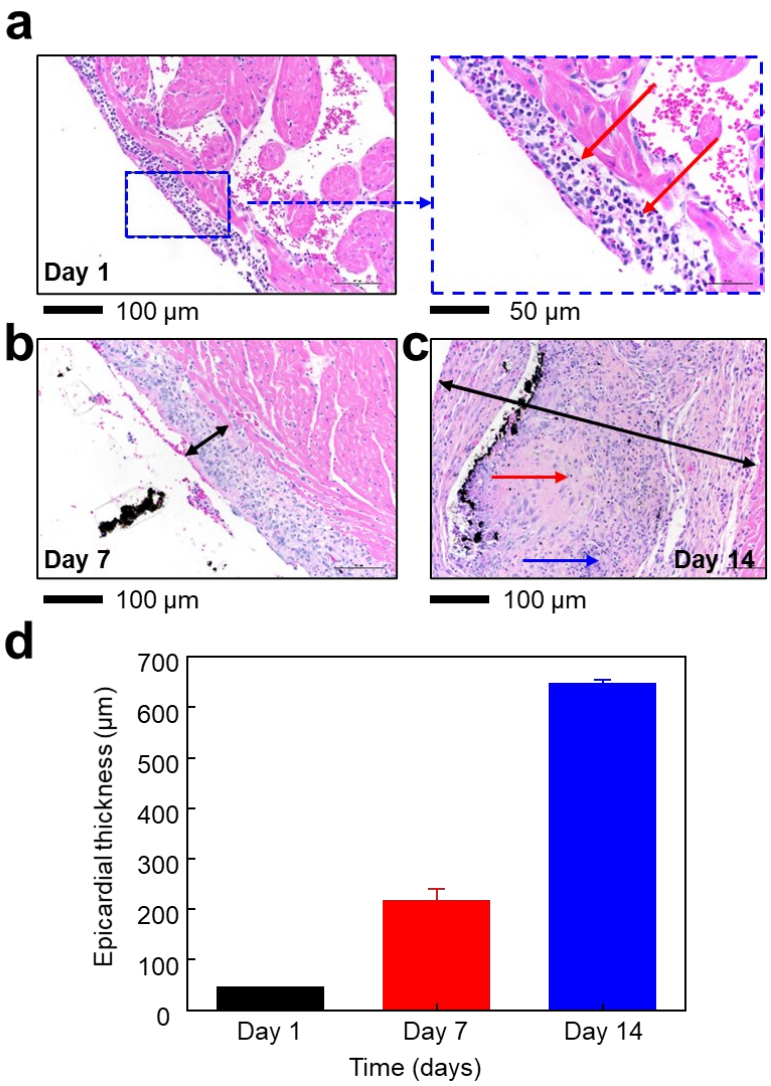

Figure 5.44. (a) Day 1 epicardium at 20 × (left) and 40 × (right) magnification. The epicardium presents at five-times normal thickness and is comprised of neutrophils (red arrows). (b) Day 7 epicardium. The double-headed line indicates a thickening of epicardium by mononuclear cells and fibroblasts due to chronic inflammatory response. (c) Day 14 epicardium. The double-headed line indicates a worsening of epicardial thickening. The presence and epithelioid morphology of macrophages (red arrow) indicate chronic granulomatous response (e.g., foreign body response) at the surface of the implanted device. The neutrophils (blue arrow) suggests that acute chronic inflammation directed towards the implanted device. (d) Progression of epicardial thickness measured using ImageJ (n = 5). The measurements were spaced at 100 µm perpendicularly from the epicardial surface to the underlying muscle layer.

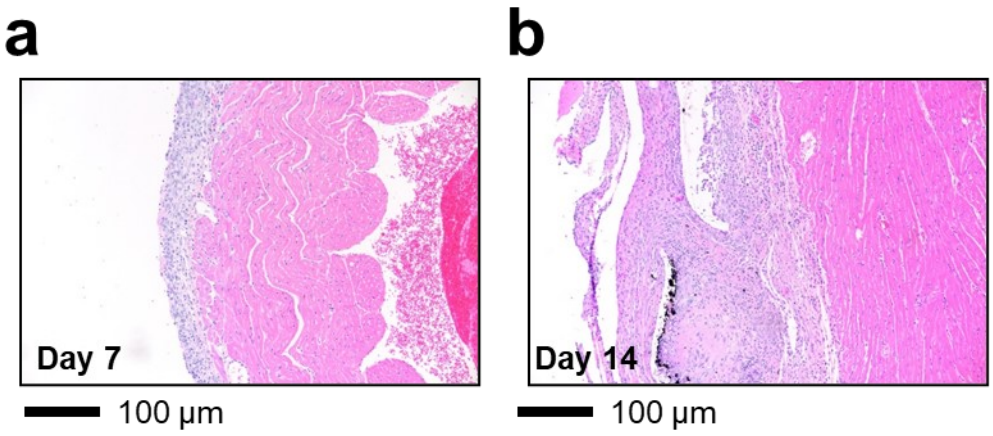

Figure 5.45. (a) Chronic epicarditis observed on day 7 post-implant. (b) Pericardial to epicardial adhesion with intralesional device observed on day 14 post-implant.

Next, we also evaluated the biofouling resistance of the device by quantifying the surface fluorescence intensity after 2 hours of incubation in 6 $mg \cdot ml^{-1}$ of a bovine serum albumin-fluorescein conjugate (BSA-FITC; A23015, Fisher Scientific, USA) diluted with 1× PBS, as compared to control groups made of the SE 1700 ink and the Sylgard 184 ink and prepared on a pristine glass (Figure 4.46). Figure 4.47 presents the corresponding results of one-way repeated measures analysis of variance (ANOVA) tests (n = 5 per group), showing statistical differences between groups. The results show that the fluorescence intensity of the device (0.7 ± 0.5 a.u.) remained significantly lower than that obtained using the Sylgard 184 ink (10.2 ± 5.5 a.u.) and the glass (15.4 ± 6.1 a.u.), suggesting that the porous surface of the device effectively prevented the accumulation of proteins.(Adiga et al., 2008; J. Xu, Xu, Moon, Sintim, & Lee, 2020) The control group made of the SE 1700 ink produced a statistically comparable degree of biofouling resistance (2.8 ± 1.7 a.u.).

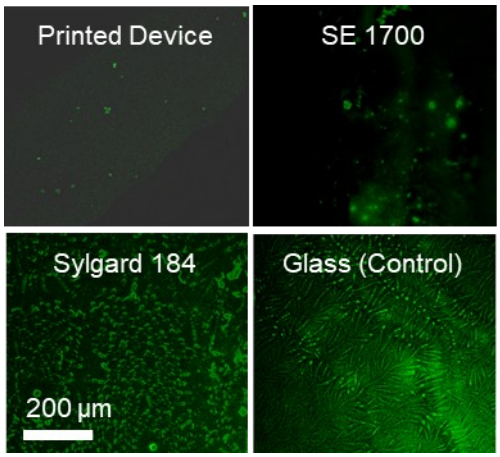

Figure 5.46. Z-stack fluorescence images of a BSA-FITC (6 mg/ml) coated on the printed device as compared to control groups made of the SE 1700 ink and the Sylgard 184 ink and prepared on a pristine glass, from upper left to bottom right clockwise.

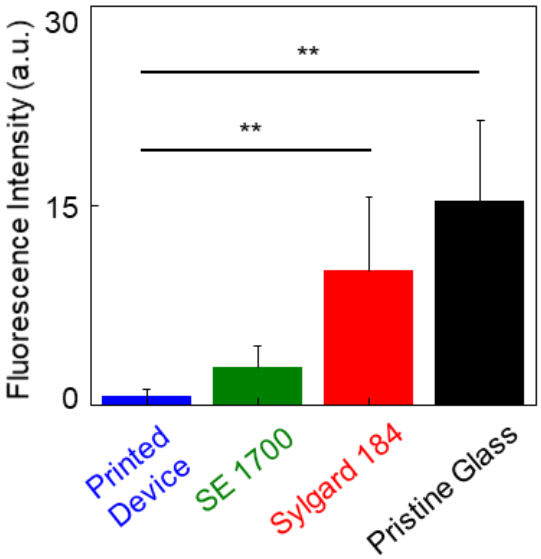

Figure 5.47. Results of one-way ANOVA tests with Bonferroni correction (n = 5 per group). Fluorescence intensity is shown as average ± standard deviation (**$p < 0.001$).

Finally, we evaluated the effect of the device on cardiac function when implanted on the epicardial surface of the murine heart and then sutured prior to anesthetic recovery. On days 0, 1, 7, and 14 post-implants, we acquired ultrasound images of the left ventricle in a long-axis (LAX) plane (Figure 4.48). With these LAX ultrasound images, the endocardial surface of the left ventricle was segmented at both end-diastole and peak-systole and used to calculate end-diastolic

volume (EDV) and peak-systolic volume (PSV) using the Simpson's rule of discs. (Otterstad, 2002) The ejection fraction (i.e., the percentage of blood pumped by the left ventricle during contraction) was then calculated using these volumes to assess global cardiac function. (Lang et al., 2015) The results confirm that the ejection fraction of the heart remained within the normal range (60-70%; green highlighted area) without noticeable decrease throughout the entire implantation period (Figure 4.49), which was clearly higher than the abnormal ranges for ischemia reperfusion injury (40-60%; yellow highlighted area) and permanent ligation (20-40%; red highlighted area).

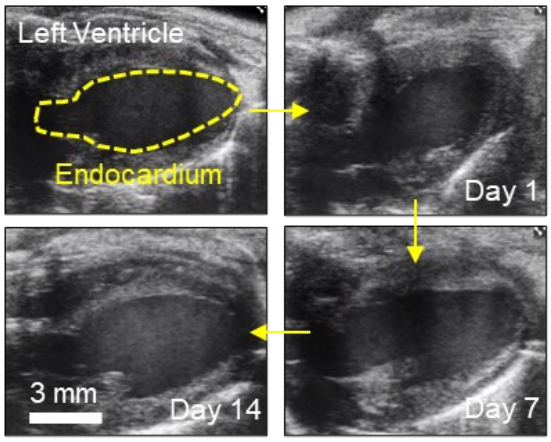

Figure 5.48. Representative ultrasound images of the left ventricle of a murine heart on 0, 1, 7, and 14 days implantation of the custom-printed sensor array.

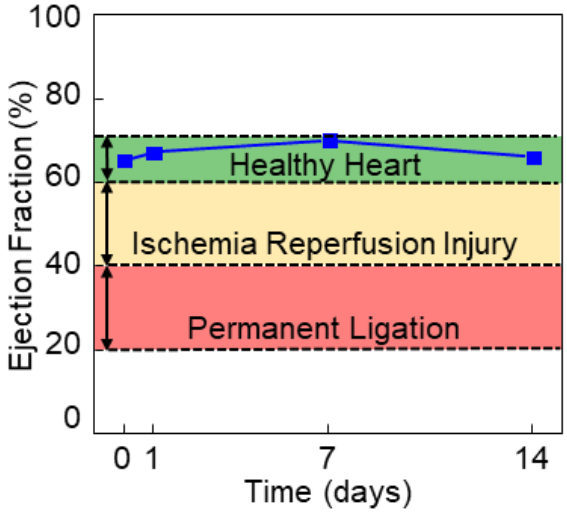

Figure 5.49. Results of the ejection fraction of the murine heart post-implant.

5.8 Methods

5.8.1 4D heart segmentation

All ultrasound images were acquired using the Vevo 3100 small animal ultrasound system (FUJIFILM VisualSonics Inc., Toronto, Canada). The 4D ultrasound data (3D geometric volume over a cardiac cycle) of adult mouse hearts with well-developed infarcts were acquired via high-frequency ultrasound. The cardiac and respiratory-gated 2D short-axis images were acquired from the apex to the base of the left ventricle and spatiotemporally synced to generate the 4D ultrasound data. The reconstructed data was resampled to isotropic voxels and exported to SimVascular for the 3D segmentation at both end-diastolic and peak-systolic timepoints. (Updegrove et al., 2017) STL files of the myocardial wall were then created with uniform meshing and used to design the devices.

5.8.2 Ink composition and preparation

The formulated inks were prepared by blending the following three compositions: a base resin, Sylgard 184, and SiO_2-PS silica particle, in a specific weight ratio (5.7:3.3:1.0, 4.2:5.0:0.8, 6.0:3.3:0.7, and 4.5:5.0:0.5) with a mixer (Thinky Mixer) for 5 minutes at 2,000 rpm. The base resin was prepared by blending 64.5 wt% of vinyl terminated diphenylsiloxane-dimethylsiloxane copolymer (a mixture of 9:1 weight ratio of PDV-0541 and PDV-0525), 33.5 wt% of trimethylsiloxane terminated methylhydrosiloxane-dimethylsiloxane copolymer (HMS-151), and 2.0 wt% of 1,3,5,7-tetravinyl-1,3,5,7-tetramethylcyclotetrasiloxane (siloxane monomer). Sylgard 184 (a mixture of 10:1 weight ratio of base and curing agent) was used as a dilute resin. The SiO_2-PS particles and Pt-carbonyl cyclovinylmethylsiloxane complex (Pt catalyst; 0.1 wt% of the amount of base resin) were added and blended using a mixer (Thinky Mixer) for 2 minutes at 2,000 rpm to adjust the rheological properties of the ink. The control inks (e.g., Sylgard 184 and SE 1700) were prepared by mixing the base and curing agent at the standard 10:1 weight ratio.

5.8.3 Mechanical and electrical measurements under cyclic strains

The well-mixed blends for the formulated inks with a certain ratio were spin-casted on a water-soluble film (PVA, Sigma-Aldrich, 10 μm-thick) to form a thin layer of the thickness of 150

μm. Any air bubbles introduced during the casting process were removed before placing the lids on the molds. Following polymerization at 120 °C for 30 minutes in an oven, the specimens were allowed to cool down to room temperature for about 15 minutes and then trimmed into a rectangular shape with the width of 2 mm. Tensile strength was measured using a mechanical testing system (Mark-10). The specimens were loaded into uniaxial grips and then pulled to reach a breakpoint at a speed of 20 $mm \cdot min^{-1}$. A total of 5 trials per specimen was taken, and the corresponding standard deviation was reported as a measurement error. For the electrical measurement, a source meter (Keithley 2400, Tektronix) and a custom-built LabView code (National Instruments) were used in a two-wire configuration.

5.8.4 Measurement of rheological properties

Rheological measurements were carried out on a Rheometer (Discovery Hybrid Rheometer-2, TA Instrument) using parallel plate fixtures with a diameter of 25 mm. The viscosity and shear moduli were measured by stress sweeps ranging from 0.1 to 65,000 Pa at a fixed angular frequency of 10 $rad \cdot sec^{-1}$ for each measurement. Oscillatory time sweeps were measured to investigate gel-points (i.e., working lifetime), where the storage modulus (G') becomes larger than the loss modulus (G") at an angular frequency of 10 $rad \cdot sec^{-1}$ and a strain rate of 4%.

5.8.5 Molecular dynamics (MD) simulation

The Forcite and Amorphous Cell modules in Material Studio (BIOVIA, UK) were used for the MD simulation. The density of the surface treated-layer, composed of one vinyl terminated diphenylsiloxane-dimethylsiloxane copolymer and three trimethylsiloxane terminated methylhydrosiloxane-dimethylsiloxane copolymer main-chains, was set to 0.97 $g \cdot cm^{-3}$. Geometry-optimized 3D models were followed by the anneal protocol in which the temperature of the system was sequentially set to 298, 398, 498, and 598 K, and then decreased in reverse using a constant-volume ensemble (NVT). Each step was performed for 50 ps, and the anneal protocol was repeated 5 times. The interaction energies of the 3D models were obtained after additional NVT dynamics at 298 K for 1,000 ps. The Condensed-phase Optimized Molecular Potentials for Atomistic Simulation Studies (COMPASS) II force field, the Ewald summation method for non-bonding interactions with an accuracy of 0.001 $kcal \cdot mol^{-1}$, the time step of 1.0 fs, the Andersen temperature

control method with 1 as the collision ratio, and the Berendsen pressure control method with 0.1 ps as the decay constant were chosen.

5.8.6 Fabrication of custom-printed sensor array

The process began with a Si wafer coated with a thin layer (1 μm-thick) of polymethyl methacrylate (PMMA) as a chemically-dissolvable sacrificial layer. The surface of the PMMA layer was exposed with 3-aminopropyltriethoxysilane (APTES) in a vacuum desiccator to form a hydrophilic silane group to improve the adhesion strength. A direct writing of the formulated ink was followed using the nozzle injection system (Nordson EFD). For the formation of micropores, the as-printed (prepolymer) ink was annealed in a pressure rice cooker (Max, Instant Pot, Inc.) in which the steam temperature and pressure were set at 120 °C and 15 psi with the ramping rate of 15°C per minute and 5.6 psi per minute, respectively. Next, the resulting structure was immersed in a mixture solution (200 ml) of hexane and Ag flakes (200 nm-5 μm in diameter; Inframat Advanced Materials, LLC) to trap the Ag flakes into the internal pores. The structure was then immersed in a Cu plating solution that contains (1) copper(II) sulfate pentahydrate ($CuSO_4 \cdot 5H_2O$, Sigma-Aldrich; 18 $g \cdot L^{-1}$), (2) Ethylenediaminetetraacetic acid (EDTA, Sigma-Aldrich; 48 $g \cdot L^{-1}$), (3) Potassium hexacyanoferrate(II) trihydrate ($K_4[Fe(CN)_6] \cdot 3H_2O$, Sigma-Aldrich; 600 mg/L), (4) Sodium Hydroxide (NaOH, Fisher scientific; 45 $g \cdot L^{-1}$), (5) Poly(ethylene glycol) ($H(OCH_2CH_2)_nOH$, Sigma-Aldrich; 500 $mg \cdot L^{-1}$), (6) Formaldehyde (HCHO, Fisher scientific; 20 $mL \cdot L^{-1}$), and (7) hydrochloric acid solution (1 N) (HCl, Fisher Scientific; 18 $mL \cdot L^{-1}$) for 30 minutes. The Cu-plated surface was subsequently plated with Au for 2 minutes using an electroplating system (24K Pure gold plating solution-Bath, Gold Plating Services), followed by thorough rinsing with deionized (DI) water. A layer (~50 μm-thick) of polyvinyl alcohol (PVA, Sigma-Aldrich) was drop-casted to form the temporary handling support. Following the complete dissolution of the bottom PMMA layer with acetone, the complete device was physically separated from the Si wafer by gently peeling the PVA layer. Trimming the excess area of the PVA layer completed the entire process.

5.8.7 Animal surgeries on mice

All surgical procedures on mice were performed aseptically and approved by the Purdue Animal Care and Use Committee under protocol number 1505001246. Adult male mice (> 12 weeks old; wild-type; C57BL/6J; The Jackson Laboratory, Bar Harbor, ME) were used for this study. To prepare for surgery, each mouse was anesthetized with 1-3% isoflurane delivered in 100% O_2 and endotracheally intubated to a small animal ventilator (SomnoSuite, Kent Scientific, Torrington, CT). To prevent pneumothorax, a pressure-controlled ventilation was employed to maintain a target inspiratory pressure of 18 cm H_2O and a peak-end expiratory pressure of 5 cm H_2O in the lungs. The mouse was secured to a heated surgical stage, and the body temperature was kept between 36 °C and 37 °C using a homeothermic control module. A 3-lead needle electrode set (ERT Control/Gating Module Model 1030, SA Instruments, Stony Brook, NY) was positioned in a Lead I configuration to continuously collect ECG waveforms throughout the surgical procedure at a sampling rate of 900 Hz. A small incision was made along the third intercostal space of the left thorax, and the ribs were retracted to expose the left ventricle before dissecting the pericardium to identify the left coronary artery. For acute infarction studies (n = 5), an 8-0 nylon suture was loosely looped around the left coronary artery, and the testbed custom-printed devices were placed on the epicardial surface using a water-soluble medical tape (PVA; 50 µm-thick, Sigma-Aldrich, USA). Warmed sterile saline was applied to completely dissolve the water-soluble tape within no more than 30 seconds. A suture was tightened to permanently ligate the left coronary artery in order to induce an acute infarct. Successful ligation was confirmed by discoloration of the myocardium in regions distal to the ligation site and global ST segment elevation or depression in the 3-lead electrode set. The ECG data from both the printed devices and the control 3-lead electrodes were acquired simultaneously and synchronized by their timestamps. The mice in the acute infarction group were euthanized humanely at the end of the procedure. For implantation surgeries (n = 3), we placed the printed device (50 µm-thick) to the epicardial surface as mentioned previously, sutured close the incision site, and allowed the mice to recover. Buprenorphine (0.05 $mg \cdot kg^{-1}$ animal body weight) was administered via intraperitoneal injection as an analgesic. The left ventricles of these mice were imaged with ultrasound on days 1, 7, and 14 post-implants, and one mouse was euthanized at each time point for longitudinal histological data.

5.8.8 Animal surgeries on pigs

All surgical procedures on pigs were terminal, performed by a trained veterinary team from Purdue University's College of Veterinary Medicine, and approved by the Purdue Animal Care and Use Committee under protocol number 1406001099. Adult domestic pigs (n = 2) were anesthetized and intubated with a ventilator throughout the entire procedure. A median sternotomy was conducted and the pericardium was cut to visualize the anterior wall of the left ventricle. The custom-printed devices, configured with total 16 electrodes (i.e., 8 recording channels, were then placed onto the epicardial surface of the left ventricle using a water-soluble medical tape. Warmed sterile saline was applied to dissolve the water-soluble tape for a tight conformal contact, and ECG waveforms were recorded continuously.

5.8.9 Simultaneous ultrasound imaging during ECG recording

All ultrasound images were acquired using the Vevo 3100 small animal ultrasound system (FUJIFILM VisualSonics Inc., Toronto, Canada). For the preparation prior to imaging, mice were anesthetized with 1-3% isoflurane delivered in medical-grade air and positioned supine on a heated imaging stage, with paws secured to gold-plated stage electrodes to monitor for ECG and respiration signals. A 40 MHz central frequency linear array transducer with 256 elements (22-55MHz; MX550D) was then positioned on the left ventral thorax to acquire ultrasound images in multiple long and short-axis planes. For the data acquisition, both ECG and respiratory gatings were implemented to minimize breathing artifacts and to acquire cardiac cine loops at 1,000 Hz. To evaluate left ventricular function, the endocardial surface of the left ventricle was manually segmented at end-diastole and peak-systole to approximate left ventricular volumes using the Simpson's rule of discs.(Lang et al., 2015) Ejection fraction (EF) was then calculated as follows:

$$EF = \frac{EDV\text{-}PSV}{EDV} \times 100$$

where EDV and PSV correspond to end-diastolic volume and peak-systolic volume, respectively. For the *in vivo* open chest imaging, a warmed ultrasound gel was applied directly onto the epicardially-implanted device on the beating heart at the end of several infarction surgeries. Several representative short-axis images of the left ventricle were acquired to visualize

adherence of the patch to the left ventricle. For the ex vivo ultrasound imaging on fixed tissues, the devices (50-300 μm-thick) were placed on the epicardial surface of the previously fixed left ventricles. An ultrasound gel was used as a conductive medium between the transducer and the fixed tissue. Multiple short-axis images of the left ventricles were acquired to investigate how the devices impact on the quality of ultrasound imaging.

5.8.10 Anti-biofouling analysis

The biofouling resistance of the printed devices was analyzed following the same procedures as reported in a previous study. The specimens were incubated in bovine serum, fluorescein conjugate (BSA-FITC; 6 $mg \cdot ml^{-1}$) diluted in 1× phosphate-buffered solution for 2 hours in a 6-well plate protected from light at room temperature (n = 5 per group). The specimens were then rinsed with 1× phosphate-buffered solution prior to air-drying and imaging. The fluorescence z-stack images were captured at 10× magnification using an inverted fluorescence microscope (Axio Observer Z1, Carl Zeiss Microscopy, Jena, Germany). The fluorescence intensity was quantified using a Java-based image processing program (ImageJ). All images were acquired using the same exposure settings to ensure no over- or under-saturated pixels (pixel values = 0-255) or image histogram aberrations. The mean intensity and standard deviation were measured from whole image selections, and the statistical analysis was performed with the SAS software (SAS Institute).

5.8.11 Histological analysis

At the end of the implantation experiment, mice were euthanized humanely. A retrograde perfusion was performed from the inferior vena cava using 30 mM potassium chloride (KCl) solution to clear residual blood and arrest the heart in diastole. The heart was harvested while minimizing any disruption to the implanted device on the epicardial surface and then fixed in 4% paraformaldehyde for 7 days at 4 °C before sending the samples for histology. The hearts were embedded in paraffin, thinly sectioned (5 μm-thick), and stained with hematoxylin-eosin (H&E) and Masson's trichrome (MTC). The stained tissues were imaged in segments at 10×, 20×, and 40× magnification using a Leica ICC50W stereomicroscope (Leica Microsystems Inc., Buffalo Grove, IL), and stitched together with MosaicJ. Epicardial thickening was measured from

histological images using ImageJ. Microscopic examination was performed by a board-certified veterinary pathologist and the interpretation was based on standard histopathological morphology of a murine heart. Four serial transverse sections of the heart from the base to the mid-papillary region were histologically evaluated. The results revealed that, on day 7 post-implant, the implanted device was present adjacent to the wall of aorta invoking the formation of a granuloma (Figure 4.43). The granuloma was comprised of a central necrotic core of eosinophilic cellular and karyorrhectic debris mixed with numerous degenerate and viable neutrophils. Surrounding the necrotic core were epithelioid macrophages and multinucleated giant cells, rimmed peripherally by lymphocytes, plasma cells, fibroblasts, and fibrous connective tissue. The epicardium of the right and left atrium was expanded by fibroblasts admixed by neutrophils, lymphocytes and macrophages (Figure 4.44). The fragments of the foreign materials surrounded by inflammatory cells were found adjacent to the wall of the right atrium. On day 14 post-implant, the epicardium of the right ventricle was thickened with pale eosinophilic collagen fibers and increased fibroblast cellularity. The pericardium was similarly thickened with collagen, numerous fibroblasts, small caliber blood vessels and infiltrates of lymphocytes, plasma cells, macrophages, multinucleate giant cells and few neutrophils. The thickened pericardium surrounded fragments of granular, black foreign material with multifocal adhesions to the underlying epicardium (Figure 4.45). The observed lesions predominantly bordered the right ventricular free wall. The pericardium was only observed on the right-side following tissue processing, likely because the pericardium was adhered to the underlying inflamed epicardium. Although chronic inflammation due to a foreign body response was present at the implant site after long-term implantation, its effects on intraoperative epicardial mapping or cardiac ejection fraction were insignificant. While short-term intraoperative implantation side effects cannot be ruled out, we observed no issues during intraoperative epicardial mapping or cardiac ejection fraction. The inflammation could be further reduced through the inclusion of anti-biofouling surfacing coatings or textures.(Jian Xu et al., 2020; Jinjia Xu et al., 2020; J. Xu, Xu, Moon, Sintim, & Lee, 2021)

5.9 Conclusion

The results reported herein suggest a route towards rapid prototyping of thin and stretchable poroelastic biosensors with a custom-fit design that can meet a specific geometric demand in clinical practices. The determination of a new formula for a dispensable silicone ink leads to

optimal rheological properties that enable both (1) the high-precision DIW of arbitrary functional microarchitectures at various length scales and (2) the capability of turning the printed microarchitectures into a sponge-like foam in a deterministic manner. Uniquely, the resulting devices are monolithic in which the densely networked conductive nanofillers are embedded through the internal pores in a way that eliminates a risk of compromising their structural integrity even under large deformations. The poroelastic nature of the devices can be used to establish a robust coupling to the epicardial surface and also remain insensitive to periodic cardiac cycle and respiratory motion without significant mechanical and electrical hysteresis. The simultaneous intraoperative monitoring of both epicardial ECG and ultrasound signals in a murine acute myocardial infarction model suggests a potential utility of the device for high-fidelity acquisition of real-time 3D cardiac mapping, which may guide surgical interventions such as ablation for arrythmias. The *in vivo* studies also suggest an opportunity to further increase the spatial resolution of these devices (i.e., the number of electrodes within a given region) in order to alleviate the need for reliance on post-processing algorithms to map the site of myocardial infarction in a higher resolution. The basic concept of this approach may be potentially expandable for continuous monitoring of lethal cardiac diseases through chronic implantation of the devices and integration with current state-of-the-art means of wirelessly communicating power and data.(Won, Song, Reeder, & Rogers, 2020)

6. CONCLUSION

This thesis captures a wide range of advanced additive manufacturing methods for their use in optical and biomedical systems. These manufacturing methods circumvent the incompatibility between conventional microfabrication processes and nonconventional flexible substrates, thereby significantly broadening consideration of complex configurations or miniaturized multidimensional systems. Also, the most attractive advantage of these approaches arises from the cost-effectiveness of their fabrication process and infrastructure comparing to conventional manufacturing at the micro/nano-scale.

These manufacturing methods have also enabled functional advances in optical and biomedical sensors with an increased sensing capability. They are applicable to quasi-3D plasmonic nanoarchitectures to be integrated with existing imagers in a deterministic manner without significantly increasing the size, weight, cost, and complexity. Besides, the modification of these methods with electrochemical reaction-driven delamination enables repetitive replication of the quasi-3D nanoarchitectures without defects over large areas up to 4-inch wafer scale. These features will apply novel optical systems to sense and process complex information in the incident light from the target object. Furthermore, the highly developed quasi-3D imager is applicable to performing real-time hyperspectral imaging, spectropolarimetric analysis of optical information across different wavelength ranges by repetitive replication of optically functional nanoarchitectures over large areas.

The rapid custom-fit prototyping enables a high-throughput assembly of stretchable conducting inks into biosensors that can reliably detect biosignals from the surface of the heart under beating with minimal mechanical and electrical hysteresis. The resulting biosensor platform will extend its applicability to the reliable monitoring of other, biopotential waveforms including but not limited from the brain (i.e., electroencephalograms, electrocorticography), neurological activation of skeletal muscle (i.e., electromyograms), and electrical activity of the retina in response to a light stimulus (i.e. electroretinograms). As such, I envision this platform technology to enable advances in a broad range of biomedical practices.

REFERENCES

Adiga, S. P., Curtiss, L. A., Elam, J. W., Pellin, M. J., Shih, C.-C., Shih, C.-M., . . . Narayan, R. J. (2008). Nanoporous materials for biomedical devices. *JOM, 60*(3), 26-32. doi:10.1007/s11837-008-0028-9

Al-Salam, S., & Hashmi, S. (2014). Galectin-1 in Early Acute Myocardial Infarction. *PLOS ONE, 9*(1), e86994. doi:10.1371/journal.pone.0086994

Alharbi, A., Nasri, B., Wu, T., & Shahrjerdi, D. (2016, 3-7 Dec. 2016). *Advanced integrated sensor and layer transfer technologies for wearable bioelectronics.* Paper presented at the 2016 IEEE International Electron Devices Meeting (IEDM).

Amenabar, I., Poly, S., Goikoetxea, M., Nuansing, W., Lasch, P., & Hillenbrand, R. (2017). Hyperspectral infrared nanoimaging of organic samples based on Fourier transform infrared nanospectroscopy. *Nature Communications, 8*(1), 14402. doi:10.1038/ncomms14402

Amjadi, M., Pichitpajongkit, A., Lee, S., Ryu, S., & Park, I. Highly Stretchable and Sensitive Strain Sensor based on Ag NWs-Elastomer Nanocomposite.

Arora, N., & Mishra, B. (2020, 7-11 Jan. 2020). *Characterization of a Low Cost, Automated and Field Deployable 2-Lead Myocardial Infarction Detection System.* Paper presented at the 2020 International Conference on COMmunication Systems & NETworkS (COMSNETS).

Ashraf, S., Niskanen, I., Kanyathare, B., Vartiainen, E., Mattsson, C., Heikkilä, R., & Thungström, G. (2019). Determination of complex refractive index of SU-8 by Kramers–Kronig dispersion relation method at the wavelength range 2.5–22.0 µm. *Journal of Quantitative Spectroscopy and Radiative Transfer, 224*, 309-311. doi:https://doi.org/10.1016/j.jqsrt.2018.11.026

Atwater, H. A., & Polman, A. (2010). Plasmonics for improved photovoltaic devices. *Nat Mater, 9*(3), 205-213. doi:10.1038/nmat2629

Au - Scofield, S. L. C., & Au - Singh, K. (2016). Confirmation of Myocardial Ischemia and Reperfusion Injury in Mice Using Surface Pad Electrocardiography. *JoVE*(117), e54814. doi:doi:10.3791/54814

Azad, A. K., Hara, J. F. O., Singh, R., Chen, H., & Taylor, A. J. (2013). A review of terahertz plasmonics in subwavelength holes on conducting films. *IEEE Journal of Selected Topics in Quantum Electronics, 19*(1), 8400416-8400416. doi:10.1109/JSTQE.2012.2208181

Bedell, S. W., Shahrjerdi, D., Hekmatshoar, B., Fogel, K., Lauro, P. A., Ott, J. A., . . . Sadana, D. (2012). Kerf-Less Removal of Si, Ge, and III–V Layers by Controlled Spalling to Enable Low-Cost PV Technologies. *IEEE Journal of Photovoltaics, 2*(2), 141-147. doi:10.1109/JPHOTOV.2012.2184267

Bernard, M., Jubeli, E., Pungente, M. D., & Yagoubi, N. (2018). Biocompatibility of polymer-based biomaterials and medical devices – regulations, in vitro screening and risk-management. *Biomaterials Science, 6*(8), 2025-2053. doi:10.1039/C8BM00518D

Carlson, A., Kim-Lee, H.-J., Wu, J., Elvikis, P., Cheng, H., Kovalsky, A., . . . Rogers, J. A. (2011). Shear-enhanced adhesiveless transfer printing for use in deterministic materials assembly. *Applied Physics Letters, 98*(26), 264104. doi:10.1063/1.3605558

Chanda, D., Shigeta, K., Gupta, S., Cain, T., Carlson, A., Mihi, A., . . . Rogers, J. A. (2011). Large-area flexible 3D optical negative index metamaterial formed by nanotransfer printing. *Nat Nanotechnol, 6*(7), 402-407. doi:10.1038/nnano.2011.82

Chanda, D., Shigeta, K., Truong, T., Lui, E., Mihi, A., Schulmerich, M., . . . Rogers, J. A. (2011). Coupling of plasmonic and optical cavity modes in quasi-three-dimensional plasmonic crystals. *Nat Commun, 2*, 479. doi:10.1038/ncomms1487

Chang, C. C., Sharma, Y. D., Kim, Y. S., Bur, J. A., Shenoi, R. V., Krishna, S., . . . Lin, S. Y. (2010). A surface plasmon enhanced infrared photodetector based on InAs quantum dots. *Nano Lett, 10*(5), 1704-1709. doi:10.1021/nl100081j

Cheben, P., Halir, R., Schmid, J. H., Atwater, H. A., & Smith, D. R. (2018). Subwavelength integrated photonics. *Nature, 560*(7720), 565-572. doi:10.1038/s41586-018-0421-7

Chen, G., Rastak, R., Wang, Y., Yan, H., Feig, V., Liu, Y., . . . Bao, Z. (2019). Strain- and Strain-Rate-Invariant Conductance in a Stretchable and Compressible 3D Conducting Polymer Foam. *Matter, 1*(1), 205-218. doi:https://doi.org/10.1016/j.matt.2019.03.011

Chen, Y.-B. (2009). Development of mid-infrared surface plasmon resonance-based sensors with highly-doped silicon for biomedical and chemical applications. *Optics Express, 17*(5), 3130-3140. doi:10.1364/OE.17.003130

Chen, Y. (2015). Nanofabrication by electron beam lithography and its applications: A review. *Microelectronic Engineering, 135*, 57-72. doi:10.1016/j.mee.2015.02.042

Cheng, C. W., Shiu, K. T., Li, N., Han, S. J., Shi, L., & Sadana, D. K. (2013). Epitaxial lift-off process for gallium arsenide substrate reuse and flexible electronics. *Nat Commun, 4*, 1577. doi:10.1038/ncomms2583

Choi, M. K., Yang, J., Kang, K., Kim, D. C., Choi, C., Park, C., . . . Kim, D.-H. (2015). Wearable red–green–blue quantum dot light-emitting diode array using high-resolution intaglio transfer printing. *Nature Communications, 6*(1), 7149. doi:10.1038/ncomms8149

Choi, S., Han, S. I., Jung, D., Hwang, H. J., Lim, C., Bae, S., . . . Kim, D.-H. (2018). Highly conductive, stretchable and biocompatible Ag–Au core–sheath nanowire composite for wearable and implantable bioelectronics. *Nature Nanotechnology, 13*(11), 1048-1056. doi:10.1038/s41565-018-0226-8

Costa, P., Ribeiro, S., & Lanceros-Mendez, S. (2015). Mechanical vs. electrical hysteresis of carbon nanotube/styrene–butadiene–styrene composites and their influence in the electromechanical response. *Composites Science and Technology, 109*, 1-5. doi:https://doi.org/10.1016/j.compscitech.2015.01.006

Cuculich, P. S., Zhang, J., Wang, Y., Desouza, K. A., Vijayakumar, R., Woodard, P. K., & Rudy, Y. (2011). The Electrophysiological Cardiac Ventricular Substrate in Patients After Myocardial Infarction. *Journal of the American College of Cardiology, 58*(18), 1893. doi:10.1016/j.jacc.2011.07.029

Daalkhaijav, U., Yirmibesoglu, O. D., Walker, S., & Mengüç, Y. (2018). Rheological Modification of Liquid Metal for Additive Manufacturing of Stretchable Electronics. *Advanced Materials Technologies, 3*(4), 1700351. doi:10.1002/admt.201700351

Deshpande, A., & Birnbaum, Y. (2014). ST-segment elevation: Distinguishing ST elevation myocardial infarction from ST elevation secondary to nonischemic etiologies. *World journal of cardiology, 6*(10), 1067-1079. doi:10.4330/wjc.v6.i10.1067

Digaum, J. L., Pazos, J. J., Chiles, J., D'Archangel, J., Padilla, G., Tatulian, A., . . . Kuebler, S. M. (2014). Tight control of light beams in photonic crystals with spatially-variant lattice orientation. *Optics Express, 22*(21), 25788-25804.

Dross, F., Robbelein, J., Vandevelde, B., Van Kerschaver, E., Gordon, I., Beaucarne, G., & Poortmans, J. (2007). Stress-induced large-area lift-off of crystalline Si films. *Applied Physics A, 89*(1), 149-152. doi:10.1007/s00339-007-4195-2

Duempelmann, L., Gallinet, B., & Novotny, L. (2017). Multispectral Imaging with Tunable Plasmonic Filters. *ACS Photonics, 4*(2), 236-241. doi:10.1021/acsphotonics.6b01003

Emadi, A., Wu, H., de Graaf, G., & Wolffenbuttel, R. (2012). Design and implementation of a sub-nm resolution microspectrometer based on a Linear-Variable Optical Filter. *Optics Express, 20*(1), 489-507. doi:10.1364/OE.20.000489

Fan, W., Zhang, S., Malloy, K. J., & Brueck, S. R. J. (2005). Enhanced mid-infrared transmission through nanoscale metallic coaxial-aperture arrays. *Optics Express, 13*(12), 4406-4413. doi:10.1364/OPEX.13.004406

Fan, W., Zhang, S., Minhas, B., Malloy, K. J., & Brueck, S. R. (2005). Enhanced infrared transmission through subwavelength coaxial metallic arrays. *Phys Rev Lett, 94*(3), 033902. doi:10.1103/PhysRevLett.94.033902

Feng, X., Meitl, M. A., Bowen, A. M., Huang, Y., Nuzzo, R. G., & Rogers, J. A. (2007). Competing Fracture in Kinetically Controlled Transfer Printing. *Langmuir, 23*(25), 12555-12560. doi:10.1021/la701555n

Fernández-Domínguez, A. I., García-Vidal, F. J., & Martín-Moreno, L. (2017). Unrelenting plasmons. *Nature Photonics, 11*(1), 8-10. doi:10.1038/nphoton.2016.258

Fowkes, F. M. (1963). ADDITIVITY OF INTERMOLECULAR FORCES AT INTERFACES. I. DETERMINATION OF THE CONTRIBUTION TO SURFACE AND INTERFACIAL TENSIONS OF DISPERSION FORCES IN VARIOUS LIQUIDS1. *The Journal of Physical Chemistry, 67*(12), 2538-2541. doi:10.1021/j100806a008

Franklin, D., Frank, R., Wu, S. T., & Chanda, D. (2017). Actively addressed single pixel full-colour plasmonic display. *Nat Commun, 8*, 15209. doi:10.1038/ncomms15209

Fu, H., Nan, K., Bai, W., Huang, W., Bai, K., Lu, L., . . . Rogers, J. A. (2018). Morphable 3D mesostructures and microelectronic devices by multistable buckling mechanics. *Nat Mater, 17*(3), 268-276. doi:10.1038/s41563-017-0011-3

Gao, L., Shigeta, K., Vazquez-Guardado, A., Progler, C. J., Bogart, G. R., Rogers, J. A., & Chanda, D. (2014). Nanoimprinting Techniques for Large-Area Three-Dimensional Negative Index Metamaterials with Operation in the Visible and Telecom Bands. *ACS Nano, 8*(6), 5535-5542. doi:10.1021/nn5015775

Gent, A. N., & Lai, S. M. (1994). Interfacial bonding, energy dissipation, and adhesion. *Journal of Polymer Science Part B: Polymer Physics, 32*(8), 1543-1555. doi:10.1002/polb.1994.090320826

Goldflam, M. D., Hawkins, S. D., Parameswaran, S., Tauke-Pedretti, A., Warne, L. K., Peters, D. W., . . . Kim, J. K. (2017, 4-11 March 2017). *Next-generation infrared focal plane arrays for high-responsivity low-noise applications.* Paper presented at the 2017 IEEE Aerospace Conference.

Guo, S.-Z., Qiu, K., Meng, F., Park, S. H., & McAlpine, M. C. (2017). 3D Printed Stretchable Tactile Sensors. *Advanced Materials, 29*(27), 1701218. doi:10.1002/adma.201701218

Huang, E. K.-w., Haddadi, A., Chen, G., Nguyen, B.-M., Hoang, M.-A., McClintock, R., . . . Razeghi, M. (2011). Type-II superlattice dual-band LWIR imager with M-barrier and Fabry–Perot resonance. *Optics Letters, 36*(13), 2560-2562. doi:10.1364/OL.36.002560

Huang, E. K.-w., Hoang, M.-A., Chen, G., Ramezani-Darvish, S., Haddadi, A., & Razeghi, M. (2012). Highly selective two-color mid-wave and long-wave infrared detector hybrid based on Type-II superlattices. *Optics Letters, 37*(22), 4744-4746. doi:10.1364/OL.37.004744

Huang, Q., Peh, J., Hergenrother, P. J., & Cunningham, B. T. (2016). Porous photonic crystal external cavity laser biosensor. *Appl Phys Lett, 109*(7), 071103. doi:10.1063/1.4961107

Hutchinson, J. W., & Suo, Z. (1991). Mixed Mode Cracking in Layered Materials. In J. W. Hutchinson & T. Y. Wu (Eds.), *Advances in Applied Mechanics* (Vol. 29, pp. 63-191): Elsevier.

Hwang, G.-T., Park, H., Lee, J.-H., Oh, S., Park, K.-I., Byun, M., . . . Lee, K. J. (2014). Self-Powered Cardiac Pacemaker Enabled by Flexible Single Crystalline PMN-PT Piezoelectric Energy Harvester. *Advanced Materials, 26*(28), 4880-4887. doi:10.1002/adma.201400562

Jang, W. Y., Ku, Z., Jeon, J., Kim, J. O., Lee, S. J., Park, J., . . . Urbas, A. (2016). Experimental Demonstration of Adaptive Infrared Multispectral Imaging using Plasmonic Filter Array. *Sci Rep, 6*, 34876. doi:10.1038/srep34876

Jeon, J., Bhattarai, K., Kim, D.-K., Kim, J. O., Urbas, A., Lee, S. J., . . . Zhou, J. (2016). A Low-loss Metasurface Antireflection Coating on Dispersive Surface Plasmon Structure. *Scientific Reports, 6*(1), 36190. doi:10.1038/srep36190

Jeong, G. S., Baek, D.-H., Jung, H. C., Song, J. H., Moon, J. H., Hong, S. W., . . . Lee, S.-H. (2012). Solderable and electroplatable flexible electronic circuit on a porous stretchable elastomer. *Nature Communications, 3*(1), 977. doi:10.1038/ncomms1980

Jin, H., Matsuhisa, N., Lee, S., Abbas, M., Yokota, T., & Someya, T. (2017). Enhancing the performance of stretchable conductors for e-textiles by controlled ink permeation. *Advanced Materials, 29*(21), 1605848.

Jitian, S., & Bratu, I. (2012a, 2012). *Determination of optical constants of polymethyl methacrylate films from IR reflection-absorption spectra*.

Jitian, S., & Bratu, I. (2012b, 2012). *Determination of optical constants of polymethyl methacrylate films from IR reflection-absorption spectra.* Paper presented at the AIP Conf. Proc.

Jo, C., Park, Y., Jeong, J., Lee, K. T., & Lee, J. (2015). Structural Effect on Electrochemical Performance of Ordered Porous Carbon Electrodes for Na-Ion Batteries. *ACS Applied Materials & Interfaces, 7*(22), 11748-11754. doi:10.1021/acsami.5b03186

Jong-Hyun, A., Hoon-Sik, K., Keon Jae, L., Zhengtao, Z., Menard, E., Nuzzo, R. G., & Rogers, J. A. (2006). High-speed mechanically flexible single-crystal silicon thin-film transistors on plastic substrates. *IEEE Electron Device Letters, 27*(6), 460-462. doi:10.1109/LED.2006.874764

Joshi-Imre, A., & Bauerdick, S. (2014). Direct-Write Ion Beam Lithography. *Journal of Nanotechnology, 2014*, 170415. doi:10.1155/2014/170415

Khan, Y., Thielens, A., Muin, S., Ting, J., Baumbauer, C., & Arias, A. C. (2020). A New Frontier of Printed Electronics: Flexible Hybrid Electronics. *Advanced Materials, 32*(15), 1905279. doi:10.1002/adma.201905279

Kim, B., Jeon, J., Zhang, Y., Wie, D. S., Hwang, J., Lee, S. J., . . . Lee, C. H. (2019). Deterministic Nanoassembly of Quasi-Three-Dimensional Plasmonic Nanoarrays with Arbitrary Substrate Materials and Structures. *Nano Letters, 19*(8), 5796-5805. doi:10.1021/acs.nanolett.9b02598

Kim, D.-H., Viventi, J., Amsden, J. J., Xiao, J., Vigeland, L., Kim, Y.-S., . . . Rogers, J. A. (2010). Dissolvable films of silk fibroin for ultrathin conformal bio-integrated electronics. *Nature Materials, 9*(6), 511-517. doi:10.1038/nmat2745

Kim, I., Woo, K., Zhong, Z., Ko, P., Jang, Y., Jung, M., . . . Lee, S. (2018). A photonic sintering derived Ag flake/nanoparticle-based highly sensitive stretchable strain sensor for human motion monitoring. *Nanoscale, 10*(17), 7890-7897.

Kim, S., Wu, J., Carlson, A., Jin, S. H., Kovalsky, A., Glass, P., . . . Rogers, J. A. (2010). Microstructured elastomeric surfaces with reversible adhesion and examples of their use in deterministic assembly by transfer printing. *Proceedings of the National Academy of Sciences, 107*(40), 17095. doi:10.1073/pnas.1005828107

Korsunsky, A. M., Cherian, S., Raiteri, R., & Berger, R. (2007). On the micromechanics of micro-cantilever sensors: Property analysis and eigenstrain modeling. *Sensors and Actuators A: Physical, 139*(1), 70-77. doi:https://doi.org/10.1016/j.sna.2007.03.007

Kraft, U., Molina-Lopez, F., Son, D., Bao, Z., & Murmann, B. (2020). Ink Development and Printing of Conducting Polymers for Intrinsically Stretchable Interconnects and Circuits. *Advanced Electronic Materials, 6*(1), 1900681. doi:10.1002/aelm.201900681

Ku, Z., Jang, W.-Y., Zhou, J., Kim, J. O., Barve, A. V., Silva, S., . . . Lee, S. J. (2013). Analysis of subwavelength metal hole array structure for the enhancement of back-illuminated quantum dot infrared photodetectors. *Optics Express, 21*(4), 4709-4716. doi:10.1364/OE.21.004709

Kusy, R. P., Whitley, J. Q., & Kalachandra, S. (2001). Mechanical properties and interrelationships of poly(methyl methacrylate) following hydration over saturated salts. *Polymer, 42*(6), 2585-2595. doi:https://doi.org/10.1016/S0032-3861(00)00613-3

Lang, R. M., Badano, L. P., Mor-Avi, V., Afilalo, J., Armstrong, A., Ernande, L., . . . Voigt, J.-U. (2015). Recommendations for Cardiac Chamber Quantification by Echocardiography in Adults: An Update from the American Society of Echocardiography and the European Association of Cardiovascular Imaging. *European Heart Journal - Cardiovascular Imaging, 16*(3), 233-271. doi:10.1093/ehjci/jev014

Lee, B. H., Cho, Y. H., Lee, H., Lee, K. D., Kim, S. H., & Sung, M. M. (2007). High-Resolution Patterning of Aluminum Thin Films with a Water-Mediated Transfer Process. *Advanced Materials, 19*(13), 1714-1718. doi:10.1002/adma.200601884

Lee, C. H., Kim, D. R., Cho, I. S., William, N., Wang, Q., & Zheng, X. (2012). Peel-and-Stick: Fabricating Thin Film Solar Cell on Universal Substrates. *Scientific Reports, 2*, 1000. doi:10.1038/srep01000

Lee, C. H., Kim, D. R., & Zheng, X. (2011). Fabrication of Nanowire Electronics on Nonconventional Substrates by Water-Assisted Transfer Printing Method. *Nano Letters, 11*(8), 3435-3439. doi:10.1021/nl201901z

Lee, C. H., Kim, D. R., & Zheng, X. (2014). Transfer Printing Methods for Flexible Thin Film Solar Cells: Basic Concepts and Working Principles. *ACS Nano, 8*(9), 8746-8756. doi:10.1021/nn5037587

Lee, C. H., Kim, J.-H., Zou, C., Cho, I. S., Weisse, J. M., Nemeth, W., . . . Zheng, X. (2013). Peel-and-Stick: Mechanism Study for Efficient Fabrication of Flexible/Transparent Thin-film Electronics. *Scientific Reports, 3*, 2917. doi:10.1038/srep02917
https://www.nature.com/articles/srep02917#supplementary-information

Lee, M.-S., Lee, K., Kim, S.-Y., Lee, H., Park, J., Choi, K.-H., . . . Park, J.-U. (2013). High-Performance, Transparent, and Stretchable Electrodes Using Graphene–Metal Nanowire Hybrid Structures. *Nano Letters, 13*(6), 2814-2821. doi:10.1021/nl401070p

Lee, S., Kang, B., Keum, H., Ahmed, N., Rogers, J. A., Ferreira, P. M., . . . Min, B. (2016). Heterogeneously Assembled Metamaterials and Metadevices via 3D Modular Transfer Printing. *Sci Rep, 6*, 27621. doi:10.1038/srep27621

Lee, S. J., Ku, Z., Barve, A., Montoya, J., Jang, W. Y., Brueck, S. R., . . . Noh, S. K. (2011). A monolithically integrated plasmonic infrared quantum dot camera. *Nat Commun, 2*, 286. doi:10.1038/ncomms1283

Lelovas, P. P., Kostomitsopoulos, N. G., & Xanthos, T. T. (2014). A Comparative Anatomic and Physiologic Overview of the Porcine Heart. *Journal of the American Association for Laboratory Animal Science, 53*(5), 432-438.

Lewis, J. A. (2006). Direct Ink Writing of 3D Functional Materials. *Advanced Functional Materials, 16*(17), 2193-2204. doi:10.1002/adfm.200600434

Li, Q., Li, Z., Li, N., Chen, X., Chen, P., Shen, X., & Lu, W. (2014). High-polarization-discriminating infrared detection using a single quantum well sandwiched in plasmonic micro-cavity. *Sci Rep, 4*, 6332. doi:10.1038/srep06332

Li, W.-D., Ding, F., Hu, J., & Chou, S. Y. (2011). Three-dimensional cavity nanoantenna coupled plasmonic nanodots for ultrahigh and uniform surface-enhanced Raman scattering over large area. *Optics Express, 19*(5), 3925-3936. doi:10.1364/OE.19.003925

Li, W. T., Charters, R. B., Luther-Davies, B., & Mar, L. (2004). Significant improvement of adhesion between gold thin films and a polymer. *Applied Surface Science, 233*(1-4), 227-233. doi:10.1016/j.apsusc.2004.03.220

Lin, Y.-S., Liao, S., Liu, X., Tong, Y., Xu, Z., Xu, R., . . . Yu, Y. (2019). Tunable terahertz metamaterial by using three-dimensional double split-ring resonators. *Optics & Laser Technology, 112*, 215-221. doi:https://doi.org/10.1016/j.optlastec.2018.11.020

Lind, J. U., Busbee, T. A., Valentine, A. D., Pasqualini, F. S., Yuan, H., Yadid, M., . . . Parker, K. K. (2017). Instrumented cardiac microphysiological devices via multimaterial three-dimensional printing. *Nature Materials, 16*(3), 303-308. doi:10.1038/nmat4782

Linghu, C., Wang, C., Cen, N., Wu, J., Lai, Z., & Song, J. (2019). Rapidly tunable and highly reversible bio-inspired dry adhesion for transfer printing in air and a vacuum. *Soft Matter, 15*(1), 30-37. doi:10.1039/C8SM01996G

Liu, H., Li, Q., Zhang, S., Yin, R., Liu, X., He, Y., . . . Guo, Z. (2018). Electrically conductive polymer composites for smart flexible strain sensors: a critical review. *Journal of Materials Chemistry C, 6*(45), 12121-12141. doi:10.1039/C8TC04079F

Liu, J., Zhang, X., Liu, Y., Rodrigo, M., Loftus, P. D., Aparicio-Valenzuela, J., . . . Bao, Z. (2020). Intrinsically stretchable electrode array enabled in vivo electrophysiological mapping of atrial fibrillation at cellular resolution. *Proceedings of the National Academy of Sciences, 117*(26), 14769. doi:10.1073/pnas.2000207117

Liu, X., Tyler, T., Starr, T., Starr, A. F., Jokerst, N. M., & Padilla, W. J. (2011). Taming the blackbody with infrared metamaterials as selective thermal emitters. *Phys Rev Lett, 107*(4), 045901. doi:10.1103/PhysRevLett.107.045901

Loo, J. F. C., Ho, A. H. P., Turner, A. P. F., & Mak, W. C. (2019). Integrated Printed Microfluidic Biosensors. *Trends in Biotechnology, 37*(10), 1104-1120. doi:https://doi.org/10.1016/j.tibtech.2019.03.009

Luo, Y., Jiang, X., Liu, L., & Si, G. (2018). Recent Advances in Plasmonic Nanolithography. *Nanoscience and Nanotechnology Letters, 10*(1), 1-12. doi:10.1166/nnl.2018.2568

Marcin, K. S., Tadeusz, M., Gabriela, S.-B., Lutful, K., David, J. W., Chenchun, Y., . . . Waclaw, U. (2010). *Measurements of stress-optic coefficient and Young's modulus in PMMA fibers drawn under different conditions.* Paper presented at the Proc.SPIE.

Mattsson, C. G., Thungstrom, G., Bertilsson, K., Nilsson, H., & Martin, H. (2007, 28-31 Oct. 2007). *Development of an infrared thermopile detector with a thin self-supporting SU-8 membrane.* Paper presented at the SENSORS, 2007 IEEE.

Mei, H., Landis, C. M., & Huang, R. (2011). Concomitant wrinkling and buckle-delamination of elastic thin films on compliant substrates. *Mechanics of Materials, 43*(11), 627-642. doi:https://doi.org/10.1016/j.mechmat.2011.08.003

Meitl, M. A., Zhu, Z.-T., Kumar, V., Lee, K. J., Feng, X., Huang, Y. Y., . . . Rogers, J. A. (2006). Transfer printing by kinetic control of adhesion to an elastomeric stamp. *Nature Materials, 5*(1), 33-38. doi:10.1038/nmat1532

Melosh, N. A., Boukai, A., Diana, F., Gerardot, B., Badolato, A., Petroff, P. M., & Heath, J. R. (2003). Ultrahigh-Density Nanowire Lattices and Circuits. *Science, 300*(5616), 112. doi:10.1126/science.1081940

Menard, E., Lee, K. J., Khang, D. Y., Nuzzo, R. G., & Rogers, J. A. (2004). A printable form of silicon for high performance thin film transistors on plastic substrates. *Applied Physics Letters, 84*(26), 5398-5400. doi:10.1063/1.1767591

Meng, J., Cadusch, J. J., & Crozier, K. B. (2021). Plasmonic Mid-Infrared Filter Array-Detector Array Chemical Classifier Based on Machine Learning. *ACS Photonics, 8*(2), 648-657. doi:10.1021/acsphotonics.0c01786

Molina-Lopez, F., Gao, T. Z., Kraft, U., Zhu, C., Öhlund, T., Pfattner, R., . . . Bao, Z. (2019). Inkjet-printed stretchable and low voltage synaptic transistor array. *Nature Communications, 10*(1), 2676. doi:10.1038/s41467-019-10569-3

Montoya, J. A., Tian, Z.-B., Krishna, S., & Padilla, W. J. (2017). Ultra-thin infrared metamaterial detector for multicolor imaging applications. *Optics Express, 25*(19), 23343-23355. doi:10.1364/OE.25.023343

Montoya, J. A., Tian, Z. B., Krishna, S., & Padilla, W. J. (2017). Ultra-thin infrared metamaterial detector for multicolor imaging applications. *Opt Express, 25*(19), 23343-23355. doi:10.1364/OE.25.023343

Murray, W. A., & Barnes, W. L. (2007). Plasmonic materials. *Advanced Materials, 19*(22), 3771-3782.

Muth, J. T., Vogt, D. M., Truby, R. L., Mengüç, Y., Kolesky, D. B., Wood, R. J., & Lewis, J. A. (2014). Embedded 3D Printing of Strain Sensors within Highly Stretchable Elastomers. *Advanced Materials, 26*(36), 6307-6312. doi:10.1002/adma.201400334

Naldoni, A., Shalaev, V. M., & Brongersma, M. L. (2017). Applying plasmonics to a sustainable future. *Science, 356*(6341), 908. doi:10.1126/science.aan5802

Ni, X., Wong, Z. J., Mrejen, M., Wang, Y., & Zhang, X. (2015). An ultrathin invisibility skin cloak for visible light. *Science, 349*(6254), 1310. doi:10.1126/science.aac9411

Ooi, K. J. A., Chu, H. S., Ang, L. K., & Bai, P. (2013). Mid-infrared active graphene nanoribbon plasmonic waveguide devices. *Journal of the Optical Society of America B, 30*(12), 3111-3116. doi:10.1364/JOSAB.30.003111

Ordal, M. A., Bell, R. J., Alexander, R. W., Long, L. L., & Querry, M. R. (1985). Optical properties of fourteen metals in the infrared and far infrared: Al, Co, Cu, Au, Fe, Pb, Mo, Ni, Pd, Pt, Ag, Ti, V, and W. *Applied Optics, 24*(24), 4493-4499. doi:10.1364/AO.24.004493

Otterstad, J. E. (2002). Measuring left ventricular volume and ejection fraction with the biplane Simpson's method. *Heart, 88*(6), 559. doi:10.1136/heart.88.6.559

Ozbay, E. (2006). Plasmonics: merging photonics and electronics at nanoscale dimensions. *science, 311*(5758), 189-193.

Ozbolat, V., Dey, M., Ayan, B., Povilianskas, A., Demirel, M. C., & Ozbolat, I. T. (2018). 3D Printing of PDMS Improves Its Mechanical and Cell Adhesion Properties. *ACS Biomaterials Science & Engineering, 4*(2), 682-693. doi:10.1021/acsbiomaterials.7b00646

Park, D. H., Park, H. W., Chung, J. W., Nam, K., Choi, S., Chung, Y. S., . . . Kim, D. H. (2019). Highly Stretchable, High-Mobility, Free-Standing All-Organic Transistors Modulated by Solid-State Elastomer Electrolytes. *Advanced Functional Materials, 29*(18), 1808909. doi:10.1002/adfm.201808909

Park, J., Choi, S., Janardhan, A. H., Lee, S.-Y., Raut, S., Soares, J., . . . Hwang, H. J. (2016). Electromechanical cardioplasty using a wrapped elasto-conductive epicardial mesh. *Science Translational Medicine, 8*(344), 344ra386. doi:10.1126/scitranslmed.aad8568

Park, S.-M., Jang, N.-S., Ha, S.-H., Kim, K. H., Jeong, D.-W., Kim, J., . . . Kim, J.-M. (2015). Metal nanowire percolation micro-grids embedded in elastomers for stretchable and transparent conductors. *Journal of Materials Chemistry C, 3*(31), 8241-8247.

Preda, M. B., & Burlacu, A. (2010). Electrocardiography as a tool for validating myocardial ischemia–reperfusion procedures in mice. *Comparative medicine, 60*(6), 443-447.

Primpke, S., Godejohann, M., & Gerdts, G. (2020). Rapid Identification and Quantification of Microplastics in the Environment by Quantum Cascade Laser-Based Hyperspectral Infrared Chemical Imaging. *Environmental Science & Technology, 54*(24), 15893-15903. doi:10.1021/acs.est.0c05722

Robin, C. J., Vishnoi, A., & Jonnalagadda, K. N. (2014). Mechanical Behavior and Anisotropy of Spin-Coated SU-8 Thin Films for MEMS. *Journal of Microelectromechanical Systems, 23*(1), 168-180. doi:10.1109/JMEMS.2013.2264341

Rosenberg, J., Shenoi, R. V., Vandervelde, T. E., Krishna, S., & Painter, O. (2009). A multispectral and polarization-selective surface-plasmon resonant midinfrared detector. *Applied Physics Letters, 95*(16), 161101. doi:10.1063/1.3244204

Safaei, A., Modak, S., Lee, J., Chandra, S., Franklin, D., Vazquez-Guardado, A., & Chanda, D. (2018). Multi-spectral frequency selective mid-infrared microbolometers. *Opt Express, 26*(25), 32931-32940. doi:10.1364/OE.26.032931

Sato, M., Matsumoto, N., Noguchi, A., Okonogi, T., Sasaki, T., & Ikegaya, Y. (2018). Simultaneous monitoring of mouse respiratory and cardiac rates through a single precordial electrode. *Journal of Pharmacological Sciences, 137*(2), 177-186. doi:https://doi.org/10.1016/j.jphs.2018.06.009

Sekitani, T., Noguchi, Y., Hata, K., Fukushima, T., Aida, T., & Someya, T. (2008). A rubberlike stretchable active matrix using elastic conductors. *Science, 321*(5895), 1468-1472.

Shah, Y. D., Grant, J., Hao, D., Kenney, M., Pusino, V., & Cumming, D. R. S. (2018). Ultra-narrow Line Width Polarization-Insensitive Filter Using a Symmetry-Breaking Selective Plasmonic Metasurface. *ACS Photonics, 5*(2), 663-669. doi:10.1021/acsphotonics.7b01011

Shahrjerdi, D., & Bedell, S. W. (2013). Extremely Flexible Nanoscale Ultrathin Body Silicon Integrated Circuits on Plastic. *Nano Letters, 13*(1), 315-320. doi:10.1021/nl304310x

Shahrjerdi, D., Bedell, S. W., Bayram, C., Lubguban, C. C., Fogel, K., Lauro, P., . . . Sadana, D. (2013). Ultralight High-Efficiency Flexible InGaP/(In)GaAs Tandem Solar Cells on Plastic. *Advanced Energy Materials, 3*(5), 566-571. doi:10.1002/aenm.201200827

Soepriatna, A. H., Yeh, A. K., Clifford, A. D., Bezci, S. E., O'Connell, G. D., & Goergen, C. J. (2019). Three-dimensional myocardial strain correlates with murine left ventricular remodelling severity post-infarction. *Journal of The Royal Society Interface, 16*(160), 20190570. doi:10.1098/rsif.2019.0570

Soukoulis, C. M., & Wegener, M. (2010). Optical Metamaterials—More Bulky and Less Lossy. *Science, 330*(6011), 1633. doi:10.1126/science.1198858

Stewart, M. E., Mack, N. H., Malyarchuk, V., Soares, J. A., Lee, T. W., Gray, S. K., . . . Rogers, J. A. (2006). Quantitative multispectral biosensing and 1D imaging using quasi-3D plasmonic crystals. *Proc Natl Acad Sci U S A, 103*(46), 17143-17148. doi:10.1073/pnas.0606216103

Stockman, M. I., Kneipp, K., Bozhevolnyi, S. I., Saha, S., Dutta, A., Ndukaife, J., . . . Kling, M. F. (2018). Roadmap on plasmonics. *Journal of Optics, 20*(4), 043001. doi:10.1088/2040-8986/aaa114

Tan, X., Zhang, H., Li, J., Wan, H., Guo, Q., Zhu, H., . . . Yi, F. (2020). Non-dispersive infrared multi-gas sensing via nanoantenna integrated narrowband detectors. *Nature Communications, 11*(1), 5245. doi:10.1038/s41467-020-19085-1

Tybrandt, K., Khodagholy, D., Dielacher, B., Stauffer, F., Renz, A. F., Buzsáki, G., & Vörös, J. (2018). High-density stretchable electrode grids for chronic neural recording. *Advanced Materials, 30*(15), 1706520.

Updegrove, A., Wilson, N. M., Merkow, J., Lan, H., Marsden, A. L., & Shadden, S. C. (2017). SimVascular: An Open Source Pipeline for Cardiovascular Simulation. *Annals of biomedical engineering, 45*(3), 525-541. doi:10.1007/s10439-016-1762-8

Vafaiee, M., Vossoughi, M., Mohammadpour, R., & Sasanpour, P. (2019). Gold-Plated Electrode with High Scratch Strength for Electrophysiological Recordings. *Scientific Reports, 9*(1), 2985. doi:10.1038/s41598-019-39138-w

Valentine, A. D., Busbee, T. A., Boley, J. W., Raney, J. R., Chortos, A., Kotikian, A., . . . Lewis, J. A. (2017). Hybrid 3D Printing of Soft Electronics. *Advanced Materials, 29*(40), 1703817. doi:10.1002/adma.201703817

Valentine, J., Zhang, S., Zentgraf, T., Ulin-Avila, E., Genov, D. A., Bartal, G., & Zhang, X. (2008). Three-dimensional optical metamaterial with a negative refractive index. *Nature, 455*(7211), 376-379. doi:10.1038/nature07247

Vazquez-Guardado, A., Smith, A., Wilson, W., Ortega, J., Perez, J. M., & Chanda, D. (2016). Hybrid cavity-coupled plasmonic biosensors for low concentration, label-free and selective biomolecular detection. *Opt Express, 24*(22), 25785-25796. doi:10.1364/OE.24.025785

Vial, B., Commandré, M., Demésy, G., Nicolet, A., Zolla, F., Bedu, F., . . . Roux, L. (2014). Transmission enhancement through square coaxial aperture arrays in metallic film: when leaky modes filter infrared light for multispectral imaging. *Optics Letters, 39*(16), 4723-4726. doi:10.1364/OL.39.004723

Vieu, C., Carcenac, F., Pépin, A., Chen, Y., Mejias, M., Lebib, A., . . . Launois, H. (2000). Electron beam lithography: resolution limits and applications. *Applied Surface Science, 164*(1), 111-117. doi:https://doi.org/10.1016/S0169-4332(00)00352-4

Wang, C., Zhang, Q., Song, Y., & Chou, S. Y. (2014). Plasmonic Bar-Coupled Dots-on-Pillar Cavity Antenna with Dual Resonances for Infrared Absorption and Sensing: Performance and Nanoimprint Fabrication. *ACS Nano, 8*(3), 2618-2624. doi:10.1021/nn406281u

Wang, Y., Du, Z., Park, Y., Chen, C., Zhang, X., & Pan, L. (2015). Quasi-3D plasmonic coupling scheme for near-field optical lithography and imaging. *Opt Lett, 40*(16), 3918-3921. doi:10.1364/OL.40.003918

Wang, Z., Ren, J., Liu, R., Sun, X., Huang, D., Xu, W., . . . Liu, Y. (2020). Three dimensional core-shell structured liquid metal/elastomer composite via coaxial direct ink writing for electromagnetic interference shielding. *Composites Part A: Applied Science and Manufacturing, 136*, 105957. doi:https://doi.org/10.1016/j.compositesa.2020.105957

Wie, D. S., Zhang, Y., Kim, M. K., Kim, B., Park, S., Kim, Y.-J., . . . Lee, C. H. (2018). Wafer-recyclable, environment-friendly transfer printing for large-scale thin-film nanoelectronics. *Proceedings of the National Academy of Sciences, 115*(31), E7236. doi:10.1073/pnas.1806640115

Won, S. M., Song, E., Reeder, J. T., & Rogers, J. A. (2020). Emerging Modalities and Implantable Technologies for Neuromodulation. *Cell, 181*(1), 115-135. doi:https://doi.org/10.1016/j.cell.2020.02.054

Xia, D., Ku, Z., Lee, S. C., & Brueck, S. R. (2011). Nanostructures and functional materials fabricated by interferometric lithography. *Adv Mater, 23*(2), 147-179. doi:10.1002/adma.201001856

Xu, J., Moon, H., Xu, J., Lim, J., Fischer, T., McNally, H. A., . . . Lee, H. (2020). One-Step Large-Scale Nanotexturing of Nonplanar PTFE Surfaces to Induce Bactericidal and Anti-inflammatory Properties. *ACS Applied Materials & Interfaces, 12*(24), 26893-26904.

Xu, J., Xu, J., Moon, H., Sintim, H. O., & Lee, H. (2020). Zwitterionic Porous Conjugated Polymers as a Versatile Platform for Antibiofouling Implantable Bioelectronics. *ACS Applied Polymer Materials, 2*(2), 528-536.

Xu, J., Xu, J., Moon, H., Sintim, H. O., & Lee, H. (2021). Zwitterionic liquid crystalline polythiophene as an antibiofouling biomaterial. *Journal of Materials Chemistry B, 9*(2), 349-356. doi:10.1039/D0TB02264K

Xu, L., Gutbrod, S. R., Bonifas, A. P., Su, Y., Sulkin, M. S., Lu, N., . . . Rogers, J. A. (2014). 3D multifunctional integumentary membranes for spatiotemporal cardiac measurements and stimulation across the entire epicardium. *Nature Communications, 5*(1), 3329. doi:10.1038/ncomms4329

Xu, L., Gutbrod, S. R., Ma, Y., Petrossians, A., Liu, Y., Webb, R. C., . . . Rogers, J. A. (2015). Materials and Fractal Designs for 3D Multifunctional Integumentary Membranes with Capabilities in Cardiac Electrotherapy. *Advanced Materials, 27*(10), 1731-1737. doi:10.1002/adma.201405017

Xu, S., Yan, Z., Jang, K.-I., Huang, W., Fu, H., Kim, J., . . . Rogers, J. A. (2015). Assembly of micro/nanomaterials into complex, three-dimensional architectures by compressive buckling. *Science, 347*(6218), 154. doi:10.1126/science.1260960

Xu, T., Yoo, J. H., Babu, S., Roy, S., Lee, J.-B., & Lu, H. (2016). Characterization of the mechanical behavior of SU-8 at microscale by viscoelastic analysis. *Journal of Micromechanics and Microengineering, 26*(10), 105001. doi:10.1088/0960-1317/26/10/105001

Yakovliev, A., Ziniuk, R., Wang, D., Xue, B., Vretik, L. O., Nikolaeva, O. A., . . . Ohulchanskyy, T. Y. (2019). Hyperspectral Multiplexed Biological Imaging of Nanoprobes Emitting in the Short-Wave Infrared Region. *Nanoscale Research Letters, 14*(1), 243. doi:10.1186/s11671-019-3068-x

Yan, Z., Han, M., Shi, Y., Badea, A., Yang, Y., Kulkarni, A., . . . Rogers, J. A. (2017). Three-dimensional mesostructures as high-temperature growth templates, electronic cellular scaffolds, and self-propelled microrobots. *Proc Natl Acad Sci U S A, 114*(45), E9455-E9464. doi:10.1073/pnas.1713805114

Yan, Z., Pan, T., Xue, M., Chen, C., Cui, Y., Yao, G., . . . Lin, Y. (2017). Thermal Release Transfer Printing for Stretchable Conformal Bioelectronics. *Advanced Science, 4*(11), 1700251. doi:10.1002/advs.201700251

Yan, Z., Zhang, F., Wang, J., Liu, F., Guo, X., Nan, K., . . . Rogers, J. A. (2016). Controlled mechanical buckling for origami-inspired construction of 3D microstructures in advanced materials. *Adv Funct Mater, 26*(16), 2629-2639. doi:10.1002/adfm.201504901

Yang, X., Yao, J., Rho, J., Yin, X., & Zhang, X. (2012). Experimental realization of three-dimensional indefinite cavities at the nanoscale with anomalous scaling laws. *Nature Photonics, 6*, 450. doi:10.1038/nphoton.2012.124
https://www.nature.com/articles/nphoton.2012.124#supplementary-information

Yi, H., Seong, M., Sun, K., Hwang, I., Lee, K., Cha, C., . . . Jeong, H. E. (2018). Wet-Responsive, Reconfigurable, and Biocompatible Hydrogel Adhesive Films for Transfer Printing of Nanomembranes. *Advanced Functional Materials, 28*(18), 1706498. doi:10.1002/adfm.201706498

Yoo, D., Vidal-Codina, F., Ciracì, C., Nguyen, N.-C., Smith, D. R., Peraire, J., & Oh, S.-H. (2019). Modeling and observation of mid-infrared nonlocality in effective epsilon-near-zero ultranarrow coaxial apertures. *Nature Communications, 10*(1), 4476. doi:10.1038/s41467-019-12038-3

Zhang, M., Lu, M., Ge, C., & Cunningham, B. T. (2014). Plasmonic external cavity laser refractometric sensor. *Opt Express, 22*(17), 20347-20357. doi:10.1364/OE.22.020347

Zhang, S., Bin, W., Xu, B., Zheng, X., Chen, B., Lv, X., . . . Hofmann, W. (2019). Mixed-gas CH4/CO2/CO detection based on linear variable optical filter and thermopile detector array. *Nanoscale Research Letters, 14*(1), 348. doi:10.1186/s11671-019-3176-7

Zhang, S., Fan, W., Malloy, K. J., Brueck, S. R. J., Panoiu, N. C., & Osgood, R. M. (2005). Near-infrared double negative metamaterials. *Optics Express, 13*(13), 4922-4930. doi:10.1364/OPEX.13.004922

Zhang, S., Fan, W., Panoiu, N. C., Malloy, K. J., Osgood, R. M., & Brueck, S. R. J. (2006). Optical negative-index bulk metamaterials consisting of 2D perforated metal-dielectric stacks. *Optics Express, 14*(15), 6778-6787. doi:10.1364/OE.14.006778

Zhang, X., & Liu, Z. (2008). Superlenses to overcome the diffraction limit. *Nature Materials, 7*, 435. doi:10.1038/nmat2141

Zhang, Y., Liu, Q., & Xu, B. (2017). Liquid-assisted, etching-free, mechanical peeling of 2D materials. *Extreme Mechanics Letters, 16*, 33-40. doi:https://doi.org/10.1016/j.eml.2017.08.005

Zhang, Y., Zhang, F., Yan, Z., Ma, Q., Li, X., Huang, Y., & Rogers, J. A. (2017). Printing, folding and assembly methods for forming 3D mesostructures in advanced materials. *Nature Reviews Materials, 2*(4). doi:10.1038/natrevmats.2017.19

Zhao, Y., Belkin, M. A., & Alu, A. (2012). Twisted optical metamaterials for planarized ultrathin broadband circular polarizers. *Nat Commun, 3*, 870. doi:10.1038/ncomms1877

Zhu, Z., Guo, S.-Z., Hirdler, T., Eide, C., Fan, X., Tolar, J., & McAlpine, M. C. (2018). 3D Printed Functional and Biological Materials on Moving Freeform Surfaces. *Advanced Materials, 30*(23), 1707495. doi:10.1002/adma.201707495

Zhu, Z., Park, H. S., & McAlpine, M. C. (2020). 3D printed deformable sensors. *Science Advances, 6*(25), eaba5575. doi:10.1126/sciadv.aba5575